UNIVERSIDADE DE LISBOA
FACULDADE DE CIÊNCIAS
DEPARTAMENTO DE FÍSICA


# Observational signatures of hot spots orbiting black hole mimickers

Daniela Sofia Jorge Cordeiro

**Mestrado em Física**
Especialização em Astrofísica e Cosmologia

Dissertação orientada por:
Francisco S. N. Lobo
João Luís Rosa

2024

# Agradecimentos

Gostaria de começar por agradecer ao professor Francisco Lobo por ter aceite orientar esta dissertação e pela oportunidade de estudar um tema que gosto e que para mim é tão fascinante. Estou grata por toda a motivação e apoio constantes, pois sem estes o meu percurso teria sem dúvida sido mais difícil e menos prazeroso. Após uma reunião com o professor Francisco eu saía a sentir-me melhor com o meu trabalho e com mais vontade e força de trabalhar. Agradeço também por se lembrar de mim para novos projetos. Na mesma nota, agradeço ao professor João Luís Rosa por todo o conhecimento que partilhou comigo, por toda a sua disponibilidade, esclarecimentos e feedback que foram cruciais para desenvolver esta dissertação. A ambos gostaria de agradecer por toda a compreensão e paciência com o meu estado de saúde e por nunca me fazerem sentir pressionada. Posso dizer que graças a vocês tive uma experiência positiva em que aprendi imenso.

A nível académico, agradeço ao professor Nelson Nunes, ao professor Pedro Machado, ao professor António Silva e ao professor Ismael Tereno. Tiveram todos um impacto muito positivo no meu percurso académico e as suas aulas fizeram-me ter ainda mais certeza de que me encontro no caminho certo. Agradeço aos meus colegas de Licenciatura e Mestrado Sandro Moreira e Rafael Rianço por todos os debates físicos e por me acompanharem ao longo deste percurso. Agradeço ainda ao João Cordeiro por todo o seu espírito Zen contagiante e à Mariana Pinto por me acompanhar desde o dia 1 de Universidade até aos dias de hoje. Não me irei esquecer dos nossos almoços na cantina de direito e todas as nossas discussões físicas e filosóficas.

Numa nota mais pessoal gostaria de agradecer às minhas amigas Margarida Coelho e Stella Pereira por me arrancarem de casa quando precisava de descansar do trabalho. Agradeço por, apesar de termos seguido caminhos diferentes, continuarem aqui para me apoiar.

Gostaria de agradecer ainda à minha família por todo o apoio e interesse no trabalho que desenvolvi. Agradeço especialmente aos meus vizinhos de cima, a minha tia Lena e o meu tio Zé por terem estado sempre envolvidos no meu percurso académico e por me terem apoiado nesta fase difícil (agora já posso ir experimentar a passadeira rolante). Agradeço também à minha avó por ser como a minha segunda mãe. Agradeço por todos os almoços deliciosos, todas as tardes bem passadas e toda a paciência por aturares a peste que eu era em criança. Mas mais que tudo, por mostrares sempre muito orgulho no meu trabalho. Da minha família, gostava de agradecer aos meus fãs número um: os meus pais. Era impossível ter pedido por pais melhores que vocês. Obrigado, pai, por seres um grande companheiro e por me ajudares a manter a minha saúde física e mental ao longo de todo este processo. Obrigado, mãe, por seres a minha melhor amiga, por me ouvires a falar durante horas do que me apaixona, dos meus sonhos mas também do que me assusta e do que me entristece. Obrigado por todos os teus conselhos, por me relembrares que, apesar de todos os meus obstáculos, eu estou aqui e que consigo fazer tanto como qualquer outra pessoa de perfeita saúde. Obrigado por serem os melhores pais do mundo, eu sou a pessoa mais sortuda por vos ter do meu lado.

Por último, gostaria de agradecer ao Luís Silva, o meu namorado. Obrigado por me aturares há já

quatro anos que mais parecem quarenta. Obrigado por todo o teu amor, paciência, positividade e apoio incondicional. Obrigado por partilhares o teu gosto de física comigo e por mais do que um namorado seres um amigo e companheiro. Obrigada por teres acompanhado o meu trabalho de perto e por todos os teus conselhos vitais no desenvolvimento da mesma. Obrigado por me apoiares em todas as minhas noitadas e compreenderes quando estou mais focada no trabalho. No fundo, obrigado por seres a pessoa incrível que és.

Agradeço a todos os que aqui foram referidos pelo impacto positivo que tiveram na minha vida e no meu percurso académico. Nunca me irei esquecer de vocês.

# Resumo

Esta tese tem como objetivo analisar as características observacionais de hot spots que orbitam gravastars estáticas e com camada fina e comparar estes resultados com as assinaturas observacionais conhecidas de um buraco negro de Schwarzschild. Para tal, a dissertação encontra-se estruturada do seguinte modo.

O primeiro capítulo correspondente à introdução, encontra-se dividido em duas secções: Revisão de Literatura e Motivação. Na primeira secção focamos os Buracos Negros, mais especificamente: a sua origem histórica, métodos de deteção que corroboram a sua existência e permitem observar as suas assinaturas visuais; os problemas inerentes a estas soluções e os objetos compactos alternativos capazes de imitarem as propriedades observacionais dos buracos negros sem os referidos problemas. Começamos assim por, na primeira subsecção, introduzir as teorias envolvidas na descoberta pioneira de buracos negros, com especial foco na teoria da Relatividade Geral de Einstein. A primeira solução da equação de campo de vácuo de Einstein, conhecida como solução de Schwarzschild, revelou-se descrever o espaço-tempo de um objeto extremamente compacto, mais tarde reconhecido como um buraco negro. Visto que este objeto possui um campo gravitacional forte ao ponto de que nem a luz consegue escapar a sua atração, é necessário estudar a influência que o buraco negro tem no ambiente que o rodeia, de modo a podermos detetar a sua existência. Deste modo, a segunda subsecção tem como foco diferentes métodos de deteção de buracos negros, nomeadamente pelo estudo da matéria que o envolve, órbitas de estrelas e deteções de ondas gravitacionais, e como estes contribuíram na primeira imagem de um objeto compacto pela colaboração Event Horizon Telescope (EHT). No mesmo tópico, as assinaturas observacionais de um buraco negro de Schwarzschild são introduzidas na próxima subsecção, onde definimos termos como sombra, imagem primária, imagem secundária e fotões do anel de luz. Apesar de todas as evidências observacionais que corroboram a existência de buracos negros, este tipo de espaço-tempo possui diversos obstáculos, tanto clássicos como quânticos, que se encontram descritos na penúltima subsecção. Tais problemas levaram à proposta de objetos compactos alternativos aos buracos negros, capazes de imitar as assinaturas observacionais dos mesmos sem os seus obstáculos. Estes objetos são conhecidos como imitadores de buracos negros, e são o foco da última subseção da introdução, onde revemos trabalhos anteriores onde as assinaturas observacionais de outros objetos compactos foram alvo de estudo, introduzindo assim uma imagem característica destes objetos. Realizamos ainda uma introdução a gravastars e ao modelo alvo de estudo nesta tese, o modelo de camada fina que consiste numa região exterior descrita pela solução de Schwarzschild, seguida de uma transição perto de onde o horizonte de eventos do buraco negro seria esperado, correspondendo a uma camada fina que separa o exterior de uma região interior descrita pela solução de de Sitter. O capítulo culmina assim na motivação que nos levou a realizar esta tese.

No segundo capítulo exploramos a mecânica de buracos negros em três secções: Equações de campo de Einstein; Equações de movimento e Potencial Efectivo; O buraco negro de Schwarzschild. Relativamente às equações de campo de Einstein, são apresentados os principais formalismos e ex-

pressões necessárias para a posterior compreensão da dissertação. Realizamos a derivação da solução de Schwarzschild, estudando algumas das suas propriedades físicas, nomeadamente o tipo de singularidades presentes. O mesmo processo é aplicado na dedução e estudo da solução de de Sitter. Em seguida, focamos o estudo do movimento ao longo de geodésicas. Inicia-se a exposição derivando a equação geral da geodésica, restingindo esta ao caso específico de geometrias do espaço-tempo estáticas e esfericamente simétricas. Utiliza-se o resultado anterior para obter uma equação unidimensional do movimento num potencial. Esta é útil para estudar o movimento orbital de fotões e partículas massivas, como por exemplo, de geodésicas circulares nulas, conhecidas também por anéis de luz. Aplicamos por fim a análise anterior ao caso do buraco negro de Schwarzschild, onde determinamos a existência, localização e estabilidade de órbitas circulares nulas e temporais neste espaço-tempo.

O terceiro capítulo foca-se no objeto compacto que é alvo de estudo nesta dissertação: As Gravastars. Na primeira secção descrevemos o modelo de camada fina, mais especificamente, começamos por caracterizar o seu elemento de linha para a região exterior e interior da gravastar onde a não exoticidade da matéria é discutida assim como algumas das suas propriedades físicas. De seguida, realizamos a dedução das condições de junção necessárias para garantir uma continuidade do elemento de linha na camada que separa as diferentes regiões. Concluímos que este modelo depende de dois parâmetros livres: o raio da gravastar $a$ e o parâmetro $\alpha$ associado à distribuição de massa. Em relação ao último parâmetro, se o seu valor for unitário, a massa total da gravastar encontra-se distribuída uniformemente em todo o seu volume. O decréscimo deste valor altera a distribuição do volume para a superfície da camada, até atingir o seu valor mínimo correspondente a uma distribuição uniforme total da massa na superfície da camada. Tal valor mínimo é definido de modo a que a densidade de energia do fluído se mantenha positiva. Por último estudamos a influência destes parâmetros nos componentes da métrica e aplicamos o estudo do capítulo anterior do potencial efetivo de fotões, à geometria do espaço-tempo da gravastar. Demonstramos que a existência e estabilidade dos anéis de luz dependem do raio da gravastar considerado, sendo que configurações pouco compactas não têm nenhum anel de luz presente, enquanto que configurações ultra compactas apresentam dois anéis de luz, um estável e outro instável. No caso crítico em que o raio da gravastar é $3M$, a configuração apresenta um par degenerado de aneís de luz.

No quarto capítulo expomos a metodologia utilizada para obter os resultados do capítulo seguinte, em 3 secções: Implementação, ray-tracing e observáveis astrométricos. Começamos por introduzir o código de ray-tracing GYOTO que é utilizado na obtenção dos resultados, uma vez que tem a capacidade de gerar imagens e espetros de diversas fontes de emissão em torno de um objeto compacto. Este código tem ainda um nível de precisão suficiente para ajustar os dados do instrumento GRAVITY, sendo que produz dados astrometricos que podem ser comparados com as observações dos intrumentos. De seguida, explicitamos o método de implementação da métrica da gravastar no código onde é necessário inserir dados sobre os componentes da métrica, símbolos de Christoffel e velocidade orbital. No fim da primeira secção apresentamos o modelo de emissão considerado, sendo este uma esfera uniforme que emite radiação isotropicamente. Na segunda secção aprofundamos o método utilizado para traçar as geodésicas nulas, conhecido como ray-tracing, consistindo em dois passos: a integração de geodésicas nulas do observador para o passado em direção à fonte de emissão e a integração da equação de transferência radiativa ao longo de uma geodésica. Por último, apresentamos os observáveis astrométricos que são obtidos pelo código, nomeadamente, o fluxo integrado ao longo do tempo, a magnitude temporal e os centróides temporais em conjunto com os dados especificos do código que reproduzem os resultados presentes no próximo capítulo. Entre os dados inseridos no código, destacamos que diferentes raios de gravastar correspondem a configurações diferentes que intitulamos de GS1-GS5 consoante o valor do raio considerado.

No capítulo cinco apresentamos os resultados obtidos que se encontram divididos em duas secções: Fluxos integrados ao longo do tempo; Magnitudes e Centróides temporais. A primeira secção encontra-se dividida em três, para facilitar a navegação nos resultados, onde estudamos a respetiva influência do ângulo de observação, raio orbital e distribuição de massa. Respetivamente ao ângulo de observação, este encontra-se ainda divido pelas soluções mais compactas e menos compactas. Pelo estudo dos resultados, concluímos que configurações mais compactas de gravastars demonstram assinaturas observacionais semelhantes às de um buraco negro. Uma vez que estes modelos apenas apresentam uma imagem secundária adicional, a gravastar é ainda mais idêntica a um buraco negro de Schwarzschild do que outros objetos compactos previamente estudados que em vez de uma, apresentam duas tais contribuições. Para configurações menos compactas não é possível garantir uma compatibilidade com o caso de Schwarzschild uma vez que os resultados dependem fortemente do raio orbital e do ângulo de observação. Observámos ainda que a distribuição de massa tem um impacto subdominante nos modelos. Posto isto, modelos ultra compactos de gravastars são candidatos plausíveis a objetos alternativos a buracos negros, que conseguem reproduzir a sua aparência visual. Por último, referimos algumas limitações nos modelos considerados, como a consideração de objetos compactos estáticos ou a simplificação no modelo da fonte de emissão.

O principal objetivo desta investigação é, para além de distinguir buracos negros de gravastars, disponibilizar meios de deteção de gravastars no futuro, sendo que esperamos que as próximas gerações do EHT e do instrumento GRAVITY sejam precisos o suficiente para fazer tal distinção.

**Palavras chave:** gravastar, objetos compactos, assinaturas observacionais, hot spot, buraco negro

# Abstract

This thesis focuses on analyzing specific observable imprints of static thin-shell gravastars and compare them to the observational signatures of a Schwarzschild black hole. The thin-shell model of the gravastar is defined by two free parameters: the gravastar radius and the mass distribution ratio within the thin-shell. We investigate the effects of these parameters as well as observation inclination and orbital radius, when these objects are orbited by a hot-spot, by using the GYOTO software, a numerical backward ray-tracing code, to simulate the observational outcomes. For this astrophysical framework, we find that all the parameters have different impacts on the observed features with exception of the mass distribution, which plays a sub-dominant role, having a negligible impact. Our analysis also reveals that the astrometrical observational properties of ultra-compact gravastars closely resemble those of other ultra-compact objects, such as fluid stars and bosonic stars. However, low-compacticity configurations exhibit a more prominent and intense plunge through image, in the time-integrated flux. Additionally, ultra-compact gravastar configurations harbor light rings, being plausible candidates for mimicking black holes, while low-compacticity configurations do not feature light rings and thus a similarity to black holes is not guaranteed. These qualitative distinctions in observational properties between gravastars and black-hole spacetimes could potentially be discerned by the next generation of interferometric experiments in gravitational physics.

**Keywords:** gravastar, compact object, observational signatures, hot spot, black hole

# Preface

The official research presented in this document was conducted at the Instituto de Astrofísica e Ciências do Espacço (IA) and the Departamento de Física da Faculdade de Ciências da Universidade de Lisboa, with support from the research grants UIDB/04434/2020, UIDP/04434/2020. The research was supervised by Professor Francisco S.N. Lobo, from the Instituto de Astrofísica e Ciências do Espaço (IA) and the Departamento de Física da Faculdade de Ciências da Universidade de Lisboa (FCUL), and co-supervised by Professor João Luís Rosa, from the Institute of Physics of the University of Tartu, Estonia and Institute of Theoretical Physics and Astrophysics of the University of Gdańsk, Poland.

Part of the work included in this dissertation was published in Physical Review D ([1]), done in collaboration with Professor Francisco S.N. Lobo, Professor João Luís Rosa, and Professor Caio F. B. Macedo:

- Rosa, J. a. L., Cordeiro, D. S. J., Macedo, C. F. B. & Lobo, F. S. N. Observational imprints of gravastars from accretion disks and hot spots. Phys. Rev. D 109, 084002. https://link.aps.org/doi/10.1103/PhysRevD.109.084002 (8 2024).

In addition, the material in [1] was presented at a national conference in talk format:

- Daniela S. J. Cordeiro, "Observational signatures of hot-spots orbiting Gravastars ", XVI Black Holes Workshop, $20^{th}$ of December, 2023, Faculdade de Engenharia da Universidade do Porto, Porto, Portugal.

# Índex

# List of Figures

# List of Tables

# Chapter 1

# Introduction

This chapter focuses on reviewing the foundational concepts required to understand this dissertation. In the first section, we begin with an introduction to **B**lack **H**ole**s** (BHs), namely their origin, physical properties, formation mechanism and observational features. Additionally, we address the challenges posed by BH spacetimes and explore alternative objects that offer solutions to these challenges while exhibiting similar observational signatures. The previous discussion culminates in the motivation behind this work, which is presented in the second and final section.

## 1.1 Literature Review

### 1.1.1 Black Hole spacetimes

The theoretical prediction of the existence of BHs is usually associated with the $20^{th}$ century, more specifically with Einstein's theory of relativity. However, the BH concept dates back to the $18^{th}$ century to John Michell, who discovered that, if the escape velocity of a massive star is larger than the speed of light, the light of this star would never be able to escape its gravitational pull and would not reach an observer on Earth, making this star "invisible" [2]. After Michell's insight, in 1796, the mathematician Laplace reasoned in his work *Exposition du Système du Monde* that "The largest bodies in the universe may thus be invisible by reason of their magnitude" [3]. His statement was purely qualitative, but later in 1799 he provided a mathematical proof for the existence of these "dark stars" [4]. However, the light debate between Newton's particle theory (1704) and Thomas Young wave theory (1799) [5] led scientists to abandon the idea that such objects existed.

In 1905, Einstein published five papers among which he introduced the theory of Special Relativity [6]. This theory is mainly based on two postulates: the universality of the laws of physics in any inertial reference frame and the constant value of the speed of light in vacuum. This led to many consequences known nowadays as the time dilation, length contraction, the relativity of simultaneity, among others. This framework was extended to include gravity when, in 1915, Einstein published the **G**eneral **R**elativity (GR) theory, based on the equivalence principle that gravity is equally experienced in a massive body as it is in an accelerated reference frame [7]. Einsteins' GR theory has been responsible for a remarkable number of predictions, such as the gravitational light deflection, the existence of BHs, the precession of orbits and gravitational time dilation. In December of 1915, Schwarzschild found the first exact spherically symmetric solution to the vacuum EFE, which described a static, non-charged and non-rotating black hole [8].

## 1. INTRODUCTION

A BH is, by its formal definition, a region in spacetime that has a gravitational field so intense that precludes even light from escaping its pull [9]. This region in spacetime has a boundary which separates the exterior from the interior of the BH, known as the **E**vent **H**orizon (EH), term coined by Rindler in 1956 [10]. The EH is a null, i.e lightlike hypersurface [11, 12], located at a fixed radial coordinate $r_s = 2M$, defined as the Schwarzschild radius, past which particles can never escape to infinity, precluding us from seeing inside of it. However, BH solutions have a singularity present, causing a breakdown in the metric and the understanding of the physics behind it. Besides, there was a lack of consensus among scientists about the capacity of nature to admit a body with a size comparable to its gravitational radius. Due to this, the field of very compact gravitational systems remained dormant until research conducted in the 1930's by Oppenheimer and Volkoff [13] concerning the existence of stars with a radius very close to the gravitational radius, known as neutron stars, and from Oppenheimer and Snyder [14] in describing a BH's formation mechanism as the complete gravitational collapse of a massive star. The most common end state of a star are white dwarfs, since their highest possible mass, first deduced in 1931 and known as the Chandrasekhar mass limit, is taken to be $1.44M_{\odot}$, where $M_{\odot} = 2 \times 10^{33} g$ [15–17]. When this limit is surpassed, the star collapses to further smaller radius, originating neutron stars that possess strong magnetic fields. On the other hand, the Oppenheimer-Volkoff mass limit for a neutron star is around $2.2 - 2.9M_{\odot}$ [13, 18], and once stars with higher masses than this limit start to collapse, no equilibrium state can be found. The core continues collapsing to radius smaller than $2M$, eventually forming a Black Hole [11, 19].

A Black Hole is described by three quantities: its mass, its electric charge and its spin, meaning that different solutions depend on the discriminated combination of these parameters. Scientists have categorized several types of BHs by their mass, in which we highlight Stellar and Supermassive BHs. The most predominant type of BHs in our Universe are stellar BHs which are formed by the aforementioned process of gravitational collapse and are expected to have tens to hundreds of solar masses [20]. In contrast, supermassive black holes can be millions of times more massive than stellar black holes and are thought to be found in the center of galaxies [21]. The gap in size between stellar and supermassive BHs suggests the existence of some intermediate stage, however, such a type of BH still lacks evidence supporting their existence [1] [22, 23]. The field of extreme compact objects gained new insights in 1963 when Kerr discovered a solution to the EFEs describing a chargeless but rotating BH [24]. Besides Schwarzschild and Kerr BHs, other solutions were found like the charged spinless Reissner-Nordström BH, [25–28], and the rotating and charged Kerr-Newman BH [29, 30]. Besides these, there is a huge variety of solutions to the EFEs that describe extreme compact objects [24, 25, 27, 30–34]. Note that, it was not until 1967 that the term black hole was first used by Wheeler [35]. For a more detailed historical review the reader is referred to [12, 36].

### 1.1.2 Detection and Imaging of Black Holes

To detect a BH it is necessary to study the effects that these objects have on their surrounding environment. One example is by studying the effects of nearby matter, when gases and dust fall towards the BH, creating a disk of particles referred to, in the literature, as an accretion disk [37]. The study of these features has already been proven useful in revealing the unique observational signatures of extreme compact objects. [38–45]. Another example are particle jets, normal to the accretion disk's plane, that emerge from opposite directions of the BH. These jets, as well as infalling matter, emit X-rays which can be detected by our telescopes [11, 46].

[1] This is also known as the BH upper mass gap problem.

The field of strong gravitational systems was still overlooked until the discovery of what was thought to be a black hole, in an X-ray binary (Cygnus X-1) in 1965 [38]. The field of black hole imaging was officially born in 1973 with the studies of Bardeen in gravitational lensing by Kerr BHs [47]. Later that year, Bardeen, together with his PhD student Cunningham, discussed the appearance of the primary and secondary image of a star orbiting an extreme rotating BH [48]. In 1978, Palmer et al. simulated the impact that a Kerr BH has on a background star field, illustrating the effects of gravitational lensing [49]. Inspired by this work, in the following year Luminet produced the first hand-drawn image of a static BH surrounded by a geometrically thin rotating accretion disk [43]. The prospect of testing these theoretical predictions became a reality when the extension of the **V**ery **L**ong **B**aseline **I**nterferometry (VLBI) to sub-millimeter wavelengths, proved to be a technique capable of imaging the compact object (Sgr A$^*$) [50, 51]. This VLBI extension was only possible by combining various radio telescopes into an Earth-sized interferometer, known as the "**E**vent **H**orizon **T**elescope" (EHT) collaboration [52]. The first image of the central compact object in the galaxy M87 was revealed by the EHT, in 2019, followed by images of SgrA$^*$ in 2022, both proving the existence of an ultra compact object. In the future, the EHT team intends to expand the amount of telescopes in the collaboration and thus increase the resolving power and sensitivity to produce sharper images. For a further developed history in the black hole imaging field, the reader is referred to [53].

Since stellar motion is only determined by gravitational forces, another way to detect the presence of an extreme compact object is by monitoring the orbits of nearby stars. For example, the presence of a massive body in the galactic centre was confirmed by following the innermost orbits of stars (S-stars) with high-resolution near-infrared techniques [54]. Lastly, the **G**ravitational **W**ave**s** (GWs) produced by black holes rotating in a binary system can provide another method of detecting these objects. The **L**aser **I**nterferometer **G**ravitational-waves **O**bservatory (LIGO) [55] and the Virgo [56] instruments (among others) were built with the aim to detect these signatures. In 2016, the LIGO/Virgo collaboration officially announced the first detection of a GW from a binary BH merger [57, 58], which strengthened the hypothesis that BHs might really exist.

When an emitting source orbits near a BH, its light rays are deflected due to the accentuated curvature present in the vicinity of such a compact object, displaying unique observational signatures in a distant observer's screen. Such features are composed by sets of bright rings and a dark region that resembles a shadow. The concept of black hole shadow can be interpreted as the dark silhouette of the BH against a bright background [59]. Regarding its origin, the notion of shadow was inspired by the work of Bardeen (1973) [47], who described an "apparent boundary" as the closed curve that divides the region where lightlike geodesics cross the horizon, from a region where the geodesics miss the horizon. However, the first time the term 'shadow' was introduced was in 1999 by Falcke et al. [50]. The authors considered a geometrically thick but optically thin accretion disk, surrounding a black hole, and defined the **shadow** as the region inside of the apparent boundary, also known as the **critical curve** [60]. For a complete analysis and calculation of the shadow of a BH and other compact objects, the reader is referred to Perlick and Tsupko [59], see also Cunha and Herdeiro [61] for a brief review over this matter.

Let us now consider a Schwarzschild BH surrounded by an isotropically emitting source, like a star or a hot spot. Assuming an observation inclination of $i = 20^\circ$, the anticipated observational signatures from this scenario are depicted in figure 1.1 where three distinct features are discernible: an outer bright region, an outer ring, and a subsequent fainter and thinner ring. Similarly to several authors, we categorize these images by the number of half-orbits $n$ completed between their source and the observer's screen [62–74]. Light rays that perform less than a half-orbit ($n = 0$) around the BH constitute the outer bright region, often referred to as the **primary** or **direct image**. Photons that complete one half-orbit ($n = 1$)

correspond to the **secondary image** (the outer ring in figure 1.1), while those that complete at least a full orbit ($n \geq 2$) around the compact object are assigned as higher-order images (the faint ring observed in the right side of figure 1.1) [73, 74]. We refer to the higher-order images as "**light ring photons**" or "**light ring contribution**". Note that the primary image is weakly lensed, corresponding to the direct emission from the front side of the source, while the secondary image corresponds to the lensed image of the back side of the source. Regarding the LR photons, specifically the ones that complete a full orbit around the center ($n = 2$), they generate an additional image of the source's front side. Note that the images of the disk produced by the photons who perform at least a half-orbit (secondary image and LR photons) are demagnified and distorted [60].

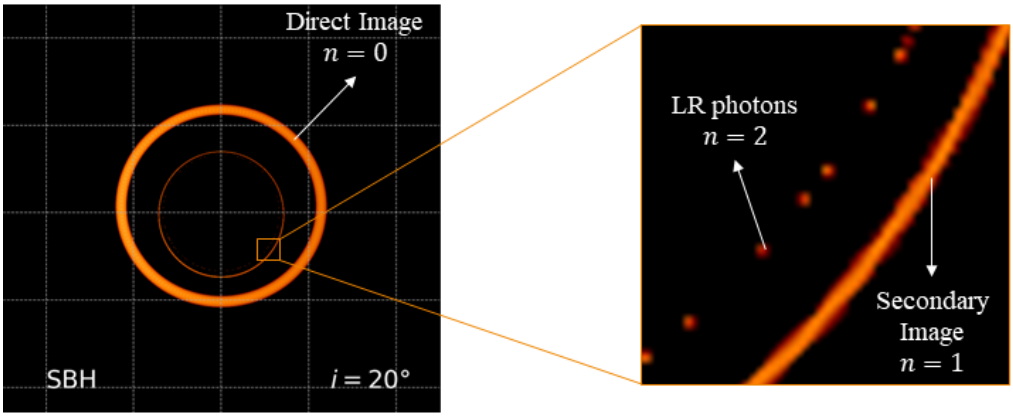


Figure 1.1: **Left Panel:** Time integrated images obtained with the GYOTO software of an isotropically emitting source orbiting a Schwarzschild BH at a radius $r_o = 8M$ and with an observation angle of $i = 20°$. **Right Panel:** A close up of the left panel image. The direct image ($n = 0$), secondary image ($n = 1$) and the LR contribution ($n = 2$) are highlighted.

### 1.1.3 Problems with Black Hole spacetimes

Until this point, our focus has been on introducing and providing evidence for the existence of BHs, namely the detection of gravitational waves, x-ray sources, the EHT images, and the examination of star trajectories near the galactic center. Despite being a simple solution with plenty theoretical support, BH spacetimes also present some challenges. As discussed earlier in this section, a BH is born when a massive star undergoes complete gravitational collapse, resulting in all its matter being compressed into an infinite density at the central singularity. In fact, Penrose and Hawking demonstrated that singularities necessarily emerge regardless of symmetry, if a closed trapped surface [2] exists or the matter within satisfies the strong energy condition [75, 76]. However, the presence of singularities is not desirable, since they are associated with geodesic incompleteness and the breakdown of spacetime. Additional challenges appear when we leave classical GR and start considering the quantum effects in BH spacetimes [77]. In classical theory, BHs can only absorb radiation without emitting any, whereas Hawking's work in quantum physics revealed that a BH emits thermal radiation [78]. Additionally, the author demonstrated that this effect leads to a negative heat capacity [79], and according to the principles of quantum statistical mechanics, "the heat capacity of any system in stable equilibrium at a fixed temperature must be positive" [77]. A consequence from having a negative specific heat, is that BHs are unstable to thermodynamical fluctuations. Another consequence of Hawking's discovery is the implication of an enormous BH entropy. When the black hole's mass $M$ equals the solar mass $M_\odot$, its entropy is 19 orders of magnitude

[2] Corresponds to a spacelike sphere $S^2$ that is found in the empty region, surrounding the matter that has contracted within $r = 2M$ [75].

greater than the entropy of the sun. This immense increase in entropy implies an enormous number of microstates at the horizon, which cannot be explained since the horizon only represents a mathematical surface [77]. Usually, the influence of Hawking radiation on classical geometry is disregarded, and thus, the BH background is often assumed to be fixed. However, thermal perturbations with large transplanckian temperatures and energies, are anticipated to alter the geometry near the horizon, deviating from the Schwarzschild solution, becoming unclear why neglecting the back-reaction effects of Hawking radiation on the classical geometry should be deemed valid [77, 80]. Lastly, BH spacetimes have an event horizon which is linked with a loss of information, since a BH evaporates through Hawking radiation. Its final state only encodes information about the total mass, electric charge, and angular momentum of the initial state. However, there are multiple possible systems with the same initial configuration of mass, electric charge and angular momentum that could lead to similar final states. According to classical and quantum principles, the state of a system at one point in time should determine its state at any other time, therefore, detailed information about the initial state would be irretrievably lost, resulting in what is known as the information loss paradox [77, 81].

### 1.1.4 Black Hole Mimickers

**E**xotic **C**ompact **O**biect**s** (ECOs) constitute a category of horizonless astrophysical objects with strong gravitational fields, and were introduced as potential candidates capable of mimicking the observational features of BH spacetimes, without their inherent limitations. [82]. The ECOs that are capable of reproducing similar observational signatures to those of BHs are known as Black Hole Mimickers [83, 84]. Additionally, the term "compact" in ECO denotes objects with a radius of $r \leq 6M$, while an ultra compact object has a radius of $r \leq 3M$ [85]. Figure 1.2 presents a table retrieved from [82] which shows a wide variety of ECOs along with categories mentioned or unmentioned in the literature. Since bosonic and fluid stars have already been examined in previous studies on observational signatures [86–88], our focus, for now, is on these two types of ECOs. Boson stars were originally called *geons*, particle-like solutions that couple GR with electromagnetism [89, 90]. However, these objects were unstable, which motivated Kaup to replace electromagnetism for a complex scalar field $\Phi$, and thus finding Klein-Gordon *geons* that we know today as boson stars [91]. For a review on boson stars the reader is referred to [92–94]. On the other hand, Schwarzschild relativistic fluid spheres (or stars) are described by two distinct regions: an interior populated by a relativistic fluid and an external Schwarzschild vacuum solution, which are separated by a hypersurface or thin shell [88, 95–98]. For a discussion on the formation, stability, electromagnetic signatures and GWs of bosonic and fluid stars the reader is referred to [85], more specifically to the references therein present in Figure 1.2.

In [87, 88] it was concluded that, regardless of the observation inclination considered, ultra compact configurations of bosonic and fluid stars display similar features to those of BHs with a primary track, a secondary track, LR photons, but also additional tracks, one corresponding to an extra LR contribution and two inner secondary tracks. On the other hand, it was showed that the amount of tracks present for less compact configurations depend strongly on the observation angle being considered. However, with the increase of the observation inclination, an additional new track emerges, corresponding to the photons that reach the observer from crossing directly the star in the middle, which the authors called the **plunge-through image**. It was also concluded that compacticity is the most dominant parameter when the interactions between the matter of the compact object and photons are neglected, presenting the gravastar model as a possible exception to this case [88]. Since the gravastar is a fairly discussed object in literature (see Figure 1.2) and has potential distinct observational signatures when orbited by

hot spots from the other ECOs, they are the chosen object to study in this dissertation.

The term Gravastar derives from **Gra**vitational **va**cuum **star**, whose model was first proposed by Mazur and Mottola in 2001 [80], consisting in a five-layer construction with: an interior de Sitter core, an interior thin shell connected to a finite region of stiff matter with equation of state $p = \rho$ where the horizon was expected, and an exterior thin-shell connecting it to the external Schwarzschild vacuum. A couple of years later, Visser and Wiltshire proposed a simpler three-layer construction with a repulsive de Sitter interior linked to a Schwarzschild exterior by a single thin-shell located at $r > r_s$, known as the thin-shell gravastar [99]. The presence of this transition hinders the formation of an event horizon and thus also lacks a singularity, providing a resolution to the information loss paradox. Note that there are also other gravastar constructions besides the one used in this work, such as gravastars supported by nonlinear electrodynamics [100]. The stability of the gravastars was studied under dynamical [101, 102], linear [97, 103], axial [104], thermodynamical [77] and radial [105–107], oscillations. However, if the gravastar is considered to be rapidly rotating, instabilities arise and this object turns to be unstable under scalar field perturbations [85]. Due to this and simplicity reasons, the gravastar model is considered to be static throughout this work.

| Model | Formation | Stability | EM signatures | GWs |
|---|---|---|---|---|
| Fluid stars | ✓ [90] | ✓ [85, 88, 109–113] | ✓ | ✓ [85, 109, 112, 114] |
| Anisotropic stars | ✗ | ✓ [115–117] | ✓ [118–120] | ✓ [115, 119, 120] |
| Boson stars & oscillatons | ✓ [53, 54, 121–123] | ✓ [86, 124–128] | ✓ [91, 129, 130] | ✓ [131–138] |
| Gravastars | ✗ | ✓ [127, 139] | ✓ [140–142] | ~ [112, 113, 135, 136, 138, 142–148] |
| AdS bubbles | ✗ | ✓ [149] | ~ [149] | ✗ |
| Wormholes | ✗ | ✓ [150–153] | ✓ [154–157] | ~ [136, 138, 148] |
| Fuzzballs | ✗ | ✗ (but see [158–161]) | ✗ | ~ (but see [135, 148, 162]) |
| Superspinars | ✗ | ✓ [163, 164] | ✗ (but see [165]) | ~ [135, 148] |
| $2-2$ holes | ✗ | ✗ (but see [166]) | ✗ (but see [166]) | ~ [135, 148] |
| Collapsed polymers | ✗ (but see [167, 168]) | ✓ [169] | ✗ [168] | ~ |
| Quantum bounces / Dark stars | ✗ (but see [170, 171]) | ✗ | ✗ | ~ [172] |
| Compact quantum objects* | ✗ [73, 173, 174] | ✗ | ✗ | ✓ [38] |
| Firewalls* | ✗ | ✗ | ✗ | ~ [135, 175] |

Figure 1.2: Catalogue of some ECOs, along with categories mentioned (tick), unmentioned (cross) and treated incompletely (~) in literature. An asterisk stands for BHs with a potential similar phenomenology to the other ECOs. Retrieved from [82].

## 1.2 Motivation

While the challenges associated with BH spacetimes, must be taken into account, it is imperative to not overlook the wealth of evidence supporting the existence of extremely compact objects. This motivated scientists to look for other alternative compact objects that circumvent the aforementioned issues, but that can still reproduce the characteristic signatures of BHs. These alternatives are collectively referred to as ECOs, also known as Black Hole mimickers. Among the wide variety of ECOs, this thesis concentrates on gravastars, an object that is recently gaining more attention for several reasons. Gravastars are horizonless compact objects that offer various solutions to the challenges posed by BHs. Additionally, they have been associated with dark energy, prompting speculation among scientists about their potential connection to the accelerated expansion of the Universe. The latter topic sparks some controversy and despite its interesting nature, it is not the focus of our investigation. Our goal is to find the inherent observational features of gravastars and compare them with the SBH and other previously studied ECOs. Note that, despite the Kerr hypothesis stating that the complete gravitational collapse results in the formation of a Kerr black hole [24, 75, 108, 109], static metrics are considerably simpler than rotating spacetimes and rotation has been proven to play a subdominant role, only affecting the results quantitatively [110]. Due to this, we chose to use static and spherically symmetric spacetimes throughout this dissertation.

The GRAVITY instrument [111–115] detected eight infrared flares [116], in the galactic center, indicating strong inhomogeneities in the accretion disk [117]. These inhomogeneities, thought to arise in reconnecting events in a magnetised accretion disk, are called **H**ot **S**pots (HS). Recently, it was shown that the flare activity is well fit by hot spots orbiting near the ISCO (see Figure 1.3) [118]. The GRAVITY collaboration constrained the orbits of the hot spots to be between $7M$ and $10M$ and concluded that smaller hot spots provide better fits to the observations. It is also expected that, at high inclinations, there will be more variations in brightness due to the Doppler beaming between the approaching and receding parts of the orbit [118]. They are also considered a great tool to discriminate between black holes and other horizonless compact objects. Due to this, the emission source considered in this dissertation is a hot spot (also referred to as an isotropically emitting source).

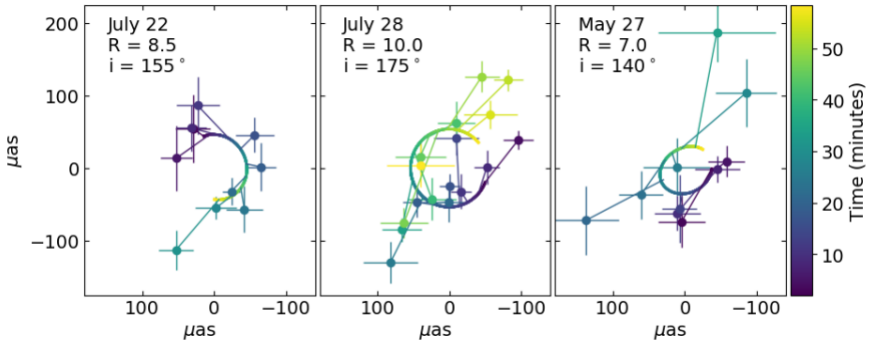


Figure 1.3: Data and nero fits of the three flares detected by GRAVITY. The solid lines show the orbits that best fits each of three flares. Colors indicate the time since the start of the flare. Image retrieved from [118].

Overall, we want to provide an answer for the following questions: What are the observational signatures of hot spots orbiting gravastars? What are the implications of compacticity, mass distribution, observational inclination and orbital radius in the observational properties of a gravastar? Are the results distinct from other previously studied ECOs? Which configurations of gravastars yield similar features to those of BHs? Namely, which set of parameters of gravastars lead to plausible BH mimicker candidates?

To answer these questions this dissertation is organized as follows.

In Chapter 2, we review the mechanics of BHs, where we begin by presenting the EFEs as well as the Schwarzschild and the de Sitter solutions, since these are necessary to comprehend the gravastar model. Besides this, we derive the generic geodesic equation and restrict our analysis to the particular case of a static, spherically symmetric spacetime. This is followed by the deduction of the effective potential which allows one to study circular null and timelike geodesics. Finally, we apply the previous analysis to the Schwarzschild BH case to determine the location of light rings in this spacetime.

In Chapter 3, we delve into the theoretical underpinnings of gravastars, specifically, into the thin-shell model that is employed in this work. In the first section we focus on the line element description of a gravastar, followed by a mathematical derivation of the junction conditions, along with a description of the gravastar's free parameters: compactness and mass distribution. The chapter culminates in an analysis of the photon effective potential to uncover the existence and stability profile of light rings.

In Chapter 4, we focus on the methodology behind this work, specifically the ray-tracing code GYOTO, used to perform the simulations. We present the implementation method, followed by a theoretical section on the ray-tracing functionality of the code, including the integration of geodesics and radiative transfer processes. The final section in this chapter examines the outputs that are generated by the code and the various parameter configurations used to obtain the results in chapter 5.

In Chapter 5, we present the time integrated images, magnitude, and centroid results, categorized into ultra compact and less compact solutions. We also discuss the impacts of observation inclination, compactness, orbital radius and mass distribution.

In Chapter 6, we attempt to address the questions previously proposed in this section while discussing the obtained results. Finally, we examine some of the limitations in this study and in gravastars, and propose prospects for future research.

# Chapter 2

# A review on Black Hole Mechanics

In this chapter, we centre our attention on the mathematical concepts and equations that are essential to understand this dissertation. The first section focuses on the mathematical foundations of GR by presenting the EFEs and define the necessary quantities behind the theory. Besides this, two solutions to these equations are presented: the Schwarzschild solution and the de Sitter solution, each one with its own subsection. In the second section we derive the equations of motion along a geodesic for a general case and the particular case of a static, spherically symmetric spacetime. This is followed by the study of circular null and timelike geodesics, specifically, by the deduction of the effective potential and the orbital velocity in this context. Lastly, we analyze the geodesic motion and photon effective potential, for a Schwarzschild BH, to determine the location of circular null geodesics and define concepts like innermost stable orbit or impact parameter.

## 2.1 The Einstein Field Equations

The relativistic Einstein Field Equations considering a case where there is a vacuum or matter, are respectively given by:

$$R_{\mu\nu} = 0 \quad \text{(vacuum)}, \tag{2.1}$$

$$G_{\mu\nu} = R_{\mu\nu} - \frac{1}{2} R\, g_{\mu\nu} = \kappa T_{\mu\nu} \quad \text{(matter)}, \tag{2.2}$$

where $G_{\mu\nu}$ is the Einstein tensor, which is symmetric $G_{\mu\nu} = G_{\nu\mu}$, $R_{\mu\nu}$ is the Ricci tensor which is linked to the Riemann curvature tensor, $R^{\alpha}_{\beta\mu\nu}$ as $R_{\mu\nu} = R^{\alpha}_{\mu\alpha\nu}$ and is given by

$$R_{\mu\nu} = \Gamma^{\sigma}_{\mu\nu,\sigma} - \Gamma^{\sigma}_{\sigma\mu,\nu} + \Gamma^{\sigma}_{\sigma\rho}\Gamma^{\rho}_{\mu\nu} - \Gamma^{\sigma}_{\mu\rho}\Gamma^{\rho}_{\sigma\nu}, \tag{2.3}$$

where $\Gamma^{\sigma}_{\mu\nu}$ are the Christoffel symbols

$$\Gamma^{\sigma}_{\mu\nu} = \frac{1}{2} g^{\sigma\lambda} \left( g_{\lambda\mu,\nu} + g_{\lambda\nu,\mu} - g_{\mu\nu,\lambda} \right), \tag{2.4}$$

and $g_{\mu\nu}$ is the metric tensor which is symmetric and satisfies the relation $g^{\mu\nu} g_{\nu\sigma} = \delta^{\mu}_{\sigma}$ where $\delta^{\mu}_{\sigma}$ is the Kronecker delta which is one if $\mu = \sigma$ and zero if $\mu \neq \sigma$. Note that the metric tensor and its inverse can be used to lower or raise indices on tensors or vectors (e.g. $g^{\mu\nu} x_{\nu} = x^{\mu}$) and the "," denotes the partial derivatives with respect to the coordinate that follows. Still regarding the EFEs, $R$ is the Ricci scalar obtained by $R = g^{\mu\nu} R_{\mu\nu}$, $T_{\mu\nu}$ is the energy-momentum tensor and $\kappa$ is a constant with value $\kappa = 8\pi G$. Note that Greek indices assume the Einstein summation notation for the four coordinates

$\mu, \nu = \{0,1,2,3\}$, while Latin indices run over only the spatial coordinates $i, j = \{1,2,3\}$.

A new term was later introduced in Eq. (2.2) containing a cosmological constant $\Lambda = 8\pi G\rho$

$$G_{\mu\nu} = R_{\mu\nu} - \frac{1}{2} R\, g_{\mu\nu} + \Lambda g_{\mu\nu} = \kappa T_{\mu\nu} \quad , \tag{2.5}$$

that is nowadays linked with the concept of dark energy. For a deeper discussion of GR the reader is referred to [11, 19, 119–121].

### 2.1.1 The Schwarzschild Solution

The first solution to the aforementioned vacuum equation was proposed shortly after the discovery of Einstein's equations. As discussed in the literature review, Schwarzschild found a spherically symmetric solution that describes a static, non-charged and non-rotating black hole. To understand better the solution, we introduce some concepts first, namely the line element and its specific form when considering static conditions and spherical symmetry. Once the necessary assumptions and calculations are introduced, it is possible to reach the desired solution. Ultimately, we perform an analysis and discussion of the metric singularities.

Let us first introduce the general line element of a spacetime

$$ds^2 = g_{\mu\nu} dx^\mu dx^\nu \tag{2.6}$$

where $ds^2$ corresponds to the square of the line element $ds$, $x^\mu$ to the four-dimensional coordinates $x^\mu = \{t, r, \theta, \phi\}$ and $dx^\mu$ to an infinitesimal displacement of these coordinates. Since Schwarzschild found a static and spherically symmetric solution, it is necessary to define the meaning of these assumptions. The static condition implies that the metric tensor is independent of the time coordinate and the line element does not have any time-space cross components like $dtdx^i$, where $i$ only runs over the spatial coordinates. On the other hand, the spherically symmetric condition requires the presence of the surface element of a unit two-sphere $d\Omega^2 = d\theta^2 + \sin^2\theta d\phi^2$ and imposes the vanishing of spatially cross components $dx^i dx^j$, leaving one free to multiply the terms in the metric by any function of r. With this being said, the static and spherically symmetric space-time element is given by (for the whole deduction see for e.g refs [11, 19])

$$ds^2 = -f(r)\, dt^2 + g(r)\, dr^2 + r^2 d\Omega^2 \tag{2.7}$$

where from now on we shall omit the r-dependence of $f(r)$ and $g(r)$. Since we want to find the solution for the vacuum equation, the goal is to solve Eq. (2.1). Inserting this metric in the field equation and recurring to the Eqs.(2.3)-(2.4), we obtain

$$\frac{f'}{f} = -\frac{g'}{g}, \tag{2.8}$$

and so the multiplication of both functions $fg$ must be a constant. In infinity, the metric tensor must approach the Minkowski metric $\eta_{\mu\nu} = (-1,1,1,1)$ and consequently $f \longrightarrow 1$, $g \longrightarrow 1$. Due to this, it is possible to infer that $fg = 1 \Longrightarrow g = 1/f$. By inserting this definition of $g$ in $R_{\theta\theta} = 0$ we obtain

$$(rf)' = 1, \tag{2.9}$$

where its integration leads to

$$f = 1 + \frac{A}{r}, \tag{2.10}$$

where $A$ is a constant of integration. In the weak field limit it is proven that $g_{tt} = -(1+2\Phi)$ [11, 19, 119], where $\Phi$ is a scalar field corresponding to the gravitational potential $\Phi = -GM/r$, which compared with the previous equation and recalling from Eq. (2.7) that $g_{tt} = -f$, one can conclude that $A = -2GM$. The Schwarzschild spherically symmetric solution can then be written as

$$ds^2 = -\left(1 - \frac{2M}{r}\right) dt^2 + \left(1 - \frac{2M}{r}\right)^{-1} dr^2 + r^2 \left(d\theta^2 + \sin^2\theta d\phi^2\right), \tag{2.11}$$

where natural units were assumed ($G = 1$, $c = 1$) and the metric is asymptotically Minkowski as previously required. For a more detailed description of the steps, the reader is advised to check Refs. [11, 19, 120, 122, 123].

Once the Schwarzschild metric is deduced, one can turn to its analysis. Note that at $r_s = 2M$, the time component of the metric tensor tends to zero, $g_{tt} \longrightarrow 0$ implying that the radial component becomes infinite $g_{rr} \longrightarrow \infty$. Not only the opposite behaviour is present for $r = 0$ but also the vanishing of the angular components $g_{\theta\theta},\ g_{\phi\phi} \longrightarrow 0$. The presence of points that lead to metric infinities, also called *singularities*, causes a breakdown in the space-time being an indication that some mathematical problem arises at these coordinates. However, it is probable that we have a coordinate singularity, related to the chosen coordinate system, rather than a physical singularity. To discern between the two and find if whether the previous singularities are coordinate-related or geometry-related we recur to the following criterion: If the curvature becomes infinite for a set of coordinates then we are looking at a physical singularity [11]. One way to test this is by computing the curvature scalar $R_{\alpha\beta\mu\nu}R^{\alpha\beta\mu\nu}$, using Eq. (2.3), for the Schwarzschild metric

$$R_{\alpha\beta\mu\nu}R^{\alpha\beta\mu\nu} = \frac{48G^2M^2}{r^6}. \tag{2.12}$$

By looking at the previous equation one can conclude that $r = 0$ represents a real singularity of the metric, meaning that geodesics are incomplete at this point. On the other hand, at $r_s = 2M$ no infinities appear in the curvature and thus the singularity can be removed when considering a different coordinate system, e.g. Eddington-Finkelstein [124, 125] or Kruskal-Szekeres coordinates [126–128]. We now want to see the implications of this radius in the metric. For $r > r_s$ we have $g_{tt} < 0$ and $g_{rr} > 0$ meaning that $t$ and $r$ are timelike and spacelike coordinates, respectively. However, crossing $r_s$ reverses the roles of time and space, since for $r < r_s$ we have $g_{tt} > 0$ and $g_{rr} < 0$ [128]. But what is the physical meaning behind this change of roles in the spatial and time coordinates? At a radial coordinate larger than $2M$, any object can change its position by changing its motion and thus approximate or move further away from $r_s$. Nonetheless, once this critical radius is crossed, a decrease in $r$ starts to represent the passage of time, instead of a change in the position in space. Any in-falling particle has only one possible direction, that is for smaller and smaller values of $r$ until it reaches the singularity at $r = 0$ [128].

### 2.1.2 The de Sitter Solution

In 1917, Willem de Sitter derived a new solution to the EFEs with a cosmological constant, by assuming a matter-free Universe [129]. To better understand the implications of this assumption, let us first rewrite the EFE in (2.5), by taking the trace of the field equation and defining $T = g^{\mu\nu}T_{\mu\nu}$

$$R = 4\Lambda - \kappa T. \tag{2.13}$$

This expression can now be substituted in the Einstein equation for matter with a cosmological constant

$$R_{\mu\nu} - \Lambda g_{\mu\nu} = \kappa \left( T_{\mu\nu} - \frac{1}{2} g_{\mu\nu} T \right). \tag{2.14}$$

The assumption of neglecting any mass terms implies that the energy-momentum tensor as well as its contracted form are set to zero and thus the previous equation reduces to

$$R_{\mu\nu} = \Lambda g_{\mu\nu}, \tag{2.15}$$

being this the equation that we now want to solve. Note that the only difference from the Schwarzschild case is that the Ricci tensor assumes a non null value. Since the de Sitter solution is also static and spherically symmetric, the same reasoning present in the previous subsection until Eq. (2.9) is applicable here. The distinction is in $R_{\theta\theta}$ that now is equal to $R_{\theta\theta} = \Lambda g_{\theta\theta}$ and thus leads to a new differential equation

$$(rf)' = 1 - \Lambda r^2, \tag{2.16}$$

which integrated yields

$$f = 1 + \frac{A}{r} - \frac{1}{3}\Lambda r^2. \tag{2.17}$$

The de Sitter metric is obtained when the mass term vanishes $M = 0$ and so is given by

$$ds^2 = -\left(1 - \frac{8\pi G\rho}{3} r^2\right) dt^2 + \left(1 - \frac{8\pi G\rho}{3} r^2\right)^{-1} dr^2 + r^2 d\Omega, \tag{2.18}$$

where the value of the cosmological constant was replaced, being $\rho$ the energy density, and the constant $A$ assumed the same value as before. This solution is also often seen as a function of the expansion rate $H \propto \sqrt{\Lambda}$

$$ds^2 = -\left(1 - H^2 r^2\right) dt^2 + \left(1 - H^2 r^2\right)^{-1} dr^2 + r^2 d\Omega. \tag{2.19}$$

Note that regarding singularities, the metric becomes infinite when $r = H^{-1}$. However, following the same criterion in the previous section, the curvature does not produce any infinities, leading to the conclusion that this is a coordinate singularity rather than a physical one and that the de Sitter space has no geometric singularities [123].

## 2.2 Equations of Motion and Effective Potential

### 2.2.1 The Geodesic Equation

In a flat space, the shortest path possible between two points is a straight line while for a general space the shortest path becomes a *geodesic* [19]. The study of geodesics has been proven relevant in GR, since they are the paths that free falling test particles follow and thus are useful in the study of particle motion [11, 128]. In this subsection the goal is to briefly derive the general form of the geodesic equation. The derivation presented ahead follows Emanuele Berti's lectures on Black Hole Perturbation Theory [130].

The geodesic equation can be interpreted as an equation of motion along a geodesic and thus its generic construction derives from the Euler-Lagrange equation

$$\frac{d}{d\lambda}\frac{\partial \mathcal{L}}{\partial \dot{x}^{\alpha}} = \frac{\partial \mathcal{L}}{\partial x^{\alpha}}, \tag{2.20}$$

for the following Lagrangian density

$$\mathcal{L} = \frac{1}{2} g_{\mu\nu}\dot{x}^{\mu}\dot{x}^{\nu}, \tag{2.21}$$

where $\lambda$ is the affine parameter used in the parametrization of the geodesic. Note that in the previous equations, the overdots denote derivatives with respect to the affine parameter along the geodesics $\frac{dx^{\mu}}{d\lambda} = \dot{x}^{\mu}$. Let us first start with the left-hand side of the Euler-Lagrange equation, where the partial derivation must take into account the case when $\mu = \nu$

$$\frac{\partial \mathcal{L}}{\partial \dot{x}^{\alpha}} = \frac{\partial \mathcal{L}}{\partial \dot{x}^{\mu}} = g_{\mu\mu}\dot{x}^{\mu}, \tag{2.22}$$

and $\mu \neq \nu$

$$\frac{\partial \mathcal{L}}{\partial \dot{x}^{\alpha}} = \frac{\partial \mathcal{L}}{\partial \dot{x}^{\mu}} + \frac{\partial \mathcal{L}}{\partial \dot{x}^{\nu}} = \frac{1}{2} g_{\mu\nu}\dot{x}^{\nu} + \frac{1}{2} g_{\nu\mu}\dot{x}^{\mu} = g_{\mu\nu}\dot{x}^{\mu}, \tag{2.23}$$

so the general derivative can be written as

$$\frac{\partial \mathcal{L}}{\partial \dot{x}^{\alpha}} = g_{\mu\alpha}\dot{x}^{\mu}. \tag{2.24}$$

Taking the derivative to the affine parameter leads to

$$\frac{d}{d\lambda}\frac{\partial \mathcal{L}}{\partial \dot{x}^{\alpha}} = \dot{x}^{\mu}\frac{dg_{\mu\alpha}}{d\lambda} + g_{\mu\alpha}\frac{d\dot{x}^{\mu}}{d\lambda} = \dot{x}^{\mu}\dot{x}^{\nu}\partial_{\nu} g_{\mu\alpha} + g_{\mu\alpha}\ddot{x}^{\mu}, \tag{2.25}$$

where the notation $\partial_{\mu} = \frac{\partial}{\partial x^{\mu}}$ was introduced as well as the following property $\frac{dg_{\mu\alpha}}{d\lambda} = \frac{dx^{\nu}}{d\lambda}\frac{\partial g_{\mu\alpha}}{\partial x^{\nu}}$. Focusing now on the right-hand side, the result is immediate

$$\frac{\partial \mathcal{L}}{\partial x^{\alpha}} = \frac{1}{2}\partial_{\alpha} g_{\mu\nu}\dot{x}^{\mu}\dot{x}^{\nu}, \tag{2.26}$$

which combined with the one in Eq. (2.25) yields

$$g_{\mu\alpha}\ddot{x}^{\mu} + \dot{x}^{\mu}\dot{x}^{\nu} g_{\mu\alpha,\nu} - \frac{1}{2} g_{\mu\nu,\alpha}\dot{x}^{\mu}\dot{x}^{\nu} = 0. \tag{2.27}$$

Since $\dot{x}^{\mu}\dot{x}^{\nu}$ is symmetric under $\mu \longleftrightarrow \nu$ interchange, we can write $2\dot{x}^{\mu}\dot{x}^{\nu} g_{\mu\alpha,\nu} = \dot{x}^{\mu}\dot{x}^{\nu}\left(g_{\mu\alpha,\nu} + g_{\nu\alpha,\mu}\right)$ and hence

$$g_{\mu\alpha}\ddot{x}^{\mu} + \frac{1}{2}\dot{x}^{\mu}\dot{x}^{\nu}\left(g_{\mu\alpha,\nu} + g_{\nu\alpha,\mu} - g_{\mu\nu,\alpha}\right) = 0. \tag{2.28}$$

By multiplying $g^{\mu\alpha}$ in both terms of the previous equation and substituting the Christoffel symbols given by Eq. (2.4)

$$\ddot{x}^{\mu} + \Gamma^{\mu}_{\beta\lambda}\dot{x}^{\beta}\dot{x}^{\lambda} = 0, \tag{2.29}$$

we reach the usual and commonly known form of the geodesic equation.

### 2.2.2 Geodesics in Static, Spherically Symmetric Spacetimes

Since throughout this dissertation only static, spherically symmetric metrics are considered, we deduce the geodesic equations of motion for this specific case. Considering the generic form of these type of metrics in Eq. (2.7), the Lagrangian density in Eq. (2.21) can be rewritten as

$$2\mathcal{L} = g_{tt}\dot{t}^2 + g_{rr}\dot{r}^2 + r^2\left(\dot{\theta}^2 + \sin^2\theta\dot{\phi}^2\right). \tag{2.30}$$

Let us now introduce the notation $p^\mu = \dot{x}^\mu$ for the particle's four-momentum, which relates with the Lagrangian density as follows

$$\frac{\partial\mathcal{L}}{\partial\dot{x}^\mu} = g_{\mu\nu}\dot{x}^\nu = \dot{x}_\mu = p_\mu. \tag{2.31}$$

This allows one to associate the four components of the momentum with the coordinate derivatives

$$p_t = \frac{\partial\mathcal{L}}{\partial\dot{t}} = g_{tt}\dot{t}, \tag{2.32}$$

$$p_r = \frac{\partial\mathcal{L}}{\partial\dot{r}} = g_{rr}\dot{r}, \tag{2.33}$$

$$p_\theta = \frac{\partial\mathcal{L}}{\partial\dot{\theta}} = r^2\dot{\theta}, \tag{2.34}$$

$$p_\phi = \frac{\partial\mathcal{L}}{\partial\dot{\phi}} = r^2\sin^2\theta\dot{\phi}, \tag{2.35}$$

which can be replaced in the Euler-Lagrange equations

$$\frac{dp_t}{d\lambda} = \frac{\partial\mathcal{L}}{\partial t} = 0 \Longrightarrow -p_t = -g_{tt}\dot{t} = E, \tag{2.36}$$

$$\frac{dp_r}{d\lambda} = \frac{\partial\mathcal{L}}{\partial r}, \tag{2.37}$$

$$\frac{dp_\theta}{d\lambda} = \frac{\partial\mathcal{L}}{\partial\theta} = r^2\sin\theta\cos\theta\dot{\phi}^2, \tag{2.38}$$

$$\frac{dp_\phi}{d\lambda} = \frac{\partial\mathcal{L}}{\partial\phi} = 0 \Longrightarrow p_\phi = r^2\sin^2\theta\dot{\phi} = L. \tag{2.39}$$

Note that the static and spherical symmetry assumptions yield a Lagrangian that is independent of $t$ and $\phi$. Due to this, the partial derivatives with respect to these coordinates are null and two conserved quantities can be defined: the energy per unit mass $E = -g_{tt}\dot{t}$ (from the time-component) and the angular momentum per unit mass $L = r^2\sin^2\theta\dot{\phi}$ (from the angular-component). The latter can be simplified by restricting our analysis to the equatorial plane without loss of generality, i.e. by assuming $\theta = \pi/2$ and $\dot{\theta} = \ddot{\theta} = 0$, which reduces the angular momentum and the Lagrangian density, respectively to $L = r^2\dot{\phi}$ and

$$2\mathcal{L} = \frac{E^2}{g_{tt}} + g_{rr}\dot{r}^2 + \frac{L^2}{r^2} = -\delta, \tag{2.40}$$

where $\delta$ is a constant parameter that takes the value $\delta = 0$ (1) for null (timelike) geodesics. Note that null geodesics correspond to the shortest path traveled by massless particles (i.e. photons), while timelike geodesics to the shortest path traveled by massive particles [11, 128]. This allows one to define the effective potential for a circular null or timelike geodesic as deduced in the next subsection.

### 2.2.3 The Photon Effective Potential

Following the reasoning of the previous subsection, Eq. (2.40) can be rearranged and reduced to the same denominator

$$E^2 = -g_{tt}g_{rr}\dot{r}^2 - g_{tt}\left(\frac{L^2}{r^2} + \delta\right). \tag{2.41}$$

However, the only solutions used throughout this dissertation are those described in subsections 2.1.1 and 2.1.2, which satisfy the property $-g_{tt} = g_{rr}^{-1}$, hence

$$\varepsilon = V(r) + \frac{1}{2}\dot{r}^2, \tag{2.42}$$

resembles the total energy equation where $\varepsilon = E^2/2$ corresponds to the total energy [128, 131], the term $\dot{r}^2/2$ represents the radial kinetic energy and $V(r)$ is the one-dimensional potential defined as

$$V(r) = -\frac{1}{2}g_{tt}\left(\frac{L^2}{r^2} + \delta\right). \tag{2.43}$$

The analysis of the above effective potential can be very useful since it allows one to study the stability and location of circular orbits in null ($\delta = 0$) and timelike ($\delta = 1$) geodesics. The latter can, for example, provide insights of the orbital dynamics of the hot spot, while the former is useful for finding the paths of null geodesics from our source. Let us first focus on the study of circular null geodesics, also known as **L**ight **R**ings (LRs). By definition, circular orbits occur at a constant radius and are defined by $\dot{r} = \ddot{r} = 0$, implying that the effective potential in Eq. (2.42) becomes flat, $V(r) = \varepsilon$ and $V'(r) = 0$. Taking $\delta = 0$ allows one to write a simplified form of the effective potential in Eq. (2.43), for circular null geodesics

$$V_{phot}(r) = \frac{2V(r)}{L^2} = \frac{-g_{tt}}{r^2}. \tag{2.44}$$

If we multiply Eq. (2.42) by $2/L^2$

$$\frac{E^2}{L^2} = V_{phot}(r) + \frac{\dot{r}^2}{L^2}, \tag{2.45}$$

and insert the overdot notation, it is possible to obtain a new form for the equation of motion that depends on the impact parameter $b = L/E$

$$\left(\frac{dr}{d\lambda}\right)^2 = \frac{1}{b^2} - V_{phot}(r), \tag{2.46}$$

where the rescaling of the affine parameter $\lambda \longrightarrow L\lambda$ [131] was introduced.

On the other hand, taking $\delta = 1$ in Eq. (2.43) allows one to write the effective potential for timelike geodesics as

$$V_{part} = 2V(r) = -g_{tt}\left(\frac{L^2}{r^2} + 1\right). \tag{2.47}$$

Another important quantity is the orbital velocity $\Omega_c$ of a timelike circular orbit around a central object given by [130]

$$\Omega_c \equiv \frac{d\phi}{dt} = \frac{\dot{\phi}}{\dot{t}} = \frac{-g_{tt}L}{r^2E}, \tag{2.48}$$

where the chain rule $\frac{d\phi}{d\lambda}\frac{d\lambda}{dt} = \frac{d\phi}{dt}$ was inserted as well as the definitions of angular momentum and energy per unit mass. As mentioned above, a consequence of having circular orbits is that $V'(r) = 0$, which applied in Eq. (2.43) for $\delta = 1$, yields the following relation

$$-g_{tt} = \frac{r^3}{2L^2}\frac{d}{dr}(-g_{tt})\left(\frac{L^2}{r^2}+1\right), \tag{2.49}$$

that can be substituted in Eq. (2.48), reducing it to

$$\Omega_c = \frac{1}{2r}\frac{d}{dr}(-g_{tt})\left(\frac{L}{E}+\frac{r^2}{LE}\right). \tag{2.50}$$

Besides the previous condition, circular orbits also demand that $V(r) = \varepsilon = E^2/2$, where the effective potential can be substituted by its definition in Eq. (2.43) for $\delta = 1$, resulting in

$$\left(\frac{L}{E}+\frac{r^2}{LE}\right) = \left(\frac{1}{2r}\frac{d}{dr}(-g_{tt})\right)^{-\frac{1}{2}}, \tag{2.51}$$

where Eq. (2.49) was introduced. This relation can then be substituted in the previous formulation of the orbital velocity, leading to

$$\Omega_c = \sqrt{\frac{1}{2r}\frac{d}{dr}(-g_{tt})}, \tag{2.52}$$

which will be the formulation used in this dissertation.

In what follows, the equations deduced throughout this section are applied to the specific case of a Schwarzschild BH, aiming to unravel the motion of light and matter in the vicinity of such a compact object.

## 2.3 The Schwarzschild Black Hole

### 2.3.1 Geodesic Motion and Light Rings

Let us recall the deduction of the photon effective potential in Eq. (2.43). Looking now at the specific case of the Schwarzschild metric in Eq.(2.11) where $g_{tt} = -\left(1-\frac{2M}{r}\right)$, the generic effective potential reduces to

$$V^{Sch}(r) = 2V(r) = \left(1-\frac{2M}{r}\right)\left(\frac{L^2}{r^2}+\delta\right). \tag{2.53}$$

The analysis of this potential allows one to study the qualitative features of geodesic motion, namely the presence and stability of circular orbits. Circular geodesics are possible at stationary points, more specifically when $V(r) = \varepsilon$ and $V'(r) = 0$. Thus taking $\left(V^{Sch}\right)' = 0$ yields

$$L^2(r-3M) = \delta M r^2. \tag{2.54}$$

From this equality one can conclude that circular geodesics only exist for $r \geq 3M$. In the specific case of $\delta = 0$, circular null geodesics only exist at $r = 3M$. This corresponds to the radius where a LR is present, $r_{LR}$, which leads to three potential categorizations of LRs, considering the photon effective potential on Eq. (2.44):

1. When $V'_{phot} = 0$ and $V''_{phot} < 0$ the potential features a maximum which corresponds to an unstable LR;
2. When $V'_{phot} = 0$ and $V''_{phot} > 0$ the potential features a minimum which corresponds to a stable LR;
3. When $V'_{phot} = 0$ and $V''_{phot} = 0$ the potential features a saddle point which corresponds to a degenerate pair of LRs.

To characterize the type of LR present at $r_{LR} = 3M$, let us substitute the Schwarzschild metric in the photon effective potential

$$V_{phot} = \frac{1}{r^2}\left(1 - \frac{2M}{r}\right), \tag{2.55}$$

which is illustrated in figure 2.1, where a turning point corresponding to a maximum is visible. We conclude then, that LRs at $r_{LR} = 3M$ are unstable [11]. It is also possible to define a **P**hoton **S**phere (PS), with a radius of $r_{PS} = r_{LR} = 3M$, as the surface in which circular null geodesics orbit infinitely.

Focusing now in the definition of the photon potential considering the impact parameter $b = L/E$ in Eq. (2.46), note that the distance from a line of height $1/b^2$ to $V_{phot}$ corresponds to $\dot{r}^2$ [131] (see Figure 2.1). Consequently, for null circular geodesics, i.e. $\dot{r} = 0$, we retrieve the following relation

$$\frac{1}{b_c^2} = V_{phot}(r_c), \tag{2.56}$$

corresponding to the maximum of the effective potential, and where $b_c$ is defined as the critical impact parameter that separates the capture of light rays from the flyby orbits [59, 130]. In short, the critical impact parameter corresponds to the value of the impact parameter for which light rays asymptotically approach the LR, and so it can be obtained for $r_c = r_{LR}$

$$b_c = \sqrt{V_{phot}^{-1}(r_{LR})} = \sqrt{3 \times 9M^2} = 3\sqrt{3}M. \tag{2.57}$$

Let us imagine a massless particle falling from infinity. From figure 2.1 we can conclude that, if the photon does not overcome the potential barrier at $r = 3M$ then it is scattered away from the BH to infinity. On the other hand, if it overcomes the potential barrier then the photon is captured into the BH. The former (latter) situation occurs for an impact parameter larger (smaller) than the critical value $b > (<)3\sqrt{3}M$ [131]. Nonetheless, observing light below the critical impact parameter is feasible if the photons are emitted outward from a radius between $2M$ and $3M$.

To study the stability of circular orbits for massive particles (i.e $\delta = 1$ in Eq. (2.53)), we need to compute $\left(V^{Sch}\right)''$ by substituting $L^2$ from Eq. (2.54) in Eq. (2.53)

$$\left(V^{Sch}\right)'' = \frac{M(r-6M)(r-2M)}{r^2(r-3M)^2}. \tag{2.58}$$

We conclude that, timelike circular geodesics are stable for $r \geq 6M$, which explains the terminology used for $r = 6M$ as the **I**nnermost **S**table **C**ircular **O**rbit (ISCO), while unstable timelike circular geodesics exist between $3M$ and $6M$ [130].

Recalling the discussion in the previous and the present chapter, we distinguish between what occurs in the vicinity of a Schwarzschild BH and what is visible in a distant observer's screen. In the former case we define: the Event Horizon as a boundary with a radius of $r = 2M$; the Light Ring as a circular null geodesic which is present only for $r = 3M$; the Photon Sphere as the surface in which circular null geodesics orbit infinitely, at a radius of $r = 3M$. On the other hand, for the latter case we define:

the impact parameter $b$ as the radial distance from the centre of the observer's screen at which a given photon is observed; the critical impact parameter $b_c = 3\sqrt{3}M$, as the radial distance from the centre of the screen in which the LR photons reach the observer's plane; the critical curve as the theoretical projection of the photon sphere in the observer's screen, having a radius of $r = 3\sqrt{3}M$ [1]; the shadow as the region inside the critical curve; the direct image as the intersection of null geodesics that do not complete a half-orbit around the center ($n = 0$), with the observer's screen; the secondary image as the intersection of null geodesics that complete a half-orbit around the center ($n = 1$), with the observer's screen; the LR photons or LR contribution as the intersection of null geodesics that complete two or more half-orbits around the center ($n \geq 2$), with the observer's screen.

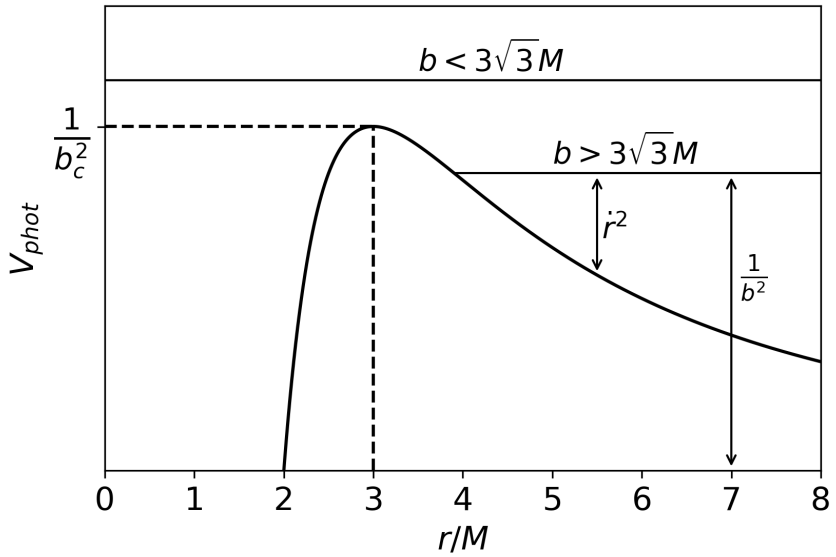


Figure 2.1: Photon effective potential $V_{phot}$ from Eq. (2.55) as a function of the normalized radial coordinate. The coordinates of the maximum in which circular null geodesics are possible are depicted, as well as the relation between the potential, $1/b^2$ and $\dot{r}^2$.

[1] Note that, we do not directly observe the critical curve, since the photons that reach an observer are asymptotic to the critical curve. The photons that correspond exactly to the critical curve remain trapped in the photon sphere, where they perform infinite orbits.

# Chapter 3

# Gravitational Vacuum Stars

This chapter is divided in two sections, the first focuses in the thin-shell gravastar model, more specifically in the line element representation and junction conditions while the latter turns to the geodesics and potential analysis.

## 3.1 Thin-shell model

### 3.1.1 Line element description

The general form of the stress-energy tensor for a static non-rotating body in a spherically symmetric geometry

$$ds^2 = -f(r)\,dt^2 + \frac{1}{h(r)}\,dr^2 + r^2(d\theta^2 + \sin^2\theta\,d\phi^2), \tag{3.1}$$

is given by

$$T^{\nu}_{\mu} = \mathrm{diag}\,(-\rho, p, p_{\perp}, p_{\perp})\,, \tag{3.2}$$

where $\rho$ is the energy density, $p$ is the radial pressure and $p_{\perp}$ is the transverse pressure. The Einstein equations (2.2) in static spherical coordinates are then reduced to

$$-G^{t}_{t} = \frac{1}{r^2}\frac{d}{dr}\left[r\,(1-h)\right] = -8\pi T^{t}_{t} = 8\pi\rho, \tag{3.3}$$

$$G^{r}_{r} = \frac{h}{rf}\frac{df}{dr} + \frac{1}{r^2}\,(h-1) = 8\pi T^{r}_{r} = 8\pi p, \tag{3.4}$$

together with the conservation equation

$$\nabla_{\nu} T^{\nu}_{r} = \frac{dp}{dr} + \frac{\rho + p}{2f}\frac{df}{dr} + \frac{2}{r}\,(p - p_{\perp}) = 0. \tag{3.5}$$

For a perfect fluid, $p = p_{\perp}$, which leads to the vanishing of the last term in Eq. (3.5). In this case, when an equation of state is defined for these regions, it is possible to solve Eqs. (3.3)–(3.5) for the functions $f$ and $h$. The gravastar model considered in this work is assumed to contain three different regions with two different equations of state:

1. Interior region: $\rho = -p$,

2. Thin Shell: $\sigma, \Pi$,

3. Exterior region: $\rho = p = 0$,

since we consider an infinitesimally thin shell with a specific surface energy density $\sigma$ and surface tension $\Pi$. In the exterior region, when substituting $p = \rho = 0$ in the conservation equation we obtain $\nabla_\lambda T_r^\lambda = 0$. The solution that satisfies this condition and approaches flat Minkowski spacetime as $r \longrightarrow \infty$ is the Schwarzschild solution (for the deduction see subsection 2.1.1). However, in the interior region, the substitution of the equation of state in equation (3.5), leads to $\frac{dp}{dr} = 0$, meaning that $\rho = -p$ is a constant, defined in the following discussion. Since this solution must also lack a curvature singularity at the origin, the interior region corresponds to a dS spacetime in static coordinates (for a deduction see subsection 2.1.2). Note that, despite the negative pressure, the matter satisfies the null energy condition $p + \rho \geq 0$, while the weak energy condition where $\rho > 0$ is only satisfied for certain model parameters, which will be further discussed in this section. With this being said, we consider a four-dimensional manifold $\mathcal{V}$ divided in the exterior region $\mathcal{V}^+$ corresponding to the Schwarzschild Vacuum and an interior region $\mathcal{V}^-$ corresponding to the de Sitter condensate separated by a spacelike spherical hypersurface $\Sigma$ corresponding to the thin-shell. The spherically symmetric line elements $ds_\pm^2$ of the two spacetime regions of a gravastar can be written in the form

$$ds_\pm^2 = -f^\pm(r)\,dt^2 + \frac{1}{h^\pm(r)}dr^2 + r^2 d\Omega^2. \tag{3.6}$$

The metric functions $f(r)^\pm$ and $h(r)^\pm$ take the forms

$$f^+(r) = h^+(r) = 1 - \frac{2M}{r}, \qquad r > a, \tag{3.7}$$

$$f^-(r) = \alpha h^-(r) = \alpha\left(1 - \frac{2m(r)}{r}\right), \qquad r < a, \tag{3.8}$$

where $M$ is the total mass of the gravastar as measured by an observer in the exterior region $\mathcal{V}^+$, $a$ is the radius of the gravastar, which coincides with the radius of the hypersurface $\Sigma$, $\alpha$ is a constant free parameter whose effect on the model we clarify in what follows, and the mass function $m(r)$ is defined as

$$m(r) = \frac{4}{3}\pi\rho r^3, \tag{3.9}$$

where, from now on, $\rho$ is the constant energy density of the exotic fluid that populates the interior region $\mathcal{V}^-$, and $p$ is the isotropic pressure. Since the hypersurface located at $r = a$ is infinitesimally thin, we neglect its contribution to the gravastar line element. However, the shell's properties are necessary for the description of some of the gravastar parameters.

### 3.1.2 Junction Conditions

In this section, we follow [77, 132]. Let us now introduce two new definitions, the induced metric $h_{ab}$ and the extrinsic curvature $K_{ab}$ at $\Sigma$, given by

$$h_{ab} = e_a^\mu e_b^\nu g_{\mu\nu}, \qquad K_{ab} = e_a^\mu e_b^\nu \nabla_\mu n_\nu, \tag{3.10}$$

where $\nabla_\mu$ is the covariant derivative operator, that when applied to a covariant vector $U_\nu$ is defined by $\nabla_\mu U_\nu = \partial_\mu U_\nu - \Gamma^\lambda_{\mu\nu} U_\lambda$, $e^\mu_a$ are a set of vectors from the four-dimensional manifold $\mathcal{V}$, orthogonal to each other but not to $\Sigma$, while $n_\mu$ is the normal vector to the three-dimensional hypersurface at a fixed $r$, which is normalized to $n^\mu n_\mu = 1$ in the full four-dimensional spacetime. By definition, $e^\mu_a$ is orthogonal to $n_\mu$ satisfying $e^\mu_a n_\mu = 0$, being thus possible to explicitly write their components as

$$n_\mu = \frac{\delta^\mu_r}{\sqrt{h(r)}}, \qquad e^\mu_a = \begin{cases} \delta^\mu_a, & \mu = t, \theta, \phi \\ 0, & \mu = r \end{cases}, \tag{3.11}$$

where $\delta^\mu_\nu$ is the Kronecker delta. Note that, in the previous equations the Latin indices are intrinsic to the surface and thus range over the coordinates $t, \theta, \phi$, while the Greek indices are intrinsic to the manifold $\mathcal{V}$, ranging over the four coordinates. For the whole spacetime $\mathcal{V} = \mathcal{V}^+ \cup \mathcal{V}^-$ to be a solution of the EFE, it is necessary that the interior and exterior metrics defined in Eqs. (3.6)–(3.8) satisfy the so-called junction (or matching) conditions [133]:

$$[h_{ab}] = 0, \qquad \left[K^b_a\right] = -4\pi \left(2S^b_a - \delta^b_a S^c_c\right), \tag{3.12}$$

where the jump notation is introduced, $[X] = X^+|_{r=a} - X^-|_{r=a}$ and $S^b_a$ is the three-dimensional surface stress-energy tensor of the thin-shell at $\Sigma$. To obtain the respective junction conditions for the general case of the spherically symmetric metric it is first needed to determine the non-vanishing terms of $K^b_a = K_{ac} h^{cb}$ using Eq. (3.10). Let us focus on the time component first

$$K^t_t = K_{tt} h^{tt} = e^\mu_t e^\nu_t \left(\partial_\mu n_\nu - \Gamma^\lambda_{\mu\nu} n_\lambda\right) e^t_\mu e^t_\mu g^{tt}, \tag{3.13}$$

where, by the aforementioned definitions, the remaining indices must assume the respective coordinates $\nu = t, \mu = t, \lambda = r$ to obtain the non-vanishing component. The previous equation can then be rewritten as

$$K^t_t = e^t_t e^t_t \left(\partial_t n_t - \Gamma^r_{tt} n_r\right) e^t_t e^t_t g^{tt}, \tag{3.14}$$

which is reduced to

$$K^t_t = -\Gamma^r_{tt} n_r g^{tt} \tag{3.15}$$

when applying the definitions in Eq. (3.11). Following the same reasoning, the $\theta$ and $\phi$ components are given by

$$K^\theta_\theta = -\Gamma^r_{\theta\theta} n_r g^{\theta\theta}, \qquad K^\phi_\phi = -\Gamma^r_{\phi\phi} n_r g^{\phi\phi}. \tag{3.16}$$

The above general Christoffel symbols, given by Eq. (2.4), for the spherically symmetric metric are

$$\Gamma^r_{tt} = \frac{h f'}{2}, \qquad \Gamma^r_{\theta\theta} = -hr, \qquad \Gamma^r_{\phi\phi} = -hr \sin^2\theta, \tag{3.17}$$

where $'$ denotes the derivative with respect to the radial coordinate, and from Eq. (3.6) we obtain

$$g^{tt} = -\frac{1}{f}, \qquad g^{\theta\theta} = \frac{1}{r^2}, \qquad g^{\phi\phi} = \frac{1}{r^2 \sin^2\theta}. \tag{3.18}$$

Combining these with the definition of $n_\mu$, the non-vanishing components of $K^b_a$ for the spherically symmetric metric are

$$K^t_t = \frac{\sqrt{h}f'}{2f}, \qquad K^\theta_\theta = K^\phi_\phi = \frac{\sqrt{h}}{r}. \tag{3.19}$$

Let us now rearrange the second matching condition in Eq. (3.12) in order to obtain the non-vanishing components of the surface stress tensor

$$\left[K^t_t\right] = -4\pi\left(2S^t_t - \delta^t_t S^c_c\right), \tag{3.20}$$

$$\left[K^\theta_\theta\right] = \left[K^\phi_\phi\right] = -4\pi\left(2S^\theta_\theta - \delta^\theta_\theta S^c_c\right) = -4\pi\left(2S^\phi_\phi - \delta^\phi_\phi S^c_c\right). \tag{3.21}$$

From (3.21) comes that $2S^\theta_\theta - S^c_c = 2S^\phi_\phi - S^c_c \Rightarrow S^\theta_\theta = S^\phi_\phi$, where $S^c_c = S^t_t + S^\theta_\theta + S^\phi_\phi$ and so this equation can be rewritten as

$$\left[K^\theta_\theta\right] = -4\pi\left(2S^\theta_\theta - S^t_t - 2S^\theta_\theta\right) = 4\pi S^t_t. \tag{3.22}$$

Applying the same reasoning, Eq. (3.20) reduces to

$$\left[K^t_t\right] = -4\pi\left(S^t_t - 2S^\theta_\theta\right) = -\left[K^\theta_\theta\right] + 8\pi S^\theta_\theta. \tag{3.23}$$

From the last two equations together with Eq. (3.19) it is possible to obtain the non-vanishing components of the stress-energy tensor

$$S^t_t = \frac{\left[K^\theta_\theta\right]}{4\pi} = \frac{1}{4\pi}\left[\frac{\sqrt{h}}{r}\right], \qquad S^\theta_\theta = \frac{1}{8\pi}\left(\left[K^t_t\right] + \left[K^\theta_\theta\right]\right) = \frac{1}{8\pi}\left(\left[\frac{\sqrt{h}f'}{2f}\right] + \left[\frac{\sqrt{h}}{r}\right]\right). \tag{3.24}$$

By defining the surface energy density $\sigma$ and the surface tension $\Pi$ of the hypersurface as

$$S^b_a = \mathrm{diag}\left(-\sigma, \Pi, \Pi\right), \tag{3.25}$$

and substituting these in Eq. (3.24) as well as the jump notation and functions $h$ and $f$ defined in Eqs. (3.7),(3.8), finally leads to the first and second junction condition in Eq. (3.12), for the general spherically symmetric metric

$$[f] = 0, \tag{3.26}$$

$$\left[\sqrt{h}\right] = -4\pi a\sigma, \qquad \left[\frac{\sqrt{h}f'}{f}\right] = 8\pi\left(\sigma + 2\Pi\right), \tag{3.27}$$

respectively, where the second junction condition contributes with two restrictions, while the first condition only contributes with one, since the angular parts of the metric coincide for the exterior and interior region. Let us now introduce the following definitions for the volumetric mass $M_\rho$ and surface mass $M_\sigma$

$$M_\rho = \frac{4}{3}\pi a^3\rho, \qquad M_\sigma = 4\pi a^2\sigma. \tag{3.28}$$

The first junction condition in Eq. (3.26) demands $f$ as defined in Eqs. (3.7),(3.8) to be continuous at $r = a$, resulting in

$$1 - \frac{2M}{a} = \alpha \left(1 - \frac{8\pi\rho a^2}{3}\right) \tag{3.29}$$

where $\rho$ can be replaced by the definition of the volumetric mass in Eq. (3.28)

$$1 - \frac{2M}{a} = \alpha \left(1 - \frac{2M_\rho}{a}\right) \tag{3.30}$$

which sets the value of $\alpha$ for a given gravastar model

$$\alpha = \frac{1 - 2\bar{M}}{1 - 2\bar{M}_\rho}, \tag{3.31}$$

where $\bar{M}$ and $\bar{M}_\rho$ are the dimensionless quantities defined as $\bar{M} = M/a$ and $\bar{M}_\rho = M_\rho/a$. From this equation it is possible to conclude that the parameter $\alpha$ controls the total mass $M$ distribution of the gravastar. For instance, one finds that setting $\alpha = 1$ in Eq. (3.31) leads to $M = M_\rho$, which is equivalent to have all the gravastar's mass distributed in its volume. Following the same mathematical reasoning, the definition of the surface mass in Eq. (3.28) can be used to replace $\sigma$ in the first restriction of Eq. (3.27) leading to

$$-\frac{M_\sigma}{a} = \sqrt{1 - \frac{2M}{a}} - \sqrt{1 - \frac{2M_\rho}{a}}, \tag{3.32}$$

which when squared sets the value of the exterior mass $M$ as

$$\bar{M} = \bar{M}_\rho + \bar{M}_\sigma \sqrt{1 - 2\bar{M}_\rho} - \frac{\bar{M}_\sigma^2}{2}, \tag{3.33}$$

where, analogously, $\bar{M}_\sigma$ is defined as a dimensionless quantity $\bar{M}_\sigma = M_\sigma/a$. This equation complements the previous definition of the parameter $\alpha$, where is possible to observe that when $\alpha = 1$ we also have $M_\sigma = 0$. This is consistent with the previous analysis in which the total mass of the gravastar is distributed in its volume when $\alpha = 1$. As the value of the parameter $\alpha$ decreases, the total mass starts to be distributed both in its volume and surface until it reaches the limit value of $\alpha = 1 - 2\bar{M}$, that results in $M_\rho = 0$ from Eq. (3.31) indicating the total allocation of mass in the gravastar's hypersurface $\Sigma$. Recalling the discussion in the previous subsection, to satisfy the weak energy condition the model cannot feature negative energy densities. However, if $\alpha < 1 - 2\bar{M}$ we have $\rho < 0$, which motivates the exclusion of such configurations in this study [1].

Lastly, the second restriction of Eq. (3.27) can be rearranged to express the surface tension $\Pi$ as

$$\Pi = \frac{1}{2}\left(\frac{1}{8\pi}\left[\frac{\sqrt{h}f'}{f}\right] - \sigma\right), \tag{3.34}$$

where the jump notation and $\sigma$ can be replaced by their respective definitions

$$\Pi = \frac{1}{8\pi a}\left(\frac{\bar{M}}{\sqrt{1 - 2\bar{M}}} + \frac{2\bar{M}_\rho}{\sqrt{1 - 2\bar{M}_\rho}} - \bar{M}_\sigma\right), \tag{3.35}$$

as well as $\bar{M}_\sigma$ by Eq. (3.32)

[1] This type of solutions are allowed from a mathematical point of view but are excluded due to its limited physical relevance.

$$\Pi = \frac{1}{8\pi a}\left(\frac{1-\bar{M}}{\sqrt{1-2\bar{M}}} + \frac{1-4\bar{M}_\rho}{\sqrt{1-2\bar{M}_\rho}}\right). \tag{3.36}$$

Note that this expression for $\Pi$ is provided for completeness only, being irrelevant for the following analysis.

Once all the necessary parameters to describe a gravastar have been defined, we conclude that the thin-shell model is mainly controlled by two free parameters: the radius of the gravastar $a$, and the constant $\alpha$. It remains to be seen the impact of these in the metric components $g_{tt}$ and $g_{rr}$. Figure 3.1 shows $-g_{tt}$ (left column) and $g_{rr}$ (right column) as functions of the normalized radial coordinate, for different values of the gravastar radius (top panels) and for a fixed gravastar radius of $a = 3\ M$ but different values of $\alpha$ (bottom panels). In all plots the Schwarzschild BH solution is present, since this depicts the exterior region of the gravastar. When setting a fixed value of $\alpha$, a change in the gravastar radius alters the value in which the matching between the gravastar's exterior and interior regions occurs. Note that this matching occurs at the value of $a$ since it represents the boundary between the interior and exterior solutions, which is in agreement with what is expected. Besides, $-g_{tt}(0) = g_{rr}(0) = 1$, implying that the boundary conditions stay the same for distinct gravastar radius. On the other hand, this demeanor is not observed for the case where $a$ remains constant and $\alpha$ varies, in the $g_{tt}$ component. In this instance, a decrease in the value of $\alpha$ leads to a decrease of the boundary condition at $r = 0$, leaving the matching radius unaltered and inducing a discontinuity in $g_{rr}$ that becomes more evident for lower values of $\alpha$.

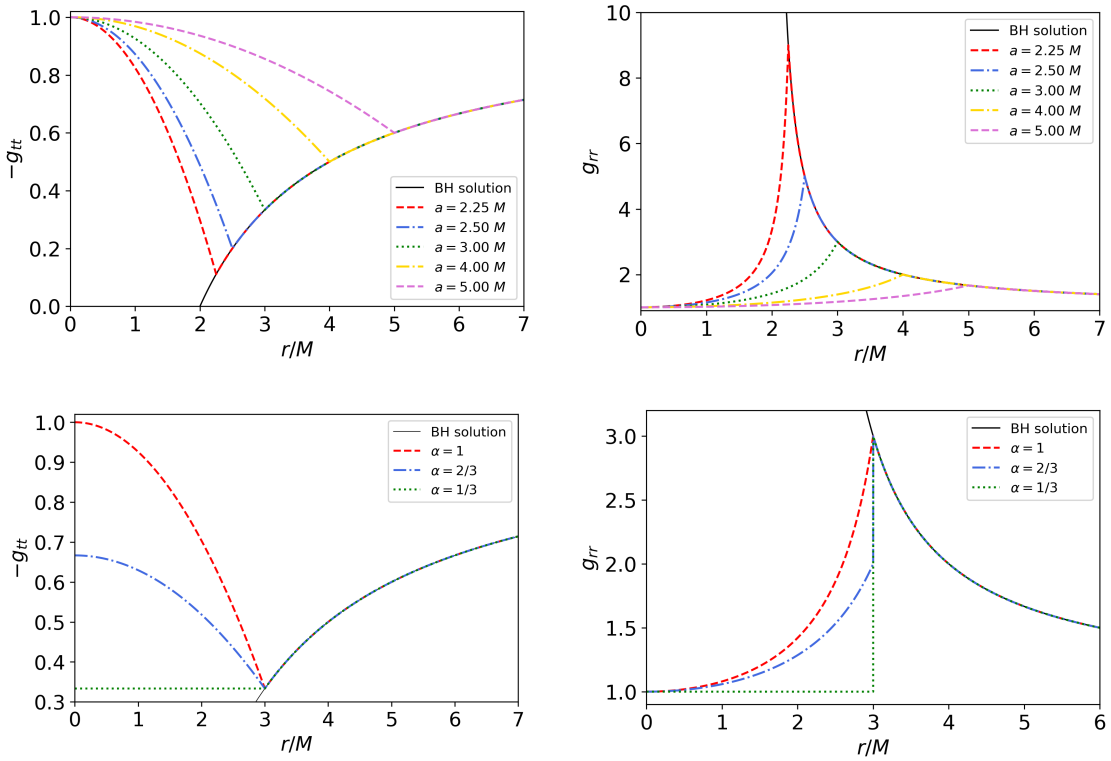


Figure 3.1: Plots of the metric components $g_{tt}$ (**left panels**) and $g_{rr}$ (**right panels**), shown in Eq.3.6 in function of the normalized radial coordinate, $r/M$. The black line represents the Schwarzschild solution. **Top Row**: Results for $\alpha = 1$ and different gravastar radius, $a$. This alters the radius where the matching occurs, maintaining the boundary conditions. **Bottom Row**: Results for $a = 3M$ and different values of $\alpha$. A decrease in value of $\alpha$ leads to a decrease in the initial boundary value of $g_{tt}$ and a discontinuity in $g_{rr}$, which becomes more discernible the lower the value of $\alpha$.

## 3.2 Geodesic and potential analysis

Let us recall the deduction made in section 2.2 of the photon effective potential in Eq. (2.44). The analysis of this potential allows one to study the qualitative features of geodesic motion, namely the presence and number of LRs in a certain configuration. Since the exterior region of the gravastar corresponds to a Schwarzschild spacetime the effective potential of photons is given by Eq. (2.55). On the other hand, substituting Eqs. (3.8) and(3.28) in Eq. (2.44), yields the photon effective potential for the interior of the gravastar

$$V_{phot}^{-} = \frac{1-\alpha}{a^2} + \frac{\alpha}{r^2} - \frac{2}{a}. \tag{3.37}$$

Figure 3.2 shows the plots of the effective potential for circular null geodesics $V_{phot}$ fixing $\alpha = 1$ while varying the gravastar radius $a$ (left column) and maintaining $a = 3M$ while varying the value of $\alpha$ (right column). On the left panel it is observed that the matching radius changes with the radius of the gravastar for the same aforementioned reasons in the analysis of the $g_{tt}$ and $g_{rr}$ components of the metric. Note that, for the right panel, the potential barrier decreases for smaller values of $\alpha$, corresponding to the addition of mass in the surface. Focusing on the left plot of figure 3.2, the analysis can be divided into three parts:

1. If $a > 3M$ there are no stationary points and so the photons cannot follow circular orbits around the gravastar meaning that no LRs are present in the spacetime.

2. If $a = 3M$ then $V'_{phot} = V''_{phot} = 0$ , featuring a saddle point that corresponds to a degenerate pair of LRs at $r_{LR} = 3M$.

3. If $a < 3M$ the photon potential features two points in which $V'_{phot} = 0$, a maximum at $r_{LR}^{+} = 3M$ corresponding to an unstable LR, and a minimum at $r_{LR}^{-} = a$ corresponding to a stable LR.

Summarizing, the presence and number of LRs depends on the considered gravastar radius, where the configurations that do not feature any LR are the ones with $a > 3M$. On the other hand, for a constant value of $a$, the parameter $\alpha$ does not affect the amount of LRs present, impacting only the potential's shape quantitatively.

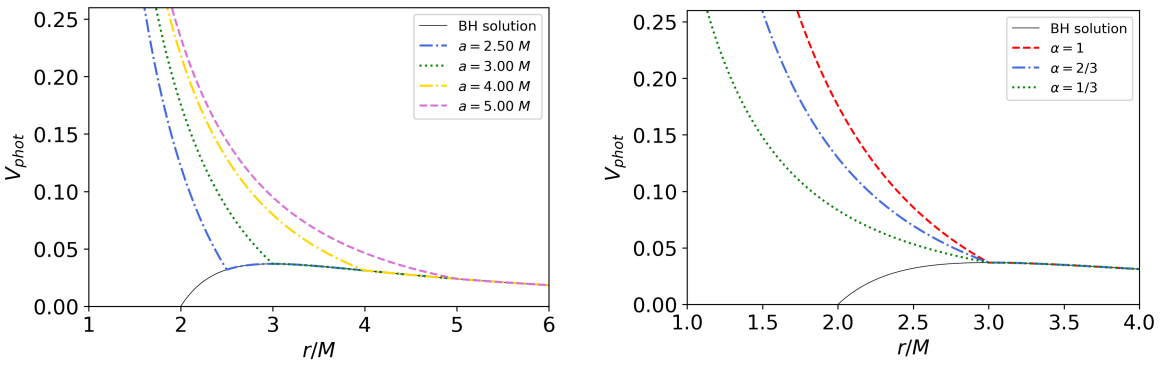


Figure 3.2: Effective photon-potential in order of the normalized radial coordinate , $r/M$ for the gravastar and the Schwarzschild solution (black line). **Left Panel**: Results for $\alpha = 1$ and different gravastar radius, $a$. **Right Panel**: Results for $a = 3M$ and different values of $\alpha$. The gravastar radius affects the presence and number of LRs, while the parameter $\alpha$ has no impact.

# Chapter 4

# Methodology

This chapter aim is to understand how the theory is implemented and which methods were used to obtain the results present in the next chapter. The first section exposes the code used to process the theoretical data and generate the astrometrical observables as well as the needed implementations: analytical quantities and the modelling of the source. This is followed by a brief description of the ray-tracing technique applied, which can be divided in two sections dedicated to the backwards integration of geodesics and the further integration of the radiative function equation once the photon reaches the emitter. The last section focuses on describing the outputs of the code as well as the gravastar, observation and screen parameters essential to simulate a spherically emitting source orbiting a central compact object.

## 4.1 Implementation

To generate the observational signatures of a hot-spot orbiting a central gravastar it is necessary to trace the geodesics in the vicinity of the compact object. This is accomplished via ray-tracing of null geodesics that are emitted from an observer's screen and are integrated backwards in time until it reaches the emitting source. To accomplish this goal we use the ray-tracing code GYOTO (**G**eneral relativit**Y** **O**rbi**T** of **O**bservatoire de Paris), developed by Vincent et al. (2011) [62, 86–88, 134–138]. GYOTO has the ability to generate images and spectra for various astrophysical bodies, like an orbiting star or accretion disks, around a compact object. The code is also capable to integrate null and timelike geodesics for both analytical or numerical metrics. Because of this, the central object can either be a Kerr BH [137] or even an ECO [86–88, 139], in our case, Gravastars. Grould et al. (2016) [134], tested the validity of the code and concluded that GYOTO exhibits a sufficient level of accuracy to model star trajectories and fit the GRAVITY data. Given these traits, GYOTO is suitable to achieve the goals of this work, since it allows the implementation of the gravastar metric and outputs astrometrical observables that provide a way of comparison with instrument observations. To be able to run the code it is necessary to input the following analytical descriptions:

1. The metric components of the background spacetime which are given by the Eqs. (3.7), (3.8) and

can be summed in:

$$g^{+}_{\mu\nu} = \begin{pmatrix} -1+\dfrac{2M}{r} & 0 & 0 & 0 \\ 0 & \left(1-\dfrac{2M}{r}\right)^{-1} & 0 & 0 \\ 0 & 0 & r^2 & 0 \\ 0 & 0 & 0 & r^2\sin^2\theta \end{pmatrix} \tag{4.1}$$

$$g^{-}_{\mu\nu} = \begin{pmatrix} -\alpha\left[1-\dfrac{r^2}{a^2}\left(1-\dfrac{1-2\bar{M}}{\alpha}\right)\right] & 0 & 0 & 0 \\ 0 & \left[1-\dfrac{r^2}{a^2}\left(1-\dfrac{1-2\bar{M}}{\alpha}\right)\right]^{-1} & 0 & 0 \\ 0 & 0 & r^2 & 0 \\ 0 & 0 & 0 & r^2\sin^2\theta \end{pmatrix} \tag{4.2}$$

where $\bar{M}$ represents the dimensionless quantity $M/a$. In equation (4.2), $g_{tt}$ and $g_{rr}$ are obtained considering Eqs. (3.8), (3.28) and (3.31), in order to express these metric components with an exclusive dependence on the free parameters $a$ and $\alpha$.

2. The corresponding Christoffel symbols, given by the equation (2.4), for the exterior region:

$$\Gamma^1_{00} = \left(1-\frac{2M}{r}\right)\times\frac{1}{r^2}$$

$$\Gamma^0_{01} = \Gamma^0_{10} = -\Gamma^1_{11} = \left(1-\frac{2M}{r}\right)^{-1}\times\frac{1}{r^2}$$

$$\Gamma^1_{22} = -\left(1-\frac{2M}{r}\right)\times r, \quad \Gamma^1_{33} = \Gamma^1_{22}\sin^2\theta$$

For the interior region:

$$\Gamma^1_{00} = \frac{\left[r\left(2M-a+a\alpha\right)\right]\times\left[r^2\left(2M-a+a\alpha\right)-a^3\alpha\right]}{a^6\alpha}$$

$$\Gamma^0_{01} = \Gamma^0_{10} = -\Gamma^1_{11} = \frac{r\left(2M-a+a\alpha\right)}{2r^2+r^2\left(a\alpha-a\right)-a^3\alpha}$$

$$\Gamma^1_{22} = -\frac{r\left(1+r^2\left(2M-a+a\alpha\right)\right)}{a^3\alpha}, \quad \Gamma^1_{33} = \Gamma^1_{22}\sin^2\theta$$

And the Christoffel symbols common to both the interior and exterior of the gravastar:

$$\Gamma^2_{12} = \Gamma^2_{21} = \Gamma^3_{13} = \Gamma^3_{31} = \frac{1}{r}$$

$$\Gamma^2_{33} = -\sin\theta\,\cos\theta$$

$$\Gamma^3_{32} = \Gamma^3_{23} = \frac{\cos\theta}{\sin\theta}$$

the remaining Christoffel symbols are zero.

3. The equatorial orbital velocities $\Omega_c$ as a function of the radius, given by equation (2.52):

$$\Omega^+_{GS} = \sqrt{\frac{M}{r^3}} \tag{4.3}$$

$$\Omega^-_{GS} = \sqrt{\frac{a-2M-a\alpha}{a^3}} \tag{4.4}$$

where $\Omega^+_{GS}$ corresponds to the orbital velocity of timelike particles in the exterior of the gravastar while $\Omega^-_{GS}$ corresponds to the interior. Note that, for $r < a$, the angular velocity is independent of the radial coordinate, being constant inside the gravastar, and that this velocity is never used in the simulation since the hot spot only orbits in the exterior region. Even though the orbital velocity is the quantity needed to run the code, the orbital period $T$, is in fact the quantity used in the observational data. It is then possible to compute the orbital period via the orbital velocity as: $T = 2\pi/\Omega$.

### 4.1.1 Modelling the hot spot

The emitting source is modelled in GYOTO as an isotropically emitting sphere orbiting the central massive object, where only the timelike geodesic of the sphere's center is computed. The astrophysical object is then defined as the points whose Cartesian-like coordinates ($x \equiv r\sin\theta\cos\phi, y \equiv r\sin\theta\sin\phi, z \equiv r\cos\theta$) have a distance to the center smaller than the sphere's radius $R$, i.e. the points that satisfy:

$$(x-x_c)^2 + (y-y_c)^2 + (z-z_c)^2 \leq R^2 \tag{4.5}$$

where $(x_c, y_c, z_c)$ are the sphere center's coordinates. Note that, due to the simplicity of the model, no internal physics nor tidal effects are taken into account. [62]

This model mimics an optically thin hot spot orbiting in the equatorial plane of the central gravastar, at a constant orbital radius $r_o$. To perform the simulation we consider 180 positions of the source around the central object in the equatorial plane $\theta = \pi/2$ with $\phi = 0$ and the radius of the hot spot is set to $R \equiv r_{HS} = M/2$, in agreement with the upper limit of $0.3R_S$, where $R_S$ is the Schwarzschild radius, derived by [54].

## 4.2 Ray-tracing

Once the necessary inputs to run the code are implemented, as well as the model of the hot spot, one can ray-trace the orbits of the emitting source around the central compact object. This process consists mainly in two steps: the backward integration of null geodesics from an observer's screen towards the emitting astrophysical object; the integration of the radiative transfer equation along the computed geodesic, once the photon reaches the radiation source, in order to determine the value of the emitted specific intensity that will reach the observer.

### 4.2.1 Integration of Geodesics

To perform the backwards ray-tracing of a single null geodesic in GYOTO, it is necessary to determine the tangent vector to the photon's trajectory at the observer's position. To acquire this information, both the position of the observer and the observation angle must be inputted in the code as the initial conditions. In our case, the observer is considered to be at a radial coordinate of $r = 1000M$, and three different observation angles are considered, which are detailed later in this chapter. Once these quantities are set, the equations of motion present in Eq. (2.29) are solved using a Runge-Kutta algorithm of fourth order (RK4). This integration is performed backwards in time with the aim to save computing time, since most of the photons would not reach the observer with forward ray-tracing. Following [62], the integration goes on until one of the following stop conditions is fulfilled:

- the photon reaches the emitting object;
- the photon escapes too far from the target object;
- the photon approaches too closely to the event horizon. In our case, since the gravastar is an horizonless compact object, this condition is never fulfilled.

To ensure a proper integration, the developers of the code impose the conservation of the constants of motion by continuously checking them and modifying the solution of the integration when needed (see [62] for further details).

### 4.2.2 Radiative Transfer

Following the backward integration of the geodesics, when the photon reaches the emitting source, a part of its trajectory lies inside the emitter, requiring the integration of the radiative transfer equation along the rest of the geodesic. The radiative transfer equation mainly translates the loss of energy to absorption and gain of energy by emission as a beam of radiation travels. Defining the emission coefficient as $j_\nu$ and the absorption coefficient as $\alpha_\nu$, the intensity added by spontaneous emission and the loss of intensity by absorption, in a beam as it travels a distance $ds$ is, respectively, given by [140]:

$$dI_\nu = -\alpha_\nu I_\nu ds \qquad \text{and} \qquad dI_\nu = j_\nu ds, \tag{4.6}$$

where $dI_\nu$ corresponds to the specific intensity's increment. It is then possible to combine both equations to obtain the effects of emission and absorption in the specific intensity along a ray:

$$\frac{dI_\nu}{ds} = -\alpha_\nu I_\nu + j_\nu, \tag{4.7}$$

Let us now introduce a new variable $\tau_\nu$ called the optical depth and defined by [140]:

$$d\tau_\nu = \alpha_\nu ds \qquad \text{or} \qquad \tau_\nu(s) = \int_{s_0}^{s} \alpha_\nu \left(s'\right) ds' \tag{4.8}$$

where $s_0$ is arbitrary, setting the point where the optical depth is zero. By the previous definition one can extrapolate that the optical depth describes how much absorption occurs when light travels through a medium, being measured along the path of a traveling ray. With this being said, if $\tau_\nu > 1$ there is absorption present and the medium is said to be optically thick or opaque. However, if $\tau_\nu < 1$ there is no absorption of light ($\alpha_\nu = 0$) and the medium is said to be optically thin or transparent. Since our emitting source is modelled to be optically thin, equation (4.7) reduces to:

$$\frac{dI_{\nu_{em}}}{ds_{em}} = j_{\nu_{em}} \tag{4.9}$$

where all quantities are computed in the emitter's frame. Following [140], equation (4.9) can be immediately integrated between some value $s_0$ where the specific intensity is vanishing and some position $s$:

$$I_\nu(s) = I_\nu(s_0) \int_{s_0}^{s} j_\nu\left(s'\right) ds' \tag{4.10}$$

The previous equation finally allows the computation of the integrated specific intensity. To be able to perform this computation it is necessary to provide the emission coefficient $j_\nu$ at each integration step in the frame of the observer comoving with the emitting matter. Note that the impact of scattering is not taken into account by the code [62].

## 4.3 Astrometric Observables

Upon performing the ray-tracing, the software outputs a two dimensional image with specific intensities $I_{\nu lm}$ [1] for each time instant $t_k \in [0, T[$ of the lensed hot spot, where $T$ is the orbital period of the hot spot. Subsequently, these intensities can be converted to data cubes $I_{klm} = \Delta\nu I_{\nu lm}$, where $\Delta\nu$ represents the spectral width, to produce three observable quantities:

1. Time integrated flux $\langle I \rangle_{lm}$ that result from performing a full integration of the hot spot orbit by summing all the illuminated pixels for an orbital period. The two dimensional image is now a sum of all specific intensities for a full orbit instead for each time instant. This observable is explicitly given by

$$\langle I \rangle_{lm} = \sum_k I_{klm} \tag{4.11}$$

2. Temporal Flux $F_k$ that correspond to the sum of all specific intensities of every pixel at a given time instant. It is explicitly given by

$$F_k = \sum_{l,m} \Delta\Omega I_{klm} \tag{4.12}$$

where $\Delta\Omega$ represents the solid angle of a single pixel.

3. Temporal Centroid $\vec{c}_k$ that relates to a weighted average of the pixels that are illuminated at a given instant. If two pixels are symmetrically illuminated at a given instant, then the centroid is located at the centre of the image. On the other hand, if only one pixel is lightened for a specific time instant, then the centroid is located at the same position of that same pixel. The observable can be explicitly given by

$$\vec{c}_k = \sum_{l,m} \Delta\Omega I_{klm} \vec{r}_{lm} \tag{4.13}$$

where $\vec{r}_{lm}$ denotes the displacement of a pixel $\{l,m\}$ with respect to the centre of the observed image.

[1] each pixel $\{l,m\}$ represents a specific intensity

From the temporal fluxes, one can define the more commonly known temporal magnitude $m_k$ as

$$m_k = -2.5 \log \left( \frac{F_k}{\min F_k} \right) \tag{4.14}$$

The main motivation for carrying out this astrometric analysis is linked to the ability of the instruments (e.g. EHT collaboration, GRAVITY, etc) to measure these quantities and thus provide a possible means to compare our results with experiments.

In the next chapter the astrometric observables defined above are analyzed for five different gravastar radius, as depicted in Table 4.1, two values of $\alpha$, namely $\alpha = \{1, \alpha_{min}\}$, with $\alpha_{min} = 1 - 2\bar{M}$, for three different observation inclination angles $i = \{20^\circ, 50^\circ, 80^\circ\}$, and for three different orbital radius $r_o = \{8M, 10M, 12M\}$. Regarding the observer's screen, a pixel corresponds to a direction on the sky, being defined by a field of view of $200\mu as$ with a pixel size of $1\mu as$. The number of pixels that covers this field of view, also known as resolution, $N_{pixels} \equiv R$, is different depending on the configuration being considered. The resolution for GS1-GS3 is $R = 1000$ while for GS35-GS5 the resolution is $R = 500$. This choice is motivated by the presence of light rings in the more compact solutions which demand a higher resolution for a better detection of these features. Since the less compact solutions lack this feature, to save computation time, we consider a smaller resolution. Regarding the Schwarzschild BH, its simulation is performed considering an orbital radius of $r_o = 8M$, the same previously mentioned inclination angles and with a resolution of $R = 1000$.

Table 4.1: The gravastar radius, $a$, considered in each configuration used in this dissertation. The values of $\alpha$ and orbital radius, $r_o$ can change in the same configuration, meaning that $a$ is the only parameter that doesn't change in a model.

| Configuration | $a/M$ |
|---|---|
| GS1 | 2.25 |
| GS2 | 2.50 |
| GS3 | 3.00 |
| GS35 | 3.50 |
| GS4 | 4.00 |
| GS5 | 5.00 |

# Chapter 5

# Results

In the first section, we present the time integrated flux results following the methodology described in the previous chapter. In this analysis we study the effects of three different parameters, namely: the observation inclination, the hot-spot orbital radius and the value of $\alpha$, each one of them corresponding to a sub-section, respectively. In the second section the temporal magnitude and centroid results are simultaneously discussed.

## 5.1 Time integrated images

### 5.1.1 Impact of the observation inclination

In this sub-section, the goal is to analyse the differences between the SBH solution and the various gravastar models, for different observation angles. For this purpose, the sub-section is separated into two groups: the more compact solutions, including the GS1, GS2 and GS3 and the less compact solutions, including GS3, GS4 and GS5. Since the radius of the GS3 model coincides with the radius of the SBH photon sphere ($r_{PS} = a = 3M$), this configuration is used as a transition between models that have a LR and those that do not.

#### 5.1.1.1 More compact solutions

Figure 5.1 shows the integrated fluxes for a SBH and the gravastar configurations with $a \leq 3M$ with a constant orbital radius of $r_o = 8M$, $\alpha = 1$ and observation inclination angles of $i = \{20^\circ;\ 50^\circ;\ 80^\circ\}$, from left to right. Revisiting subsection 1.1.2, it is known that the SBH possesses a primary image, a secondary image and a LR contribution. However, for the gravastar models, an additional secondary image is present for all configurations and observation angles. An additional central feature is scarcely visible in GS1 and GS2 but more noticeable in GS3, for $i = 80^\circ$. This signature corresponds to the previously discussed plunge-through image (see subsection 1.1.4) which usually appears in a high observation inclination. Apart from these qualitative differences, there are also subtler quantitative differences present when the gravastar radius changes, such as: the distance between the inner secondary image and the centre, and the discrete number of LRs present. In the SBH case, the presence of an event horizon hinders the light rays below the critical curve from reaching an observer, while for a gravastar, the lack of it allows for distinct signatures for smaller impact parameters. To expose these different behaviours, figure 5.2 exhibits the geodesics of the SBH solution as well as the three gravastar models in study. The compact objects are located at the centre of the image where $z = y = 0$. The hot-spot equatorial plane for

an inclination of $i = 0.01^\circ$ [1] is represented by the solid black line. The observer is located on the left side of the images, at $y = -1000M$. In this figure, the colored lines correspond to the trajectories of photons that: produce the direct image (blue); produce the secondary image (yellow); produce the LR photons (red); cross the EH (green), corresponding to the shadow in the case of the SBH. This geodesic categorization was established according to the definition provided in subsection 1.1.2. The black dashed line is traced at the radius of the photon sphere, $r_{PS} = 3M$; the black dotted line assumes the role of event horizon at $r = 2M$ for the BH case, and the role of gravastar radius for $r = \{2.25M, 2.50M, 3.00M\}$ for the corresponding configurations GS1, GS2 and GS3. Note that, since the metric is spherically symmetric, only the geodesics for positive values of $z$ are represented.

Note how below the critical impact parameter, no geodesics reach the observer for the SBH case, visible in figure 5.2, for a low observation inclination, where trajectories with $r < 3M$ (photon sphere) eventually fall into the horizon. This can be observed in the top row of figure 5.1 for $i = 20^\circ$ since no emission is detected inside the LR contribution. In contrast, for the gravastar configurations, there are light trajectories with a radial coordinate with an impact parameter below the critical value that reach the observer (Fig. 5.2), allowing for the detection of extra features in the integrated images. This corroborates the existence of an inner secondary image for all gravastar models. However, among these configurations, the distance of this signature to the centre increases with the gravastar radius. This discrepancy can be explained by looking at the range of impact parameters that correspond to trajectories that produce a secondary image (Fig. 5.2). This value increases with the increase of the value of $a$, meaning that this feature is expected to appear further away from the centre of the compact object for a larger gravastar radius. Note also that some null geodesics intersect at the equatorial plane of the hot-spot. These correspond to specific values of $r_o$ in which the luminous source is lensed into different tracks. Applying to the present gravastar configurations, when the hot-spot passes these points more than one image appears in the observer screen simultaneously, corresponding, in this case, to an inner secondary image and an outer secondary image.

Focusing on figure 5.2, near the critical impact parameter, it is possible to observe that there are some photons that cross the hot-spot's equatorial plane more than two times, for the GS1, GS2 and GS3, being classified as LR photons. Recalling the previous potential analysis (section 3.2), it is possible to observe LR tracks between the gravastar radius and the photon sphere for GS1 and GS2 since they possess a stable and an unstable LR. This is depicted in figure 5.2 where the photon trajectories are contained in this range of radial coordinates. Note also that, although there is a continuous interval of impact parameters of geodesics defined as LRs, the only trajectories that reach the observer screen are the ones that trace back to the luminous source. This only happens for discrete impact parameter values rather than the whole possible range. The same logic applies for the other observed images. Therefore, it is possible to detect more than one LR track in figure 5.1, for $a < 3M$, while only one LR is detectable in the GS3 model, once the gravastar radius coincides with the photon sphere and so, below this radius the gravastar geometry no longer corresponds to the SBH geometry. Above the LR tracks, all configurations behave in the same way, having the same features present: an outer secondary image and a direct image (visible both in the integrated images and geodesics).

Looking one last time to figure 5.1, it is possible to observe an increase in the plunge-through image for larger values of $a$. Once the gravastar radius increases, more photon trajectories cross directly the middle of the gravastar and thus turning the observation of this feature more discernible (see figure 5.2). This image is also only present for higher inclinations because it corresponds to emission that

[1] the software does not support the exact value of $i = 0^\circ$

comes directly from the hot-spot when it is behind the compact object. Further comments on the impact of inclination on these models are discussed in the following sub-section, together with the remaining configurations.

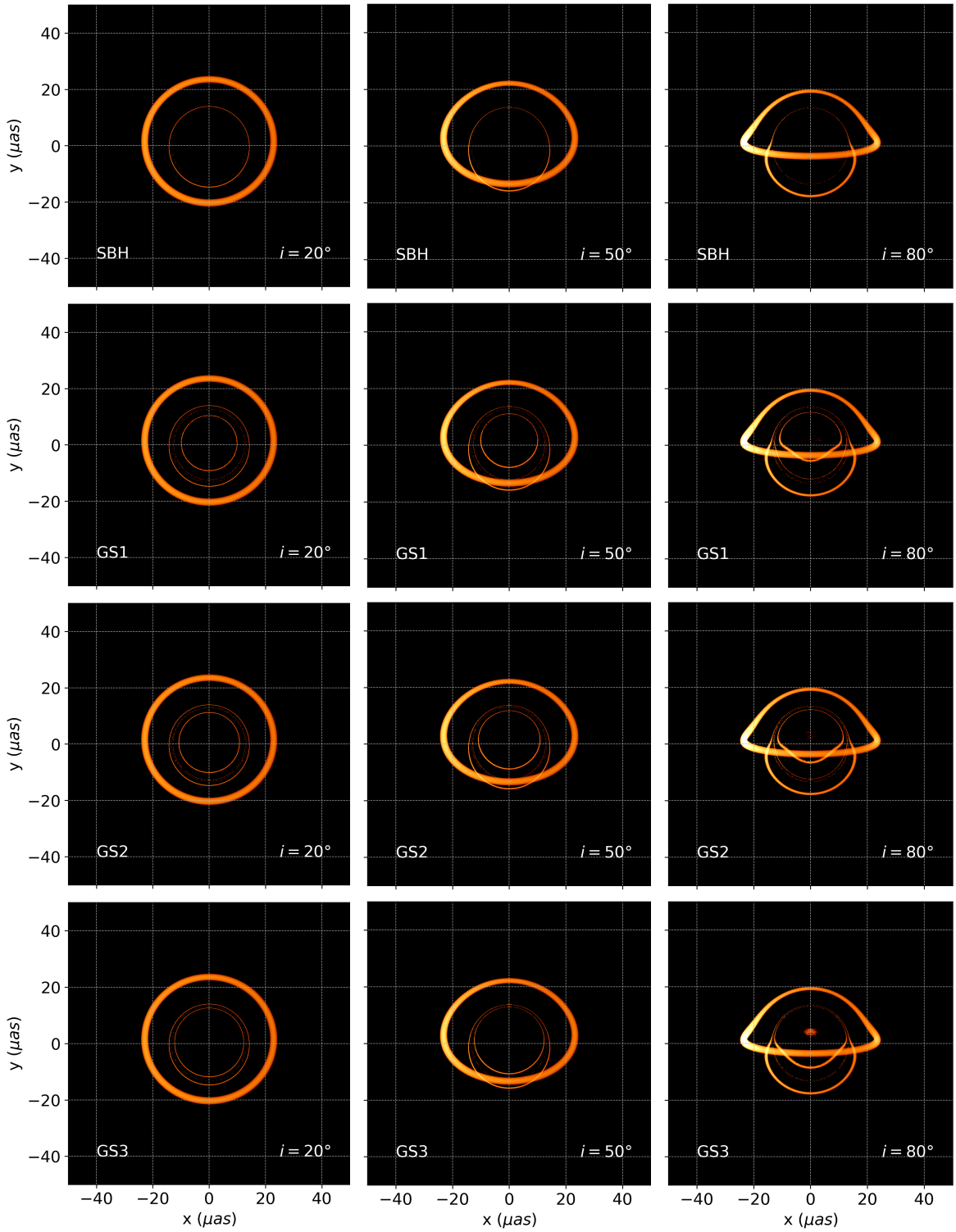


Figure 5.1: Time integrated images of a full orbit, assuming an isotropically emitting source, with a radius of $r_{HS} = M/2$, for the SBH and gravastar configurations with a radius, from top to bottom, of $a = \{2.25M, 2.5M, 3M\}$ and an inclination of $i = \{20°, 50°, 80°\}$, from left to right. For all the simulations it was set $\alpha = 1$ and an orbital radius of $r_o = 8M$.

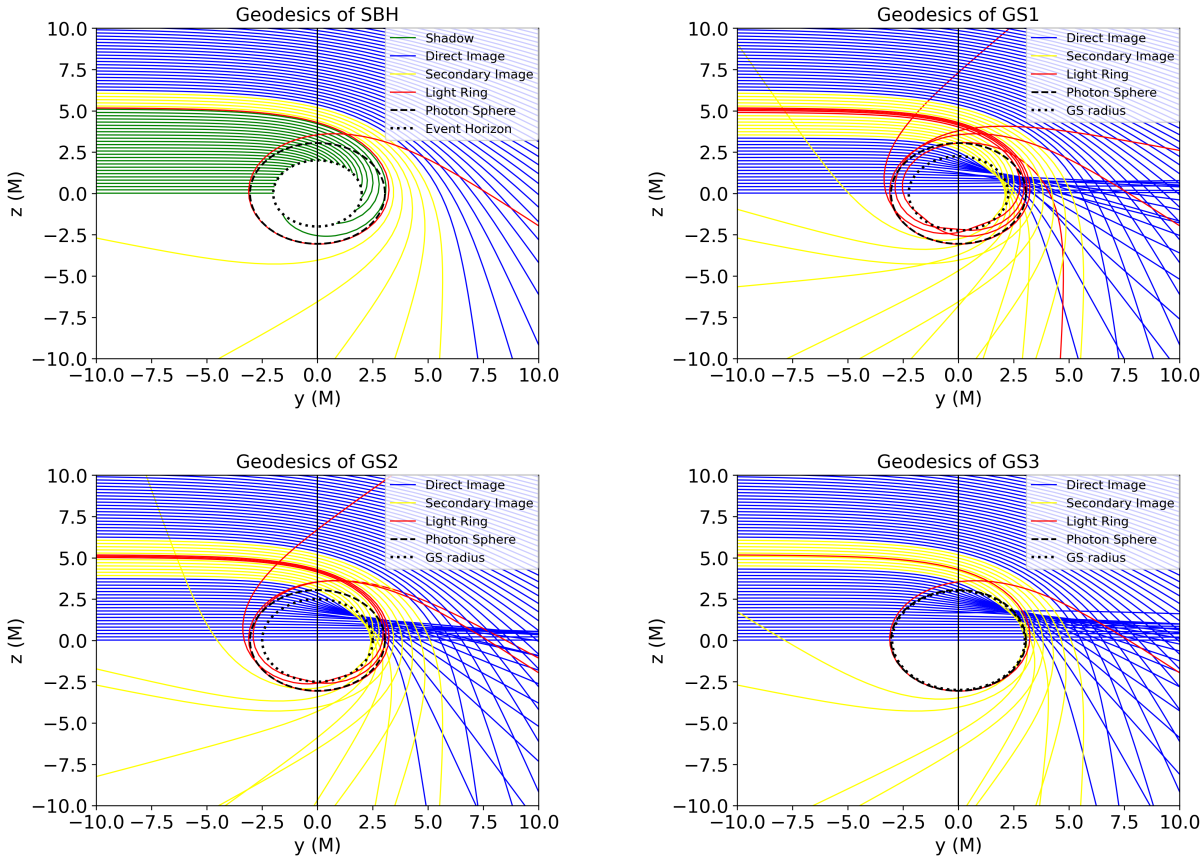


Figure 5.2: Photon geodesics for the SBH solution and the configurations GS1, GS2 and GS3 with $i = 0.01^\circ$ and $\alpha = 1$. The observer is located towards the left side of the image at $y = -1000M$ while the compact object is located at the centre. The colored lines correspond to the trajectories of photons that: produce the primary image (blue); produce the secondary image (yellow); produce the LRs (red); cross the EH (green). The black lines correspond to: the photon sphere (dashed); the event horizon for the SBH case (dotted); the gravastar radius for GS1-GS3 configurations (dotted); position of the equatorial plane for $i = 0.01^\circ$ (solid).

Although it is possible to distinguish these three configurations, they are qualitatively similar and thus only GS3 is used in the following analysis, since it represents a critical configuration between the most compact models and the least ones.

#### 5.1.1.2 Less compact solutions

Let us now focus on the analysis of the configurations with a smaller compacticity. Figure 5.3 shows the integrated fluxes for a Schwazrschild BH and the gravastar configurations GS3, GS4 and GS5 with an orbital radius of $r_o = 8M$, $\alpha = 1$ and observation inclination angles of $\theta = \{20^\circ;\ 50^\circ;\ 80^\circ\}$, from left to right. Comparing the GS3 model with the new models in consideration, some changes are present for an inclination of $80^\circ$: 1) the absence of a light ring like it was predicted in the analysis of the effective potential in section 3.2; 2) the merging between the two secondary images, where they are practically coincident in the GS5 configuration; 3) the increase in size of the plunge through image that eventually forms a closed track with an increase in the gravastar radius. The second appointed difference can be better understood by looking at figure 5.4 where the transition between the GS3 and GS4 model is shown by the addition of the GS35 model. In this configuration it is possible to observe the merge between the two secondary images and the transition to a situation where they start to form a closed curve, as

well as the increase in size of the central image and the absence of the light ring. The increase in the gravastar radius indicates that the compacticity of the star is lower and thus the effects of light deflection close to the surface of the star are weaker, resulting into a closed secondary track. This decrease in the compacticity is also what leads to the near overlap of the secondary images visible for GS5 configuration. The same reasoning justifies the expansion of the plunge-through image, as mentioned in the previous subsection. In figure 5.3, for the GS5 model the inner closed track corresponds to the light that travels directly from the hot spot as it passes behind the gravastar, being classified as a plunge through image.

Shifting our attention now to the impact of the inclination in figures 5.1 and 5.3, it is possible to distinguish three different cases:

1. For the ultra-compact configurations (GS1-GS3), the amount of observational signatures is the same when considering an inclination below $80^\circ$ (two separated secondary tracks). However, the increase in the observation angle makes it possible to observe an extra feature in all of these models (GS1-GS3), the plunge through image;

2. For the GS4, the light deflection is smaller than in GS3 since the object is less compact. Because of this it is only possible to observe one closed secondary track, present for all observation angles considered. Similarly to the other cases, an increase in the inclination results in the appearance of the plunge through image;

3. Finally, for the GS5 model, the inclination plays a huge role in the amount of the observed features. Since the light deflection is smaller for this model, only the direct image is present for lower inclinations . Although, for $i = 80^\circ$ the plunge through image is present, forming a closed track and the closed secondary track is also detectable, where the secondary images almost coincide.

To better understand the impact of inclination in the GS4 and GS5 configurations let us focus on figure 5.5. As previously indicated, the compact objects are located at the centre of the image where $z = y = 0$, the observer is located on the left side of the images, at $y = -1000M$ and since the secondary images appear below $y = 0$, only the geodesics for negative values of $z$ are represented. This figure has some slight differences in comparison with figure 5.2 that emphasize how the observation inclination angle and the orbital radius affect the results. In figure 5.5 the solid lines represent the hot-spot equatorial plane while different colors correspond to different angles: green for $20^\circ$, red for $50^\circ$ and black for $80^\circ$. Note that unlike the previous geodesic plots, the hot spot orbit is now projected in the $yOz$ plane. This is due to the fact that the hot spot is performing orbits around the compact object with a specific orbital radius. The length of these solid lines takes into account the orbital radius considered in these simulations, $r_o = 8M$ as well as the fact that the hot-spot has a radius of $r_{HS} = M/2$.

For instance, in the GS5 model, the geodesics cross the hot spot orbit twice only for an inclination of $80^\circ$. Therefore, a secondary image is not expected to be observed for $i = \{20^\circ, 50^\circ\}$, while it must be present for $i = 80^\circ$ which is consistent with the integrated flux results. For the GS4 model there is at least one trajectory of light that crosses the equatorial plane after emission and before reaching the observer. This means that these are secondary tracks and thus a secondary image must be present for all inclinations, consistently with what is observed in the analysis of the integrated flux (5.3). Focusing on an inclination of $80^\circ$, there are some secondary tracks where their trajectories pass at a minimum radial distance larger or smaller than the gravastar radius. When these intersect and cross the equatorial plane, the hot spot image is lensed in two and the observer detects two distinct secondary images simultaneously. This explains why it is possible to detect two secondary images in figure 5.3 for GS4 and GS5 instead of

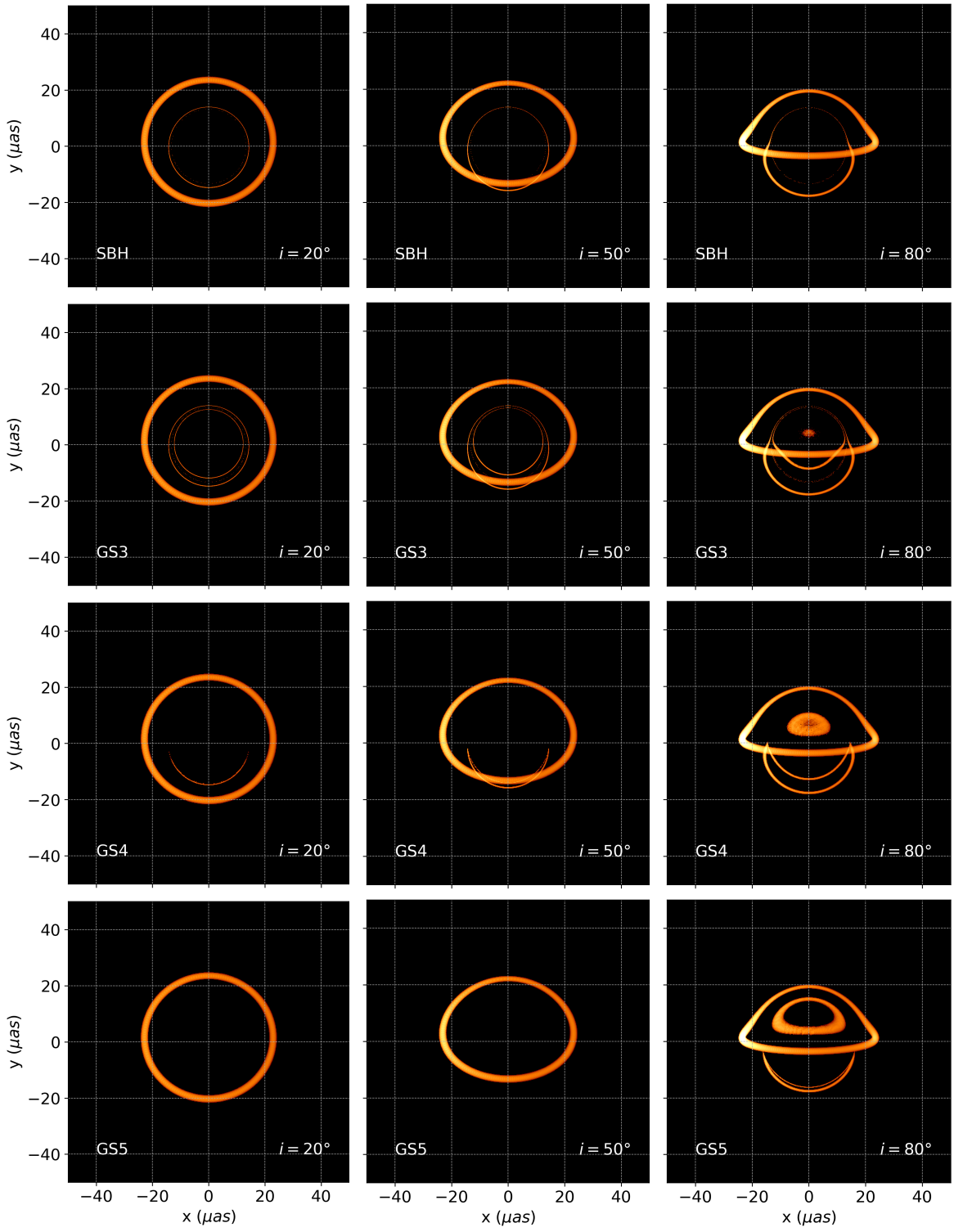


Figure 5.3: Time integrated images of a full orbit, assuming an isotropically emitting source, with a radius of $r_{HS} = M/2$, for the SBH and gravastar configurations with a radius, from top to bottom, of $a = \{3M, 4M, 5M\}$ and an inclination of $i = \{20°, 50°, 80°\}$, from left to right. For all the simulations it was set $\alpha = 1$ and an orbital radius of $r_o = 8M$.

just one like in the SBH case. It is also possible to predict that if a smaller orbital radius was taken into account, the green line would be smaller and thus the geodesics would not cross the hot-spot equatorial plane twice. This implies that for $r_o < 8M$ the integrated flux of the GS4 configuration would only show

direct image for $i = 20°$. This indicates not only a dependency on the inclination but also on the hot spot distance, which motivates the study of the impact of the orbital radius.

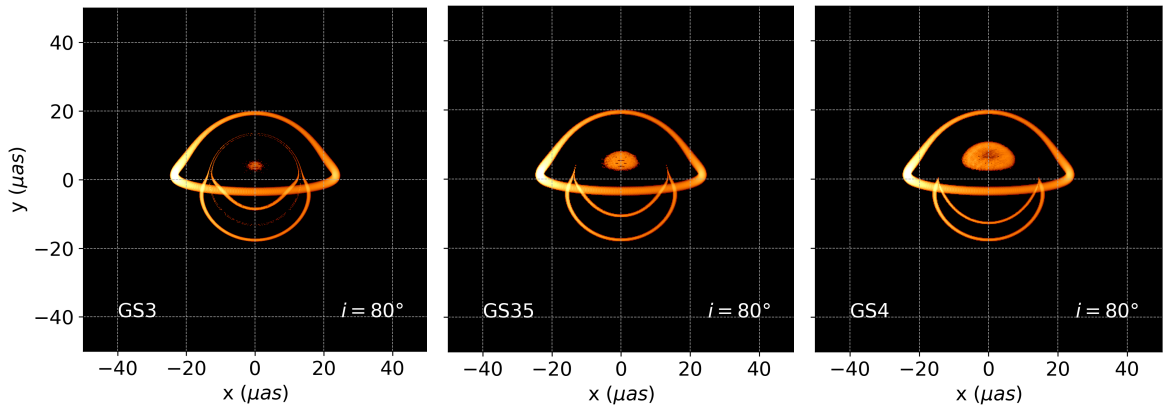


Figure 5.4: Time integrated images of a full orbit, assuming an isotropically emitting source, with a radius of $r_{HS} = M/2$, featuring the transition between GS3 and GS4. The gravastar configurations depicted have a radius of $a = \{3M, 3.5M, 4M\}$ and an inclination of $i = 80°$. For all the simulations it was set $\alpha = 1$ and an orbital radius of $r_o = 8M$.

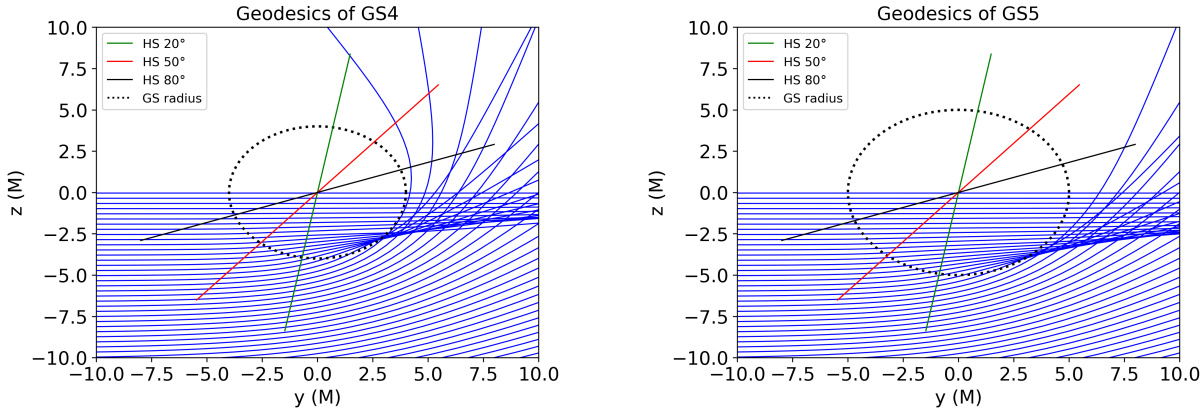


Figure 5.5: Photon geodesics for GS4 and GS5 with $\alpha = 1$. The observer is located towards the left side of the image at $y = -1000M$ while the compact object is located at the centre. The solid lines correspond to the hot-spot equatorial plane for 20° (green), 50° (red) and 80° (black). The length of each solid line accounts for the orbital radius $r_o = 8M$ plus the hot-spot radius $r_{HS} = M/2$.

### 5.1.2 Impact of the orbital radius

Figure 5.6 displays the integrated fluxes for the gravastar configurations GS3, GS4 and GS5, maintaining the inclination $i = 80°$ and $\alpha = 1$ but varying the orbital radius $r_o = \{8M, 10M, 12M\}$ (from left to right). From the analysis of these results, three main differences become apparent: 1) the diminishing of the size of the plunge through image, and in some cases even the vanishing, with the increase in the orbital radius; 2) the widening of the direct image; 3) the increase in the distance between the two secondary images, following the increase in $r_o$. The former can be explained by noting that an increase in the orbital radius demands a higher deflection of light to produce the same observational features. However, the deflection is the same for the same configuration which lead to a decrease in the brightness of the plunge-through image and its eventual vanishing, in some cases. This transition occurs for higher values of $r_o$ for less compact configurations, as displayed in figure 5.6. Note also that, the widening of

the primary image results directly from considering a higher hot spot orbit.

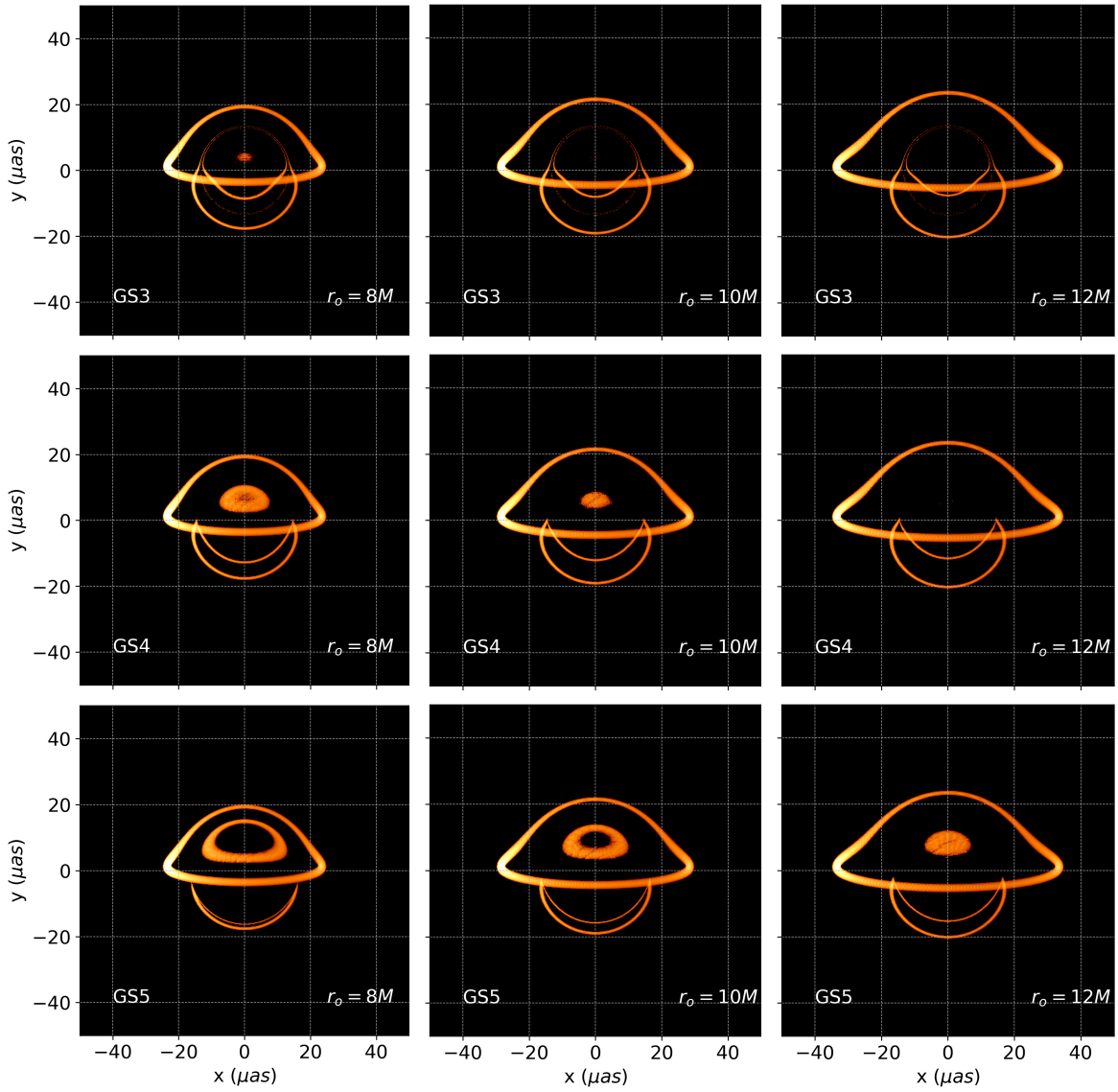


Figure 5.6: Time integrated images of a full orbit, assuming an isotropically emitting source, with a radius of $r_{HS} = M/2$, for the gravastar configurations with a radius, from top to bottom, of $a = \{3M, 4M, 5M\}$ and an orbital radius of $r_o = \{8M, 10M, 12M\}$, from left to right. For all the simulations it was set $\alpha = 1$ and an inclination of $i = 80°$.

Looking at figure 5.5, if the solid lines are extended to larger values of $r_o$ it is possible to picture more light trajectories intersecting the equatorial planes twice. This implies that, the photon geodesics that pass at a minimum radial distance from the centre, smaller than the gravastar radius, reach the observer's plane at lower impact parameters and thus appear closer to the centre of the compact object. On the other hand, for larger $r_o$, when the photon trajectories intersect each other and the equatorial plane, the outer secondary track has a larger impact parameter while the inner one has a smaller impact parameter. This means that the distance between the two secondary images grows when the orbital radius increases.

Besides the simulations present in figure 5.6, other simulations were performed varying the orbital radius $r_o = \{8M, 10M, 12M\}$ as well as the inclination $i = \{20°, 50°, 80°\}$ (see appendix 7).

### 5.1.3 Impact of the mass distribution

Let us now analyze the impact of the parameter $\alpha$, recalling that a change in its value leads to different mass distributions. When $\alpha = 1$ the total mass of the gravastar is distributed in its volume, but as its value decreases, the mass starts to be allocated both in the gravastar volume and surface until it reaches the limit of $\alpha_{min} = 1 - 2M/a$, where the mass is totally distributed at the surface of the gravastar in the form of a thin-shell. Figure 5.7 shows the integrated flux of GS3, GS4 and GS5 assuming $r_o = 8M$, $i = 80^\circ$ and $\alpha = \{1, \alpha_{min}\}$ where $\alpha_{min} = \{1/3, 1/2, 3/5\}$, respectively. For GS4 and GS5, the parameter $\alpha$ does not affect noticeably the results. However, a slight difference is observed in the plunge through image for the GS3 model, due to the weakened lensing of photons that cross the interior of the gravastar. Overall, these results show that, for both ultra compact and non-ultra compact gravastars, the effect of the value of $\alpha$ is subdominant in relation to the other parameters and therefore is not analyzed for further models.

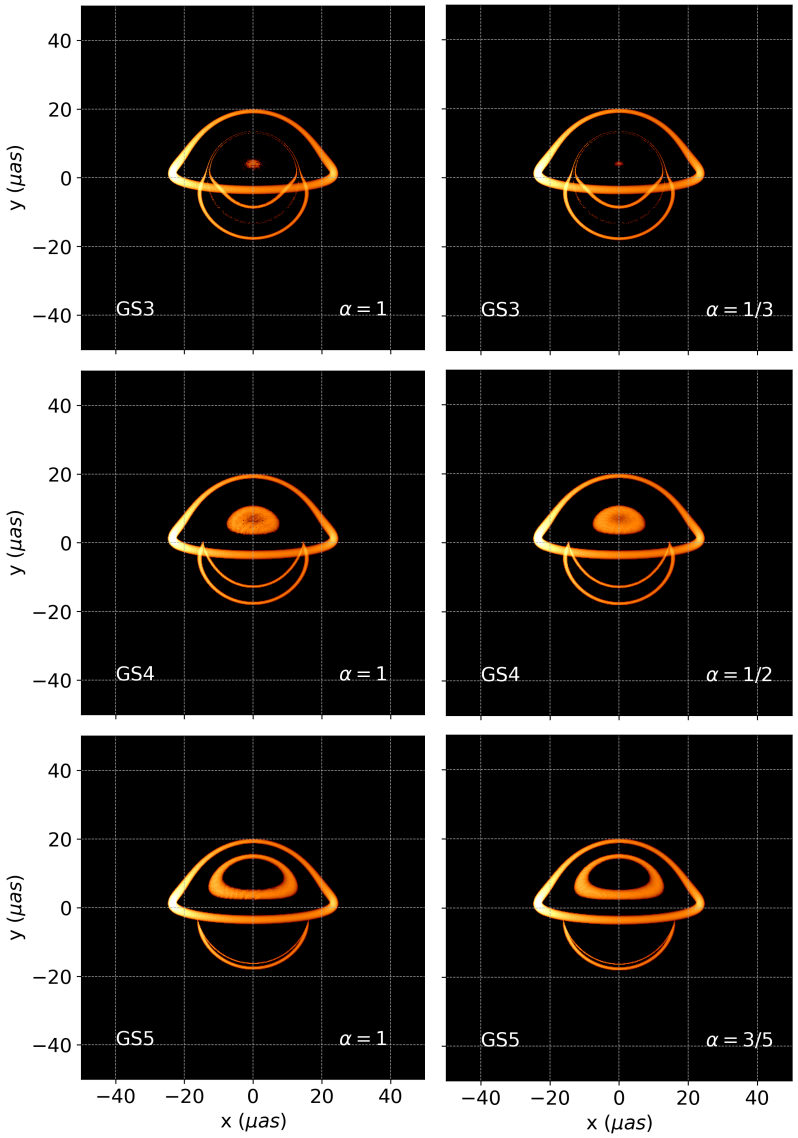


Figure 5.7: Time integrated images of a full orbit, assuming an isotropically emitting source, with a radius of $r_{HS} = M/2$, for the gravastar configurations with a radius, from top to bottom, of $a = \{3M, 4M, 5M\}$ and $\alpha = \{1,\ \alpha_{min}\}$, from left to right, where $\alpha_{min} = \{1/3,\ 1/2,\ 3/5\}$, respectively. For all the simulations it was set $r_o = 8M$ and an inclination of $i = 80^\circ$.

## 5.2 Magnitude and Centroid

In this section, the focus is on the temporal magnitudes and centroids results for a full orbit, obtained by Eq. 4.14 and Eq. 4.13, respectively. Figure 5.8 shows the temporal magnitudes in function of time (normalized by an orbital period) for a SBH, GS1-GS3 (top panels) and GS3, GS4 and GS5 (bottom panels) for $i = \{20°;\ 50°;\ 80°\}$ (left to right). These correspond to the temporal-integrated fluxes in figures 5.1 and 5.3 and thus assume a constant orbital radius of $r_o = 8M$ and $\alpha = 1$. Note that $t = 0$ does not necessarily correspond to the same point in the orbit for all models, which explains some deviations between curves. For an inclination of 20° and 50° a central peak is observed for all gravastar configurations and the SBH. This is due to the relativistic Doppler shift and corresponds to the moment in which the hot-spot is moving towards the observer. This result also indicates that the amount of observed features remains constant for these inclinations and thus no additional peak is detected. This explains why there is no remarkable difference between the curves and thus all of them show the same qualitative behaviour as the SBH case.

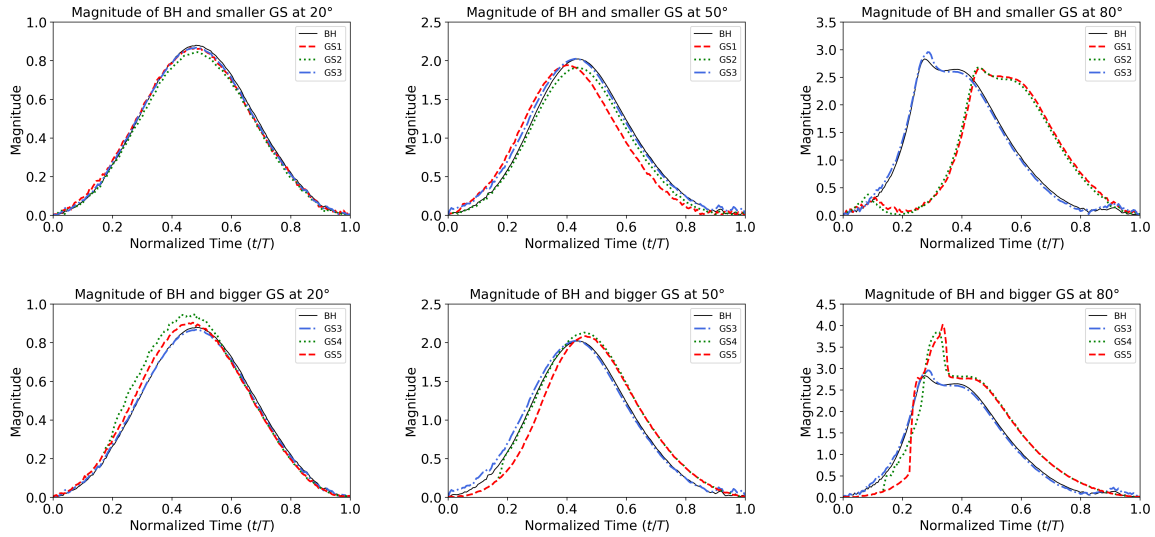


Figure 5.8: Temporal magnitudes for a full orbit, assuming an isotropically emitting source, with a radius of $r_{HS} = M/2$, with an inclination of $i = \{20°, 50°, 80°\}$ for the SBH and gravastar configurations with a radius of: $a = \{2.25M, 2.5M, 3M\}$ (top panels); $a = \{3M, 4M, 5M\}$ (bottom panels). For all the simulations it was set $\alpha = 1$ and an orbital radius of $r_o = 8M$. The time is normalized by an orbital period.

For a higher inclination the case changes and some differences are visible. For the SBH and GS1-GS3 configurations an additional bump is present. This is due to the contribution of the Doppler shift of the secondary images. Note that this bump for GS3 has a slightly larger magnitude which can be explained by the presence of the plunge through image, scarcely present for the other compact configurations. Note that, for these models, some slight numerical noise is present for lower temporal magnitude values. This is caused by the presence of LR photons. When performing the simulation, these photons are not always present for the whole orbit of the hot spot, due to the limited resolution of the simulation. Since the magnitude obtained by equation 4.14 behaves logarithmically with the flux, the LR photons have a bigger contribution for smaller values of magnitude. On the other hand, for GS4 and GS5 configurations the curves are smoother and no noise is detected due to the absence of a photon sphere. For these configurations and an inclination of 80°, the additional peak right before the central one is more pronounced. As seen in figure 5.3, not only the beaming of the secondary images contributes to this

extra feature but also the weakly lensed photons that cross the centre of the gravastar. As discussed in Ref. [88], when the secondary track appears as a single image, a bump in the magnitude is expected, that decreases when this separates into two. When they are merged again, before vanishing, another peak is present. The third peak observed corresponds to the aforementioned central one. A similar behaviour was expected for GS4 and GS5, however, it is not possible to distinguish these three peaks since they are overlapped with the central peak. Lastly, the corresponding magnitude of the peaks increase with inclination. Looking at figure 5.1 and 5.3 the left side of the direct image is clearly brighter for higher inclinations. This translates into an increase in the Doppler effect and thus a larger value of magnitude.

The temporal centroids of the same configurations are now displayed in figure 5.9. As in the temporal magnitudes, $i = \{20°;\ 50°;\ 80°\}$ (left to right) where the results also correspond to the temporal-integrated fluxes in figures 5.1 and 5.3. Note that for $i = 80°$ the y-axis has a smaller range than for other inclinations in order to provide a better distinction between different curves.

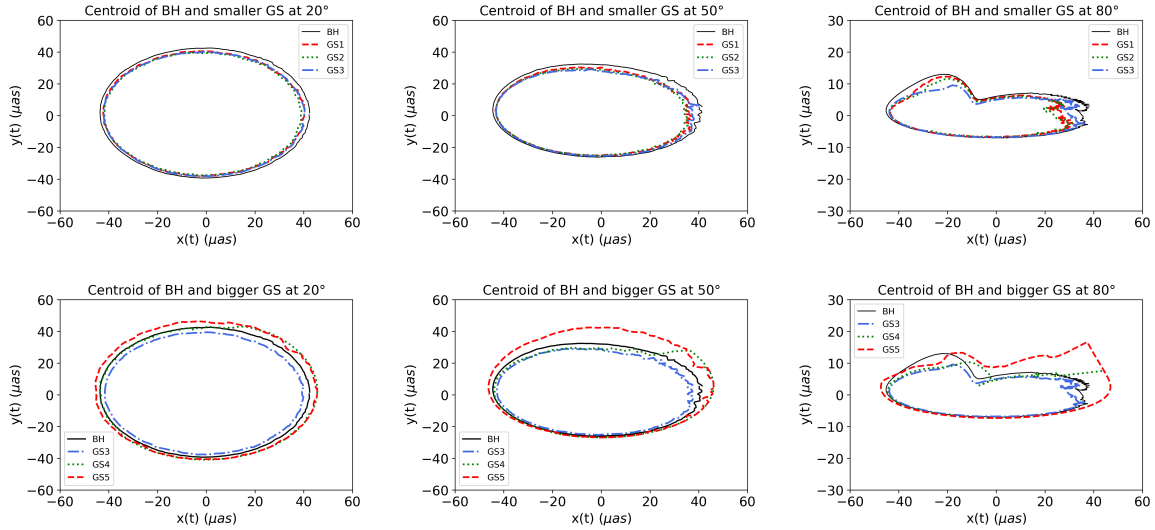


Figure 5.9: Temporal centroids for a full orbit, assuming an isotropically emitting source, with a radius of $r_{HS} = M/2$, as the source with an inclination of $i = \{20°, 50°, 80°\}$ for the SBH and gravastar configurations with a radius of: $a = \{2.25M, 2.5M, 3M\}$ (top panels); $a = \{3M, 4M, 5M\}$ (bottom panels). For all the simulations it was set $\alpha = 1$ and an orbital radius of $r_o = 8M$.

Recalling the centroid definition in the previous chapter, there are three main possibilities:

1. When only direct image is present, the centroid corresponds directly to the trajectory of the hot-spot, approximating to a distorted ellipse;

2. When besides the direct image, the same amount of secondary images is present for the full orbit, although the centroid trajectory does not correspond to the hot-spot orbit, it still approximates to a distorted ellipse but with smaller dimensions;

3. When an image is not always present for the whole orbit, its appearance causes a shift in the centroid. In some cases, this displacement occurs due to Doppler shifting.

Let us now study each case individually. For compact configurations and lower inclinations $i = 20° - 50°$, the trajectories of the centroids do resemble a distorted ellipse, since the same amount of features is present for a full orbit. However, the centroid of these models follow a slightly smaller

trajectory compared to the SBH solution, since an extra inner secondary image is present in all of them. For $i = 80°$, when the hot-spot passes behind the ultra compact objects, the beaming of the secondary tracks increases in the left side of the integrated images (see fig. 5.1), causing a shift to the centre on the centroid trajectory for GS1-GS3 models. After this deviation, the Doppler shift is reduced and the centroid gets further away from the centre. Additionally, as in the magnitude graphs, numerical noise is also evident due to the presence of LR photons in all of these models. On the other hand, for GS4 and GS5, the case is different and some changes are observed. For $i = 20°$, the centroid trajectory is larger for GS5 than for the SBH. Since this gravastar configuration has no secondary image or LR present, the centroid follows exactly the trajectory of the hot-spot. Considering the same inclination, something slightly different is observed for GS4. In this configuration, for a certain time interval, only the direct image is present and thus the centroids follow the same path as GS5. However, as seen in the integrated images, two secondary images are present, that seem to coincide, and thus the centroid trajectory assumes a similar trajectory as the SBH, since this solution has only one secondary track. When the inclination is increased to 50°, the separation between the secondary images is detectable. Because of this, when these signatures are present the centroid follows a similar trajectory to the GS3 that has the same amount of secondary tracks. When only the direct image is visible, as mentioned before, the centroid path is the same as GS5. For the larger gravastar (GS5) the same is observed as for a lower inclination, since there is still no secondary tracks present. For $i = 80°$, both GS4 and GS5 display a deviation to the centre as for the most compact cases. However, for the models with a lower compacticity, this shift occurs, not because an increase in beaming is present, but due to the appearance of the secondary images. A slight difference in the moment that the centroid deviates is also visible between GS3, GS4 and GS5. This only indicates that the cause for the shift occurs at different instants for these configurations. Note also that, unlike the more compact solutions, the centroid curves are smoother for GS4 and GS5, consistently with the non-existence of LR photons in these configurations. Overall, both the magnitude and centroid results of the gravastar configurations approximate to the SBH solution with some exceptions for non-ultra compact models.

Figure 5.10 shows the magnitude (top panels) and centroids (bottom panels) corresponding to the integrated images of figure 5.4 on the left and figure 5.7 on the right.

Focusing on the left column first, the transition between GS3 and GS4 model is straightforward when also considering the GS35 configuration. The bump before the central peak that is observed in the magnitude plot (top image), is larger in GS35 model than the GS3, but smaller than GS4, although closer to the latter. This is mostly due to the enlargement of the plunge-through image, whose size is closer to that of the GS4 (see figure 5.4). Regarding the centroids, the main difference lies at the point in which the shift to the centre occurs. In GS3, the secondary images are always present for the full orbit while for GS35 the same is not true and thus the secondary images appear at a latter instant for GS35 than the increase in the beaming for GS3, delaying the centroid deviation to the centre. Note that, some numerical noise is still present for GS35 configuration, since it is a transition configuration and the considered resolution is lower than the one used in the GS3 model.

Focusing now on the right column of figure 5.10, no major difference is detected, for both magnitude and centroid plots, reinforcing the sub-dominance in the results of the parameter $\alpha$, being this in agreement with the integrated flux results.

Lastly, figure 5.11 exhibits the magnitude (top panels) and centroids (bottom panels) corresponding to the integrated images of figure 5.6 (using the same parameters).

Let us first centre our attention on the magnitude results. When the distance between the hot-spot and the gravastar increases, the orbital velocity of the light source decreases and thus the effect of Doppler

shifting is smaller. Because of this, the magnitude of the peak assumes higher values for lower orbital radius in all configurations. Focusing on the magnitudes for GS3 model, the only visible difference in the time-integrated images (see figure 5.6) is the vanishing of the plunge-through image for $r_o \geq 10M$. However, this difference is not detectable in the temporal magnitudes. For the GS4, the magnitude curves for $r_o = 8M$ and $r_o = 10M$ seem to have the same shape while for a larger orbital radius the higher peak is reduced due to the vanishing of the plunge through image, assuming a similar form to the magnitude curves of GS3. The magnitude of the GS5 configuration shows similar results in the sense that curves for $r_o = 8M$ and $r_o = 10M$ follow the same pattern whilst for $r_o = 12M$ it changes. However, the reason why this occurs is different from GS4. It is visible in figure 5.6 that one of the signatures of the integrated image of GS5 that varies, is the plunge-through image. For $r_o \leq 10M$, this feature is separated into a closed track with two images, whereas for a larger value these merge originating a single image. With this being said, for a smaller orbital radius, the plunge-through image remains in the observer's sky for a longer period of time, causing a widening in the peak of the magnitude and contributing with the three additional peaks previously mentioned for closed tracks.

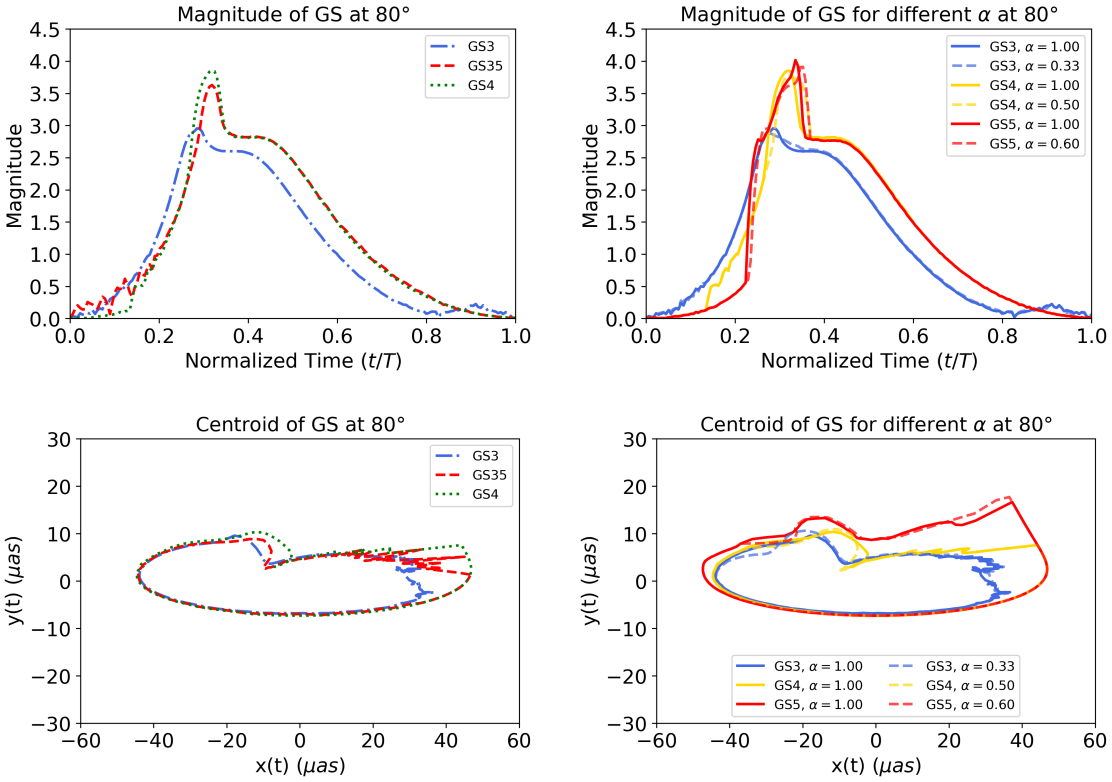


Figure 5.10: Temporal magnitudes (top plots) and centroids (bottom plots) for a full orbit, assuming an isotropically emitting source, with a radius of $r_{HS} = M/2$, for the gravastar configurations with a radius of: $a = \{3M, 3.5M, 4M\}$ (left panels); $a = \{3M, 4M, 5M\}$ (right panels). The value of $\alpha$ is set to 1 for the left plots but assumes the values of $\alpha = 1$ (solid lines) and $\alpha = \alpha_{min}$ (dashed lines) for the right plots. For all the simulations it was set $i = 80°$ and an orbital radius of $r_o = 8M$.

Regarding the centroids, the increase in the orbital radius increases the size of the centroid trajectory for all cases. However, these results do not show any more significant differences, since the only distinction in the integrated images present in figure 5.6 is the vanishing of the central feature.

As previously mentioned, further simulations were performed, varying both the orbital radius and the inclination. The corresponding magnitudes and centroids can be found in the Appendix.

Summarizing, the aforementioned results are in agreement with the results of the integrated images,

providing complementary information regarding the Doppler effect and the moments in which each image appears.

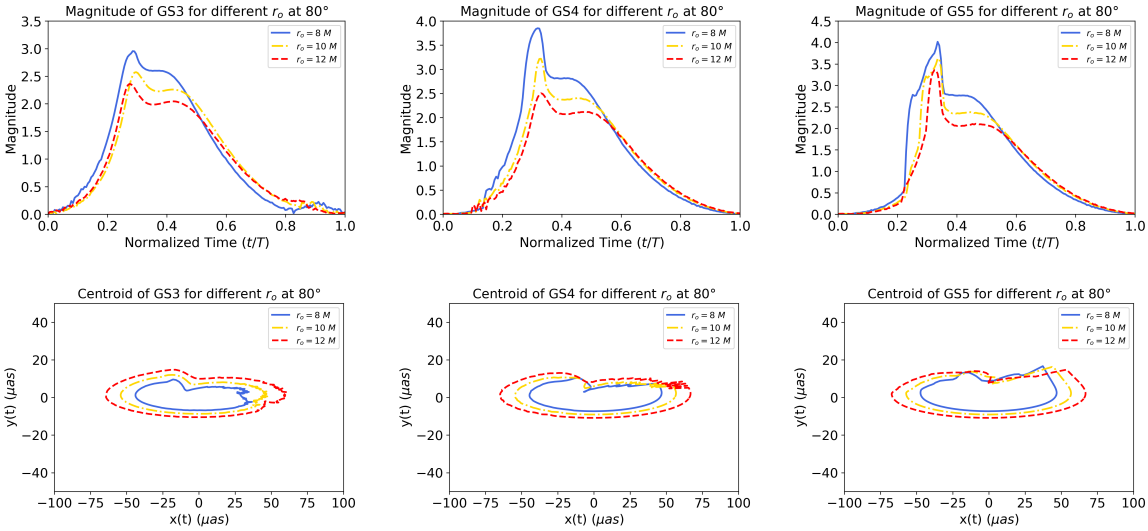


Figure 5.11: Temporal magnitudes (top plots) and centroids (bottom plots) for a full orbit, assuming an isotropically emitting source, with a radius of $r_{HS} = M/2$, for the gravastar configurations with a radius of $a = \{3M, 4M, 5M\}$ (from left to right) and an orbital radius of: $r_o = 8M$ (blue solid line); $r_o = 10M$ (yellow dash-dotted line); $r_o = 12M$ (red dashed line). For all the simulations it was set $\alpha = 1$ and $i = 80°$.

# Chapter 6

# Conclusion

In this dissertation we have studied the observational signatures of isotropically emitting sources, known as hot spots, orbiting different thin-shell gravastar models. From these models, we analyzed the repercussions of the gravastar radius and mass distribution, along with the impacts of the orbital radius and observation inclination in the results. For ultra compact gravastar configurations, the astrometrical observables, namely the time integrated fluxes, temporal magnitudes and centroids, closely resemble the ones for the Schwarzschild black hole spacetime. Since these gravastar models only feature one additional secondary track, they are even more similar to the Schwarzschild black hole case than other studied ECOs that feature two additional such contributions. Note, however, that for higher observation angles the plunge through image becomes visible and thus configurations with a lower observation inclination provide more similar signatures to those of black hole spacetimes.

For the non ultra compact configurations, we verified that the observables depend strongly on the orbital radius of the source, as well as on the observation inclination, which leads to distinct contributions from those observed for the Schwarzschild black hole. Due to this, we can not guarantee the compatibility between these gravastar models and the black hole scenario. Lastly, the mass distribution ratio within the thin-shell has proved to play a sub dominant role compared to the other parameters, affecting only the plunge through contribution for ultra compact configurations, having thus a negligible impact. However, in [1] this parameter is revealed to be rather significant when considering accretion disks. The main reason for this distinction is that the hot spot orbits the gravastar at a constant radius which leads to a constant gravitational redshift effect, while the accretion disk models are extended through various radial coordinates. Due to this, the impacts of the parameter $\alpha$ are more pronounced when considering an accretion disk as the emission source. From this study exclusively, we conclude that ultra compact thin-shell gravastar models are plausible black hole mimicker candidates since the current generation of instruments do not have enough resolution to distinguish the additional features present in gravastar spacetimes.

There are, however, some limitations in the gravastar model itself and in the performed study that leave space for improvement in the future. Regarding gravastars, the major drawback of these objects is the lack of an acceptable formation mechanism. On the other hand, we assume that the thin shell gravastar configurations are static, and although it was proved that rotation is a subdominant parameter that only affects the results quantitatively, we know that compact objects are dynamic in nature, and thus including rotation in these models provides a more realistic scenario. Additionally, the hot spot is modelled as an uniform sphere that emits isotropically with no internal physics taken into account. This is a very simplified model that discards any type of polarization or magneto-hydrodynamics of the hot spot. Since this isotropically emitting source is supposed to model the inhomogeneities in the accretion

disk, they are most likely not uniform spheres and their physics must be taken into account to provide a more realistic description. Nonetheless, note that this work is just a first approximation and in the future we plan to work with more realistic models. Besides this, in future work we can study more generalized models of gravastars with thick shells or even other exotic compact objects. For example, it might be interesting to study a recently proposed object known as nestar, which consists on a "nest" of gravastars, i.e. a gravastar spacetime inside of another gravastar spacetime [141].

The main aim of this investigation is not only to compare the gravastar observational signatures with those of black holes, but also provide the gravastar's expected visual appearance to potentially detect these objects in the future. Despite the low resolution of current observations, we hope that the next generation of the EHT and the GRAVITY instrument, are precise enough to corroborate or exclude some of the proposed models and provide new insights in the supermassive compact objects field.

# Chapter 7

# Appendix

Figures 7.1, 7.2 and 7.3 display the integrated fluxes for the gravastar configurations GS3, GS4 and GS5, respectively, varying the orbital radius $r_o = \{8M, 10M, 12M\}$ as well as the inclination $i = \{20°, 50°, 80°\}$, for a fixed value of $\alpha = 1$. Beyond the study performed in chapter 5, only GS4 and GS5 show some noteworthy results. In the configuration with $a = 4M$ and $i = 20°$ the secondary image tends to form a closed path acquiring similar features to the ones observed for the SBH case (see figure 5.3 or 5.1). For GS5 and $r_o = 12M$ a secondary track is present for a lower inclination of $i = 50°$ instead of $i = 80°$, as predicted in the analysis of the photon geodesics for this configuration.

Figures 7.4, 7.5 and 7.6 exhibit the magnitudes (top panels) and centroids (bottom panels) corresponding to the integrated images of figures 7.1, 7.2 and 7.3, respectively, using the same parameters. From these results, only GS5 shows some noteworthy features. For $i = 50°$ and $r_o = 12M$ there is a clear difference in the centroid trajectory due to the appearance of the secondary image for these specific parameters. Regarding the magnitude the difference is scarcely noticed but a slight bump seems to appear around $t = 0.3T$.

## 7. APPENDIX

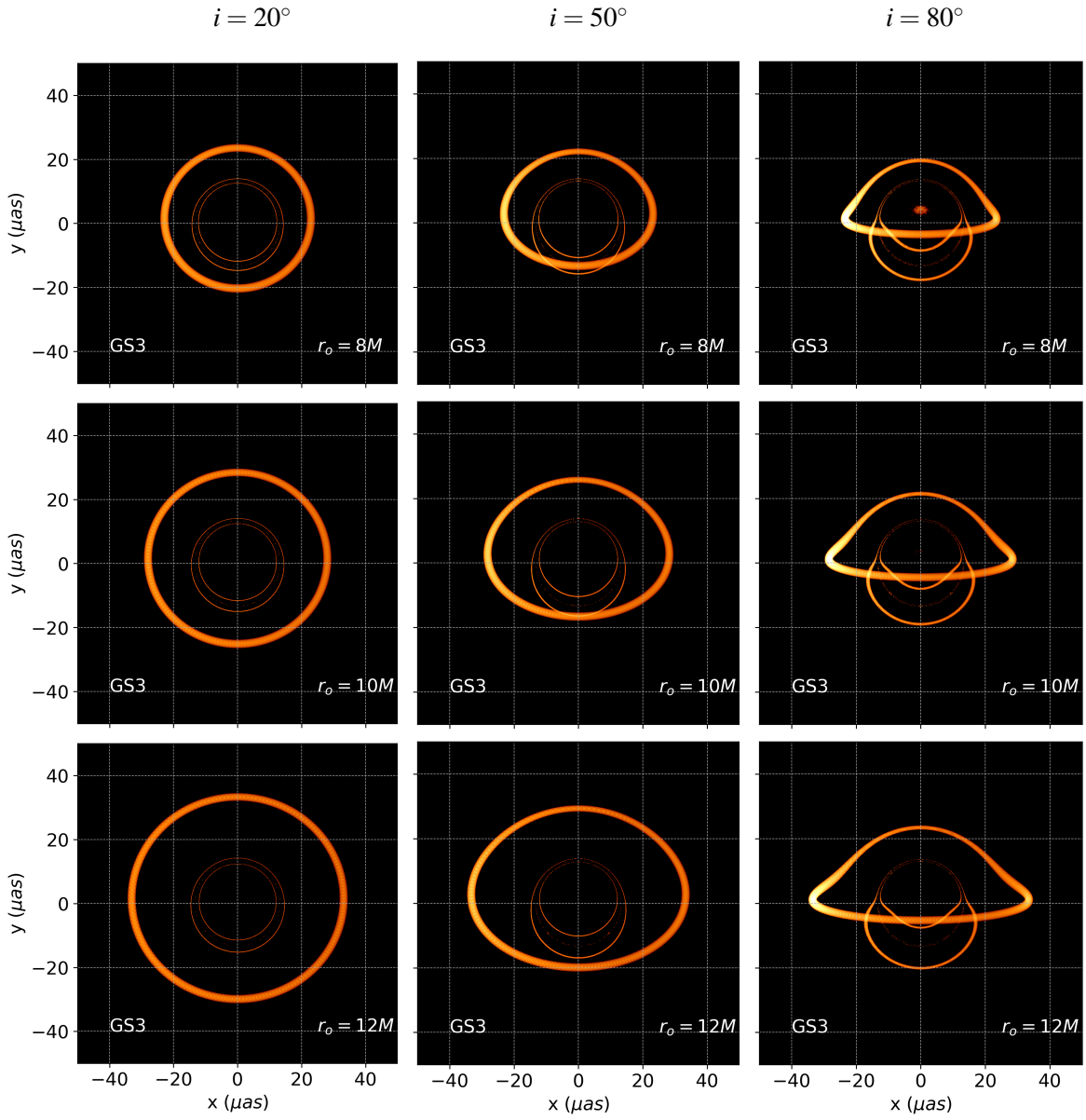


Figure 7.1: Time integrated images of a full orbit, assuming an isotropically emitting source, with a radius of $r_{HS} = M/2$, for GS3 with an orbital radius of $r_o = \{8M, 10M, 12M\}$, from top to bottom and $i = \{20°, 50°, 80°\}$, from left to right. For all the simulations it was set $\alpha = 1$.

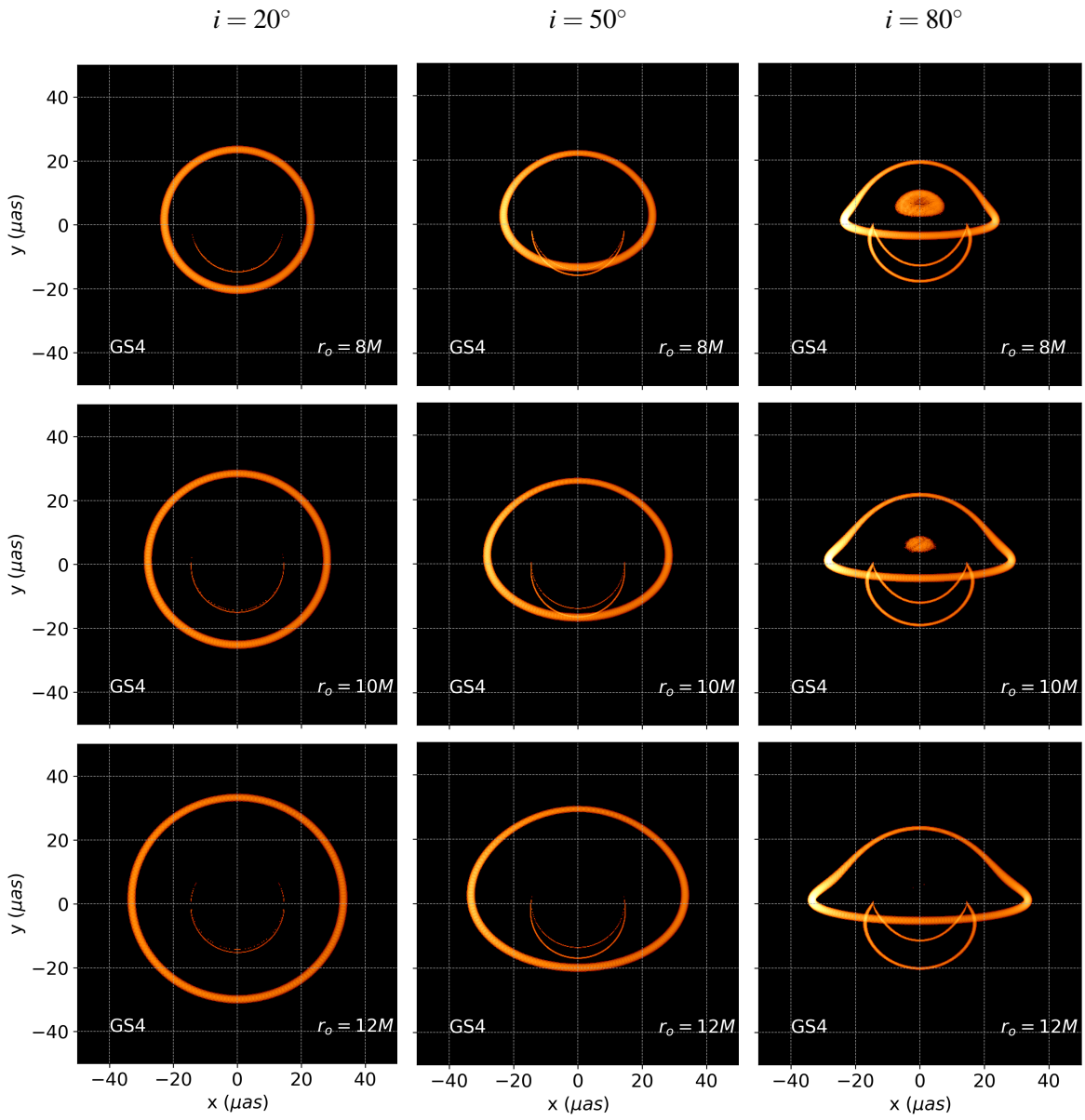


Figure 7.2: Time integrated images of a full orbit, assuming an isotropically emitting source, with a radius of $r_{HS} = M/2$, for GS4 with an orbital radius of $r_o = \{8M, 10M, 12M\}$, from top to bottom and $i = \{20°, 50°, 80°\}$, from left to right. For all the simulations it was set $\alpha = 1$.

# 7. APPENDIX

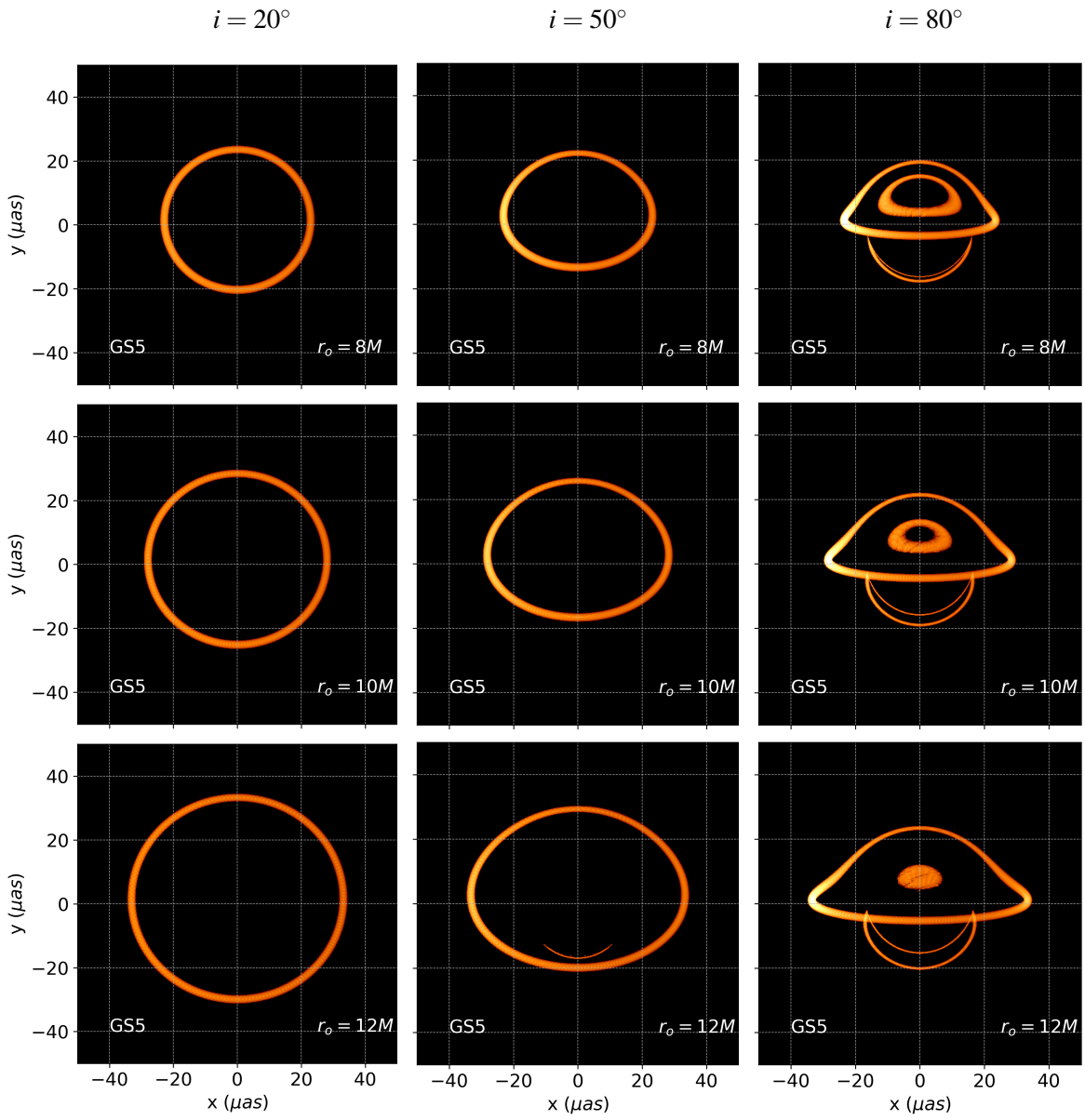


Figure 7.3: Time integrated images of a full orbit, assuming an isotropically emitting source, with a radius of $r_{HS} = M/2$, for GS5 with an orbital radius of $r_o = \{8M, 10M, 12M\}$, from top to bottom and $i = \{20°, 50°, 80°\}$, from left to right. For all the simulations it was set $\alpha = 1$.

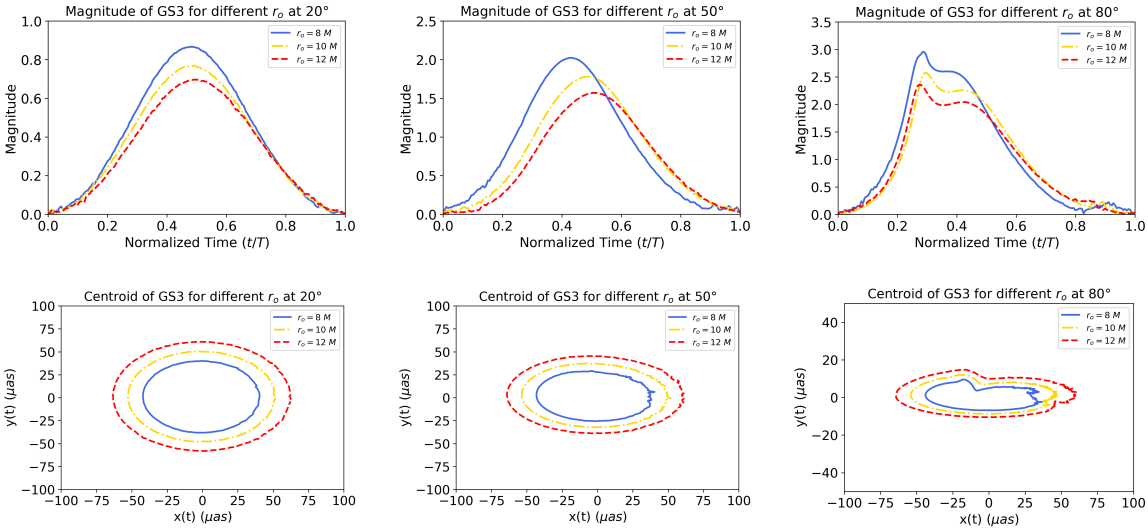


Figure 7.4: Temporal magnitudes (top plots) and centroids (bottom plots) for a full orbit, assuming an isotropically emitting source, with a radius of $r_{HS} = M/2$, for GS3 with $i = \{20°, 50°, 80°\}$ and an orbital radius of: $r_o = 8M$ (blue solid line); $r_o = 10M$ (yellow dash-dotted line); $r_o = 12M$ (red dashed line). For all the simulations it was set $\alpha = 1$.

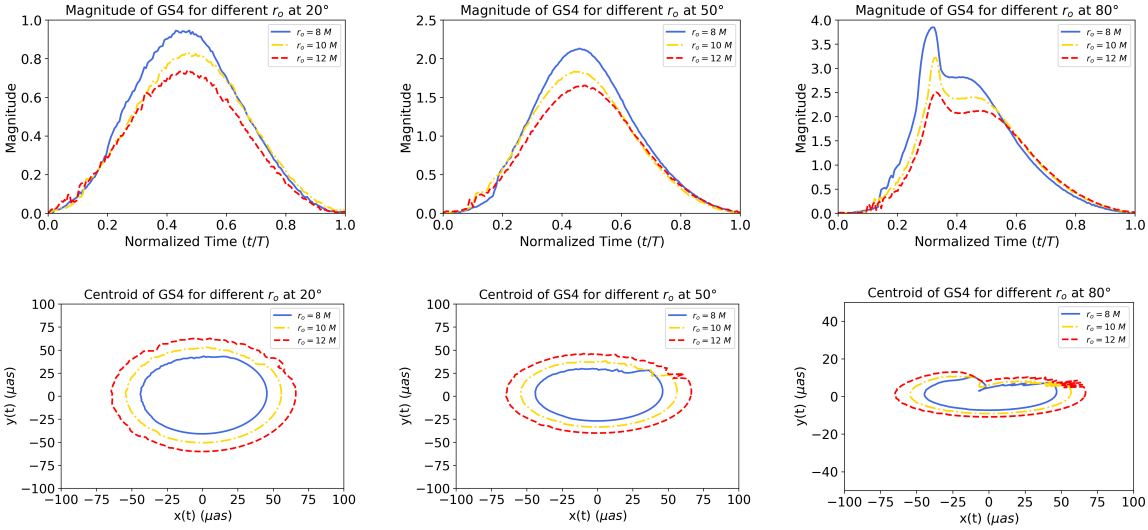


Figure 7.5: Temporal magnitudes (top plots) and centroids (bottom plots) for a full orbit, assuming an isotropically emitting source, with a radius of $r_{HS} = M/2$, for GS4 with $i = \{20°, 50°, 80°\}$ and an orbital radius of: $r_o = 8M$ (blue solid line); $r_o = 10M$ (yellow dash-dotted line); $r_o = 12M$ (red dashed line). For all the simulations it was set $\alpha = 1$.

# 7. APPENDIX

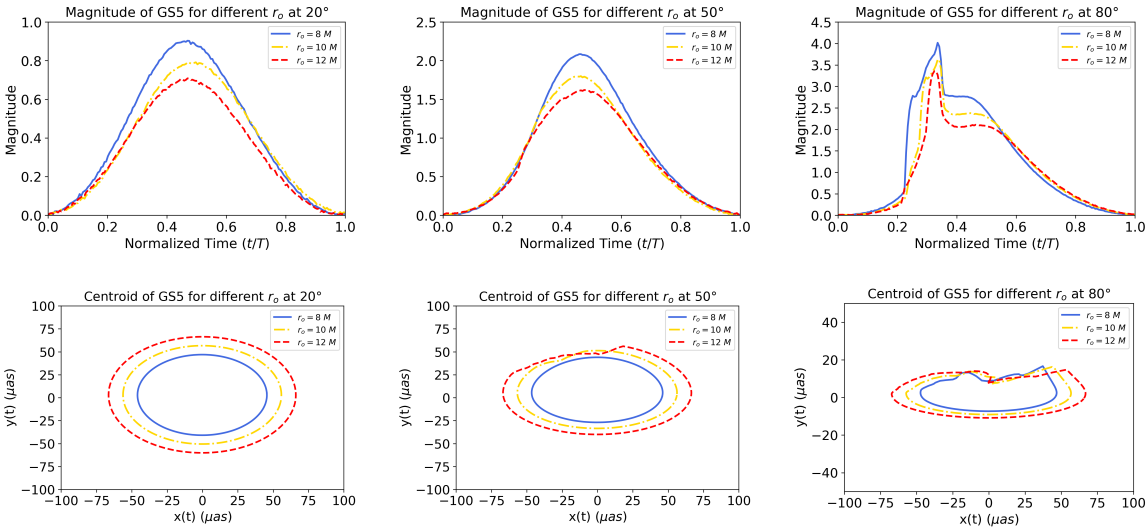


Figure 7.6: Temporal magnitudes (top plots) and centroids (bottom plots) for a full orbit, assuming an isotropically emitting source, with a radius of $r_{HS} = M/2$, for GS5 with $i = \{20°, 50°, 80°\}$ and an orbital radius of: $r_o = 8M$ (blue solid line); $r_o = 10M$ (yellow dash-dotted line); $r_o = 12M$ (red dashed line). For all the simulations it was set $\alpha = 1$.

# Bibliography


1. Rosa, J. a. L., Cordeiro, D. S. J., Macedo, C. F. B. & Lobo, F. S. N. Observational imprints of gravastars from accretion disks and hot spots. *Phys. Rev. D* **109,** 084002. https://link.aps.org/doi/10.1103/PhysRevD.109.084002 (8 2024).
2. Michell, J. VII. On the means of discovering the distance, magnitude, &c. of the fixed stars, in consequence of the diminution of the velocity of their light, in case such a diminution should be found to take place in any of them, and such other data should be procured from observations, as would be farther necessary for that purpose. By the Rev. John Michell, BDFRS In a letter to Henry Cavendish, Esq. FRS and AS. *Philosophical transactions of the Royal Society of London,* 35–57 (1784).
3. Montgomery, C., Orchiston, W. & Whittingham, I. Michell, Laplace and the origin of the black hole concept. *Journal of Astronomical History and Heritage* **12,** 90–96 (2009).
4. Laplace, P. S. Beweis des Satzes, dass die anziehende Kraft bey einem Weltkörper so gross seyn könne, dass das Licht davon nicht ausströmen kann. *Allgemeine Geographische Ephemeriden* **4,** 1–6 (1799).
5. Robinson, A. *The Last Man Who Knew Everything: Thomas Young, the Anonymous Polymath Who Proved Newton Wrong, Explained How We See, Cured the Sick, and Deciphered the Rosetta Stone, Among Other Feats of Genius (Revised Edition)* (Open Book Publishers, 2023).
6. Stachel, J. *et al.* Einstein's miraculous year. *Five Papers that Changed* (1998).
7. Einstein, A. Die feldgleichungen der gravitation. *Sitzungsberichte der Königlich Preußischen Akademie der Wissenschaften,* 844–847 (1915).
8. Schwarzschild, K. Über das gravitationsfeld eines massenpunktes nach der einsteinschen theorie. *Sitzungsberichte der königlich preussischen Akademie der Wissenschaften,* 189–196 (1916).
9. Black Hole, N. in *The Oxford English Dictionary*. URL: https://doi.org/10.1093/OED/9016006593. (Accessed in 22 November 2023).
10. Rindler, W. Visual horizons in world models. *Monthly Notices of the Royal Astronomical Society* **116,** 662–677 (1956).
11. Carroll, S. M. An introduction to general relativity: spacetime and geometry. *Addison Wesley* **101,** 102 (2004).
12. Frolov, V. & Novikov, I. *Black hole physics: Basic concepts and new developments* (Springer Science & Business Media, 2012).
13. Oppenheimer, J. R. & Volkoff, G. M. On massive neutron cores. *Physical Review* **55,** 374 (1939).
14. Oppenheimer, J. R. & Snyder, H. On continued gravitational contraction. *Physical Review* **56,** 455 (1939).

15. Chandrasekhar, S. The maximum mass of ideal white dwarfs. *Astrophysical Journal, vol. 74, p. 81* **74,** 81 (1931).

16. Landau, L. To the Stars theory. *Phys. Zs. Sowjet* **1,** 285 (1932).

17. Yakovlev, D. G., Haensel, P., Baym, G. & Pethick, C. Lev Landau and the concept of neutron stars. *Physics-Uspekhi* **56,** 289 (2013).

18. Kalogera, V. & Baym, G. The maximum mass of a neutron star. *The Astrophysical Journal* **470,** L61 (1996).

19. Ryder, L. *Introduction to general relativity* (Cambridge University Press, 2009).

20. Mirabel, F. The formation of stellar black holes. *New Astronomy Reviews* **78,** 1–15 (2017).

21. Wolfe, A. & Burbidge, G. Black holes in elliptical galaxies. *Astrophysical Journal, vol. 161, p. 419* **161,** 419 (1970).

22. Abbott, B. *et al.* Binary black hole population properties inferred from the first and second observing runs of Advanced LIGO and Advanced Virgo. *The Astrophysical Journal Letters* **882,** L24 (2019).

23. Baibhav, V. *et al.* The mass gap, the spin gap, and the origin of merging binary black holes. *Physical Review D* **102,** 043002 (2020).

24. Kerr, R. P. Gravitational field of a spinning mass as an example of algebraically special metrics. *Physical review letters* **11,** 237 (1963).

25. Reissner, H. Über die Eigengravitation des elektrischen Feldes nach der Einsteinschen Theorie. *Annalen der Physik* **355,** 106–120 (1916).

26. Weyl, H. Zur gravitationstheorie. *Annalen der physik* **359,** 117–145 (1917).

27. Nordstrom, G. On the Energy of the Gravitational Field in Einstein's Theory II Verhandl. *Koninkl. Ned. Akad. Wetenschap., Afdel. Natuurk., Amsterdam* **26,** 1201–1208 (1918).

28. Jeffery, G. B. The field of an electron on Einstein's theory of gravitation. *Proceedings of the Royal Society of London. Series A, Containing Papers of a Mathematical and Physical Character* **99,** 123–134 (1921).

29. Newman, E. T. & Janis, A. Note on the Kerr spinning-particle metric. *Journal of Mathematical Physics* **6,** 915–917 (1965).

30. Newman, E. T. *et al.* Metric of a rotating, charged mass. *Journal of mathematical physics* **6,** 918–919 (1965).

31. Yajima, H. & Tamaki, T. Black hole solutions in Euler-Heisenberg theory. *Physical Review D* **63.** ISSN: 1089-4918. `http://dx.doi.org/10.1103/PhysRevD.63.064007` (2001).

32. Bardeen, J. M. *Non-singular general-relativistic gravitational collapse* in *Proceedings, 5th International Conference on Gravitation and the Theory of Relativity, Tbilisi, USSR,* (1968), 174.

33. Frolov, V. P. Notes on nonsingular models of black holes. *Physical Review D* **94,** 104056 (2016).

34. Sen, A. Rotating charged black hole solution in heterotic string theory. *Physical Review Letters* **69,** 1006 (1992).

35. Wheeler, J. A. Our universe: the known and the unknown. *The American Scholar,* 248–274 (1968).

36. Hawking, S. W. & Israel, W. *Three hundred years of gravitation* (Cambridge University Press, 1987).

37. Kato, S., Fukue, J. & Mineshige, S. *Black-Hole Accretion Disks—Towards a New Paradigm—* (2008).

38. Bowyer, S, Byram, E., Chubb, T. & Friedman, H. Cosmic X-ray sources. *Science* **147,** 394–398 (1965).

39. Liu, Q. & Mirabel, I. A catalogue of ultraluminous X-ray sources in external galaxies. *Astronomy & Astrophysics* **429,** 1125–1129 (2005).

40. Corral-Santana, J. M. *et al.* BlackCAT: A catalogue of stellar-mass black holes in X-ray transients. *Astronomy & Astrophysics* **587,** A61 (2016).

41. Chen, S., Jing, J., Qian, W.-L. & Wang, B. Black hole images: A review. *Science China Physics, Mechanics & Astronomy* **66,** 260401 (2023).

42. Takahashi, R. Shapes and positions of black hole shadows in accretion disks and spin parameters of black holes. *The Astrophysical Journal* **611,** 996 (2004).

43. Luminet, J.-P. Image of a spherical black hole with thin accretion disk. *Astronomy and Astrophysics* **75,** 228–235 (1979).

44. Da Silva, L. F. D., Lobo, F. S., Olmo, G. J. & Rubiera-Garcia, D. Photon rings as tests for alternative spherically symmetric geometries with thin accretion disks. *Physical Review D* **108,** 084055 (2023).

45. Harko, T., Kovács, Z. & Lobo, F. S. Can accretion disk properties distinguish gravastars from black holes? *Classical and Quantum Gravity* **26,** 215006 (2009).

46. Abramowicz, M. A. & Fragile, P. C. Foundations of black hole accretion disk theory. *Living Reviews in Relativity* **16,** 1–88 (2013).

47. Bardeen, J. M. *et al.* Timelike and null geodesics in the Kerr metric. *Black holes* **215** (1973).

48. Cunningham, C. & Bardeen, J. M. The optical appearance of a star orbiting an extreme Kerr black hole. *Astrophysical Journal, Vol. 183, pp. 237-264 (1973)* **183,** 237–264 (1973).

49. Palmer, L, Pryce, M & Unruh, W. *Simulation of starlight lensed by a camera orbiting a Schwarzschild black hole* 1978.

50. Falcke, H., Melia, F. & Agol, E. Viewing the shadow of the black hole at the galactic center. *The Astrophysical Journal* **528,** L13 (1999).

51. Doeleman, S. *et al.* Structure of Sagittarius A$^*$ at 86 GHz using VLBI closure quantities. *The Astronomical Journal* **121,** 2610 (2001).

52. Doeleman, S. *et al.* Imaging an event horizon: submm-VLBI of a super massive black hole. *arXiv preprint arXiv:0906.3899* (2009).

53. Luminet, J.-P. An illustrated history of black hole imaging: Personal recollections (1972-2002). *arXiv preprint arXiv:1902.11196* (2019).

54. Gillessen, S *et al.* Variations in the spectral slope of sagittarius A$^*$ during a near-infrared flare. *The Astrophysical Journal* **640,** L163 (2006).

55. Aasi, J. *et al.* Advanced ligo. *Classical and quantum gravity* **32,** 074001 (2015).

56. Acernese, F. a. *et al.* Advanced Virgo: a second-generation interferometric gravitational wave detector. *Classical and Quantum Gravity* **32,** 024001 (2014).

57. Abbott, B. P. *et al.* Observation of gravitational waves from a binary black hole merger. *Physical review letters* **116,** 061102 (2016).

58. Castelvecchi, D. & Witze, A. Einstein's gravitational waves found at last. *Nature news* **11** (2016).

59. Perlick, V. & Tsupko, O. Y. Calculating black hole shadows: review of analytical studies. *Physics Reports* **947,** 1–39 (2022).

60. Gralla, S. E., Holz, D. E. & Wald, R. M. Black hole shadows, photon rings, and lensing rings. *Physical Review D* **100,** 024018 (2019).

61. Cunha, P. V. & Herdeiro, C. A. Shadows and strong gravitational lensing: a brief review. *General Relativity and Gravitation* **50,** 1–27 (2018).

62. Vincent, F. H., Paumard, T., Gourgoulhon, E. & Perrin, G. GYOTO: a new general relativistic ray-tracing code. *Classical and Quantum Gravity* **28,** 225011 (2011).

63. Bozza, V. Gravitational lensing by black holes. *General Relativity and Gravitation* **42,** 2269–2300 (2010).

64. Johnson, M. D. *et al.* Universal interferometric signatures of a black hole's photon ring. *Science advances* **6,** eaaz1310 (2020).

65. Gralla, S. E. & Lupsasca, A. Lensing by Kerr black holes. *Physical Review D* **101,** 044031 (2020).

66. Gralla, S. E., Lupsasca, A. & Marrone, D. P. The shape of the black hole photon ring: A precise test of strong-field general relativity. *Physical Review D* **102,** 124004 (2020).

67. Pesce, D. W. *et al.* Toward determining the number of observable supermassive black hole shadows. *The Astrophysical Journal* **923,** 260 (2021).

68. Wielgus, M. Photon rings of spherically symmetric black holes and robust tests of non-Kerr metrics. *Physical Review D* **104,** 124058 (2021).

69. Broderick, A. E., Tiede, P., Pesce, D. W. & Gold, R. Measuring spin from relative photon-ring sizes. *The Astrophysical Journal* **927,** 6 (2022).

70. Paugnat, H., Lupsasca, A., Vincent, F. & Wielgus, M. Photon ring test of the Kerr hypothesis: Variation in the ring shape. *Astronomy & Astrophysics* **668,** A11 (2022).

71. Vincent, F. H., Gralla, S. E., Lupsasca, A. & Wielgus, M. Images and photon ring signatures of thick disks around black holes. *Astronomy & Astrophysics* **667,** A170 (2022).

72. Ayzenberg, D. Testing gravity with black hole shadow subrings. *Classical and Quantum Gravity* **39,** 105009 (2022).

73. Tsupko, O. Y. Shape of higher-order images of equatorial emission rings around a Schwarzschild black hole: Analytical description with polar curves. *Physical Review D* **106,** 064033 (2022).

74. Bisnovatyi-Kogan, G. S. & Tsupko, O. Y. Analytical study of higher-order ring images of the accretion disk around a black hole. *Physical Review D* **105,** 064040 (2022).

75. Penrose, R. Gravitational collapse and space-time singularities. *Physical Review Letters* **14,** 57 (1965).

76. Hawking, S. W. & Ellis, G. F. *The large scale structure of space-time* (Cambridge university press, 2023).

77. Mottola, E. in *Regular Black Holes: Towards a New Paradigm of Gravitational Collapse* 283–352 (Springer, 2023).

78. Hawking, S. W. Particle creation by black holes. *Communications in mathematical physics* **43,** 199–220 (1975).

79. Hawking, S. W. Black holes and thermodynamics. *Physical Review D* **13,** 191 (1976).

80. Mazur, P. O. & Mottola, E. Gravitational Condensate Stars: An Alternative to Black Holes. *Universe* **9,** 88. arXiv: gr-qc/0109035 (2023).

81. Hawking, S. W. Information loss in black holes. *Physical Review D* **72,** 084013 (2005).

82. Cardoso, V. & Pani, P. Testing the nature of dark compact objects: a status report. *Living Reviews in Relativity* **22,** 1–104 (2019).

83. Abramowicz, M. A., Kluźniak, W & Lasota, J.-P. No observational proof of the black-hole event-horizon. *Astronomy & Astrophysics* **396,** L31–L34 (2002).

84. Lemos, J. P. & Zaslavskii, O. B. Black hole mimickers: Regular versus singular behavior. *Physical Review D* **78,** 024040 (2008).

85. Cardoso, V., Pani, P., Cadoni, M. & Cavaglia, M. Ergoregion instability of ultracompact astrophysical objects. *Physical Review D* **77,** 124044 (2008).

86. Rosa, J. L., Garcia, P., Vincent, F. H. & Cardoso, V. Observational signatures of hot spots orbiting horizonless objects. *Physical Review D* **106,** 044031 (2022).

87. Rosa, J. L., Macedo, C. F. & Rubiera-Garcia, D. Imaging compact boson stars with hot-spots and thin accretion disks. *arXiv preprint arXiv:2303.17296* (2023).

88. Tamm, H. L. & Rosa, J. L. Observational properties of hot spots orbiting relativistic fluid spheres. *Physical Review D* **109,** 044062 (2024).

89. Wheeler, J. A. Geons. *Phys. Rev.* **97,** 511–536. https://link.aps.org/doi/10.1103/PhysRev.97.511 (2 1955).

90. Power, E. A. & Wheeler, J. A. Thermal Geons. *Rev. Mod. Phys.* **29,** 480–495. https://link.aps.org/doi/10.1103/RevModPhys.29.480 (3 1957).

91. Kaup, D. J. Klein-Gordon Geon. *Phys. Rev.* **172,** 1331–1342. https://link.aps.org/doi/10.1103/PhysRev.172.1331 (5 1968).

92. Liebling, S. L. & Palenzuela, C. Dynamical boson stars. *Living Reviews in Relativity* **26,** 1 (2023).

93. Jetzer, P. Boson stars. *Physics Reports* **220,** 163–227 (1992).

94. Schunck, F. E. & Mielke, E. W. General relativistic boson stars. *Classical and Quantum Gravity* **20,** R301–R356. ISSN: 1361-6382. http://dx.doi.org/10.1088/0264-9381/20/20/201 (2003).

95. Tolman, R. C. Static solutions of Einstein's field equations for spheres of fluid. *Physical Review* **55,** 364 (1939).

96. Buchdahl, H. A. General relativistic fluid spheres. *Physical Review* **116,** 1027 (1959).

97. Rosa, J. L. & Piçarra, P. Existence and stability of relativistic fluid spheres supported by thin shells. *Physical Review D* **102,** 064009 (2020).

98. Rosa, J. L. Observational properties of relativistic fluid spheres with thin accretion disks. *Physical Review D* **107,** 084048 (2023).

99. Visser, M. & Wiltshire, D. L. Stable gravastars: An Alternative to black holes? *Class. Quant. Grav.* **21,** 1135–1152. arXiv: gr-qc/0310107 (2004).

100. Lobo, F. S. & Arellano, A. V. Gravastars supported by nonlinear electrodynamics. *Classical and Quantum Gravity* **24,** 1069 (2007).

101. Visser, M. & Wiltshire, D. L. Stable gravastars—an alternative to black holes? *Classical and Quantum Gravity* **21,** 1135 (2004).

102. Martin-Moruno, P., Garcia, N. M., Lobo, F. S. & Visser, M. Generic thin-shell gravastars. *Journal of Cosmology and Astroparticle Physics* **2012,** 034 (2012).

103. Lobo, F. S. & Crawford, P. Stability analysis of dynamic thin shells. *Classical and Quantum Gravity* **22,** 4869 (2005).

104. Chirenti, C. B. & Rezzolla, L. How to tell a gravastar from a black hole. *Classical and Quantum Gravity* **24,** 4191 (2007).

105. Lobo, F. S. Stable dark energy stars. *Classical and Quantum Gravity* **23,** 1525 (2006).

106. Horvat, D., Ilijić, S. & Marunović, A. Radial stability analysis of the continuous pressure gravastar. *Classical and Quantum Gravity* **28,** 195008 (2011).

107. Posada, C. & Chirenti, C. On the radial stability of ultra-compact Schwarzschild stars beyond the Buchdahl limit. *Classical and Quantum Gravity* **36,** 065004 (2019).

108. Will, C. M. The confrontation between general relativity and experiment. *Living reviews in relativity* **17,** 1–117 (2014).

109. Yagi, K. & Stein, L. C. Black hole based tests of general relativity. *Classical and Quantum Gravity* **33,** 054001 (2016).

110. Akiyama, K. *et al.* First Sagittarius A$^*$ Event Horizon Telescope results. IV. Variability, morphology, and black hole mass. *The Astrophysical Journal Letters* **930,** L15 (2022).

111. Abuter, R. *et al.* Detection of the gravitational redshift in the orbit of the star S2 near the Galactic centre massive black hole. *Astronomy & Astrophysics* **615,** L15 (2018).

112. Collaboration, G. *et al.* VizieR Online Data Catalog, p. *I/345* (2018).

113. Witzel, G *et al.* Rapid variability of Sgr A$^*$ across the electromagnetic spectrum. *The Astrophysical Journal* **917,** 73 (2021).

114. Michail, J. M., Wardle, M., Yusef-Zadeh, F. & Kunneriath, D. Multiwavelength Observations of Sgr A$^*$. I. 2019 July 18. *The Astrophysical Journal* **923,** 54 (2021).

115. Abuter, R *et al.* Constraining particle acceleration in Sgr A with simultaneous GRAVITY, Spitzer, NuSTAR, and Chandra observations. *Astronomy & Astrophysics* **654,** A22 (2021).

116. Abuter, R *et al.* Polarimetry and astrometry of NIR flares as event horizon scale, dynamical probes for the mass of Sgr A. *Astronomy & Astrophysics* **677,** L10 (2023).

117. Broderick, A. E. & Loeb, A. Imaging bright-spots in the accretion flow near the black hole horizon of Sgr A. *Monthly Notices of the Royal Astronomical Society* **363,** 353–362 (2005).

118. Bauböck, M *et al.* Modeling the orbital motion of Sgr A$^*$'s near-infrared flares. *Astronomy & Astrophysics* **635,** A143 (2020).

119. Hooft, G. The self-screening Hawking atmosphere—A different approach to quantum black hole microstates. *Nuclear Physics B-Proceedings Supplements* **68,** 174–184 (1998).

120. Thorne, K. S., Wheeler, J. A. & Misner, C. W. *Gravitation* (Freeman San Francisco, CA, 2000).

121. Plebanski, J. & Krasinski, A. *An introduction to general relativity and cosmology* (Cambridge University Press, 2006).

122. *Black hole physics: Basic concepts and new developments* (eds Frolov, V. P. & Novikov, I. D.) (1998).

123. Rindler, W. *Relativity: special, general, and cosmological* 2003.

124. Eddington, A. S. A comparison of Whitehead's and Einstein's formulæ. *Nature* **113,** 192–192 (1924).

125. Finkelstein, D. Past-future asymmetry of the gravitational field of a point particle. *Physical Review* **110,** 965 (1958).

126. Kruskal, M. D. Maximal extension of Schwarzschild metric. *Physical review* **119,** 1743 (1960).

127. Szekeres, G. On the singularities of a Riemannian manifold. *Publicationes Mathematicae Debrecen 7* **7,** 285 (1960).

128. Misner, C. W., Thorne, K. S. & Wheeler, J. A. *Gravitation* (Macmillan, 1973).

129. De Sitter, W. Einstein's theory of gravitation and its astronomical consequences. Third paper. *Monthly Notices of the Royal Astronomical Society, Vol. 78, p. 3-28* **78,** 3–28 (1917).

130. Berti, E. *Black Hole Perturbation Theory* URL: `https://www.icts.res.in/event/page/3071`. 2016.

131. Shapiro, S. L. & Teukolsky, S. A. *Black holes, white dwarfs, and neutron stars: The physics of compact objects* (John Wiley & Sons, 2008).

132. Pani, P., Berti, E., Cardoso, V., Chen, Y. & Norte, R. Gravitational wave signatures of the absence of an event horizon: Nonradial oscillations of a thin-shell gravastar. *Physical Review D* **80,** 124047 (2009).

133. Israel, W. Singular hypersurfaces and thin shells in general relativity. *Il Nuovo Cimento B (1965-1970)* **44,** 1–14 (1966).

134. Grould, M., Paumard, T. & Perrin, G. Testing the validity of the ray-tracing code GYOTO. *Astronomy & Astrophysics* **591,** A116 (2016).

135. Vincent, F. *et al.* Geometric modeling of M87* as a Kerr black hole or a non-Kerr compact object. *Astronomy & Astrophysics* **646,** A37 (2021).

136. Lamy, F., Gourgoulhon, E., Paumard, T. & Vincent, F. H. Imaging a non-singular rotating black hole at the center of the Galaxy. *Classical and Quantum Gravity* **35,** 115009 (2018).

137. Vincent, F. H., Gourgoulhon, E., Herdeiro, C. & Radu, E. Astrophysical imaging of Kerr black holes with scalar hair. *Physical Review D* **94,** 084045 (2016).

138. Vincent, F. H., Gourgoulhon, E. & Novak, J. 3+ 1 geodesic equation and images in numerical spacetimes. *Classical and Quantum Gravity* **29,** 245005 (2012).

139. Grandclement, P., Somé, C. & Gourgoulhon, E. Models of rotating boson stars and geodesics around them: new type of orbits. *Physical Review D* **90,** 024068 (2014).

140. Rybicki, G. B. & Lightman, A. P. *Radiative processes in astrophysics* (John Wiley & Sons, 1991).

141. Jampolski, D. & Rezzolla, L. Nested solutions of gravitational condensate stars. *Classical and Quantum Gravity* **41,** 065014 (2024).